UNIVERSIDAD NACIONAL AUTÓNOMA DE MÉXICO
PROGRAMA DE POSGRADO EN ASTROFÍSICA
INSTITUTO DE ASTRONOMÍA

The effect of morphology and dynamics of large scale non-axisymmetric structures in galaxies on Radial Migration

TESIS QUE PARA OPTAR POR EL GRADO DE:
Doctor en Ciencias (Astrofísica)

PRESENTA:
Gerardo Martínez Bautista

TUTOR PRINCIPAL
Dr. Héctor Manuel Velázquez
Instituto de Astronomía
Dra. María de los Ángeles Pérez Villegas
Instituto de Astronomía

COMITÉ TUTOR
M. en C. Christine Allen, Instituto de Astronomía
Dr. Sebastián Sánchez, Instituto de Astronomía
Dr. Jesús González, Instituto de Astronomía

CIUDAD UNIVERSITARIA, CDMX, MARZO, 2022.

JURADO ASIGNADO:

Presidente:

Secretario:

Vocal:

1er. Suplente:

2o. Suplente:

La tesis se realizó en el Instituto de Astronomía, UNAM.

TUTORES:

Dr. Héctor Manuel Velázquez
Instituto de Astronomía
Dra. María de los Ángeles Pérez Villegas
Instituto de Astronomía

AGRADECIMIENTOS

"La grandeza de una nación y su progreso moral pueden ser juzgados por la manera en que ellos tratan a sus animales. Yo siento que el progreso espiritual requiere que en algún momento dejemos de matar a nuestras criaturas hermanas para la satisfacción de nuestros deseos corporales."
Mahatma Gandhi.

Agradezco a CONACyT por el apoyo económico recibido para desarrollar este proyecto doctoral, al proyecto DGAPA-PAIIT IN101918, al Laboratorio Nacional de Supercómputo del Sureste-CONACyT, al Centro Nacional de Supercómputo-IPICYT-CONACyT y Miztli de la DGTIC-UNAM, al proyecto LAMOD UNAM a través de los clusters Atocatl y Tochtli y al proyecto DGAPA-PAIIT IN100519.

Agradezco a la Facultad de Ciencias y al Instituto de Astronomía de la Universidad Nacional Autónoma de México por todo el conocimiento, experiencias y recursos recicibidos. Espero que en algún momento de la vida, pueda hacer llegar parte de ello a la sociedad, que es la que, en el fondo, permitió que yo pudiera recibir la educación que ahora termina.

En numerosas ocasiones surgían dudas que amablemente me ayudaron a resolver muchas personas en el Instituto de Astronomía y por ello les doy las gracias, y también al posgrado por su apoyo en momentos difíciles. Agradezco a la Maestra Christine Allen, al Doctor Jesús González y al Doctor Sebastián Sánchez que me acompañaron durante todo el proyecto y mis sinodales que enriquecieron enormemente esta tesis con sus comentarios.

Sin la ayuda de mis asesores, el Doctor Héctor Velázquez y la Doctora Ángeles Pérez Villegas, este proyecto no habría llegado a buen puerto. Ahora puedo decir que todo

valió la pena. Muy particularmente quiero agradecer al Doctor Edmundo Moreno por su tiempo y aunque ya no está, a la Doctora Bárbara Pichardo por haberme dado un tema de investigación que se ve reflejado en la obtención de un grado académico.

Este doctorado es uno de los mejor premios que el esfuerzo y dedicación pueden ofrecer como recompensa, todos eso inumerables días de trabajo ya pueden ser cuantificados; este logro es de Flor, a quien le doy infinitas gracias. Le doy las gracias a Ramón, René y a sus familias y a quién recuerdo todos los días y que ahora ya volvió a convertirse en polvo de estrellas. Sin ti, esto jamás habría terminado, con amor te doy las gracias Nubia.

La vida tiene muchas cosas raras, pero en cualquier circunstancia, han habido personas a las que quiero y que me quieren en esta ciudad y en aquella detrás de los volcanes o en otras más, muchas gracias.

Quisiera reducirlo a una sola frase: ¡este doctorado es de todos!

Resumen

La tesis de doctorado que lleva por nombre "The effect of morphology and dynamics of large scale non-axisymmetric structures in galaxies on Radial Migration", tiene como objetivo realizar un estudio sistemático de la influencia de los parámetros estructurales y dinámicos de los brazos espirales, tales como ángulo de enrollamiento, amplitud, longitud de escala radial y velocidad angular, en la migración radial estelar en galaxias de disco. Para este análsis se emplearon simulaciones de partículas prueba en modelos galácticos estacionarios de galaxias espirales no barradas.

La ventaja de los modelos estacionarios es la flexibilidad de estos potenciales para variar los parámetros de los brazos espirales (y del fondo axisimétrico) y aislar el efecto que cada parámetro tiene sobre la dinámica orbital estelar en los discos de las galaxias.

Se construyeron dos modelos galácticos, uno para representar galaxias espirales tempranas (Sa) y otro para galaxias espirales tardías (Sc), considerando así el efecto en una galaxia masiva y una poco masiva. Con estos dos modelos galácticos, se realizaron varias simulaciones de partículas prueba con diferentes configuraciones de los brazos espirales.

Los diagnósticos utilizados para cuantificar la influencia de cada parámetro del brazo en la migración radial fueron los cambios en distintos intervalos de tiempo de: 1) momento angular en la dirección perpendicular al disco L_z; 2) excentricidad; y 3) radio.

De estos análisis se puede concluir que todos los paramétros de los brazos espirales tienen una contribución en la migración radial, que principalmente se observa en las regiones de resonancias, mayormente en la zona de corrotación. Se destaca que la longitud de escala de los brazos espirales es el parámetro con mayor contribución a la migración radial estelar en el disco galáctico. Esto implica que, las estrellas son desplazadas desde su lugar de origen hacia otras distancias galactocéntricas, mezclando el material del disco.

Adicionalmente, se encontraron otros resultados derivados del trabajo, por ejemplo, formación de subestructuras (ridges), la forma de la distribución de metalicidad estelar y sus implicaciones dinámicas.

Abstract

The doctoral dissertation called "The effect of morphology and dynamics of large scale non-axisymmetric structures in galaxies on Radial Migration", aims to carry out a systematic study of the influence of the structural and dynamic parameters of the spirals arms, such as pitch angle, amplitude, radial scale length, and angular velocity, in stellar radial migration in disc galaxies. For this analysis, simulations of test particles in stationary galactic models were used.

The advantage of stationary models is the flexibility of these potentials to vary the parameters of the spiral arms (and of the axisymmetric background) and to isolate the effect that each parameter has on the stellar orbital dynamics in the galactic discs.

Two galactic models were built, one to represent early-type spiral galaxies (Sa) and one for late-type spiral galaxies (Sc), to consider the effect on a massive and a less massive galaxy. With these two axisymmetric galactic models, a set of test-particles simulations with different configurations of the spiral arms were made.

The tests used to quantify the influence of each arm parameter on radial migration were the changes in different time intervals of: 1) angular momentum in the z direction; 2) eccentricity; and 3) radius.

From these analyses, it can be concluded that all the parameters of the spiral arms have a contribution to the radial migration, which is principally observed in the regions of the resonances, mainly in the corotation zone. It is highlighted that the scale length of the spiral arms is the parameter with the highest contribution to stellar radial migration in the galactic disc. This implies that the stars are moved from their birth places to another galactocentric distances several kpc, mixing the disc material.

In addition, other results derived from this work were found, for instance, substructure formation (ridges), shapes of the metallicity curves and their dynamical implications.

Contents

List of Figures

List of Tables

Chapter 1

Introduction

Ancient cultures have looked to the sky in clear nights, trying to understand all those shivering luminous points. A lot of questions arose, but only simple explanations were archived. A divine creation acting on every thing on the Earth and beyond. The same day and night are part of this plan and many civilizations around the world associated gods and goddesses to the celestial phenomena that ruled their lives.

During several centuries, several spheres centered in the Earth would not allow any question about the origin of the existence of the humankind or its nature. Those spheres contained the stars and more clearly the planets. Now, the idea that the human beings were at the center of the Universe had support.

The break in Wittenberg allowed to rethink the human place among the planets, the Sun and the other celestial bodies. It left the door wide open for the "On the Revolutions of the Heavenly Spheres (Copernicus, 1543)", that could have been hidden for a long time, but in the middle of the conflict, the two ways to see the world were involved in the search for truth and the evidence prevailed; people are not any more in the center of the Universe, but the privileged place was not lost. It was not until the beginning of the XVIIth century that, finally the reason started to be used instead of beliefs and the superstitions. Although that continues to exist, it is no longer considered to explain the phenomena of nature, despite the fact that some peasant minds continue to cling desperately.

Nevertheless, this superstition gave rise to the most brilliant idea ever thought by the humankind: the laws of motion in the Earth are the same for the solar system. Now there are rules to explain the movements in the sky and there is no need for an unseen reason.

While the night observations improved, new and very far structures that, at the beginning it was assumed that they formed part of the Milky Way, were discovered. Then, in the early 1900s a realm of those objects was announced (Hubble, 1936). Those

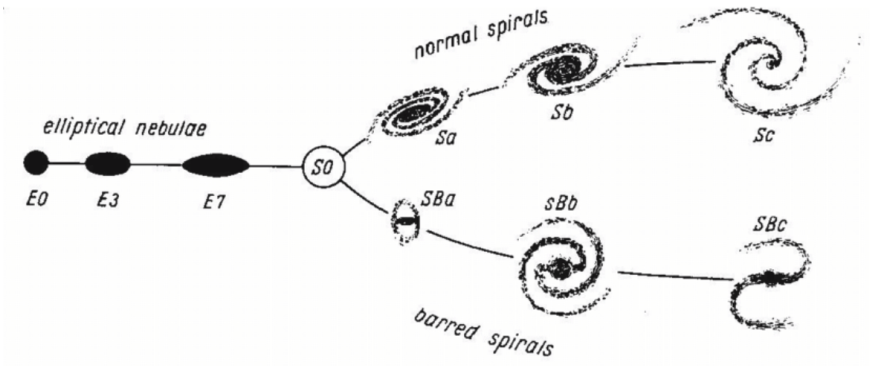

Figure 1.1: Hubble sequence of the tuning fork. Taken from Hubble (1936).

objects were not part of our Galaxy, but this discovery would not have been possible without the fundamental period-luminosity relation of the Cepheid stars, remarkably established by Leavitt & Pickering (1912).

Figure 1.1 shows the "nebulae" known until then that, in fact were other galaxies. Anew, as the telescopes became more powerful, the Hubble sequence classification was highly modified to include all kinds of galaxies at very large distances from the Earth. Nowadays a large number of morphological classifications is available and includes a wide range of forms. Figure 1.2 shows the large number of possible galactic forms in the Universe.

As the knowledge of the galaxies steadily grew up, it was figured out that in the Universe also there were galaxies interacting with other galaxies and in some way the Milky Way does as well, like for example as Magellanic Clouds. This, raised the need to create a new form to archive the galaxies, the Vorontsov-Velyaminov (1959) and later Arp (1966) catalogs of interacting galaxies.

According to Sloan Digital Sky Survey (SDSS; Abazajian et al., 2003), the local Universe is dominated by two main types of galaxies: spiral and elliptical galaxies. In a very general way, the elliptical galaxies are massive concentrations of old and small stars that apparently were born at the same time, and they do not have a lot of dust and gas and are supported by velocity dispersion.

On the other hand, the spiral or disc galaxies are dynamically interesting and have several internal structures and are supported by rotation, which means that there is a main plane where the stars move around the galactic center. This kind of galaxies has dust, gas, old and young stars due to the uninterrupted star formation since its formation.

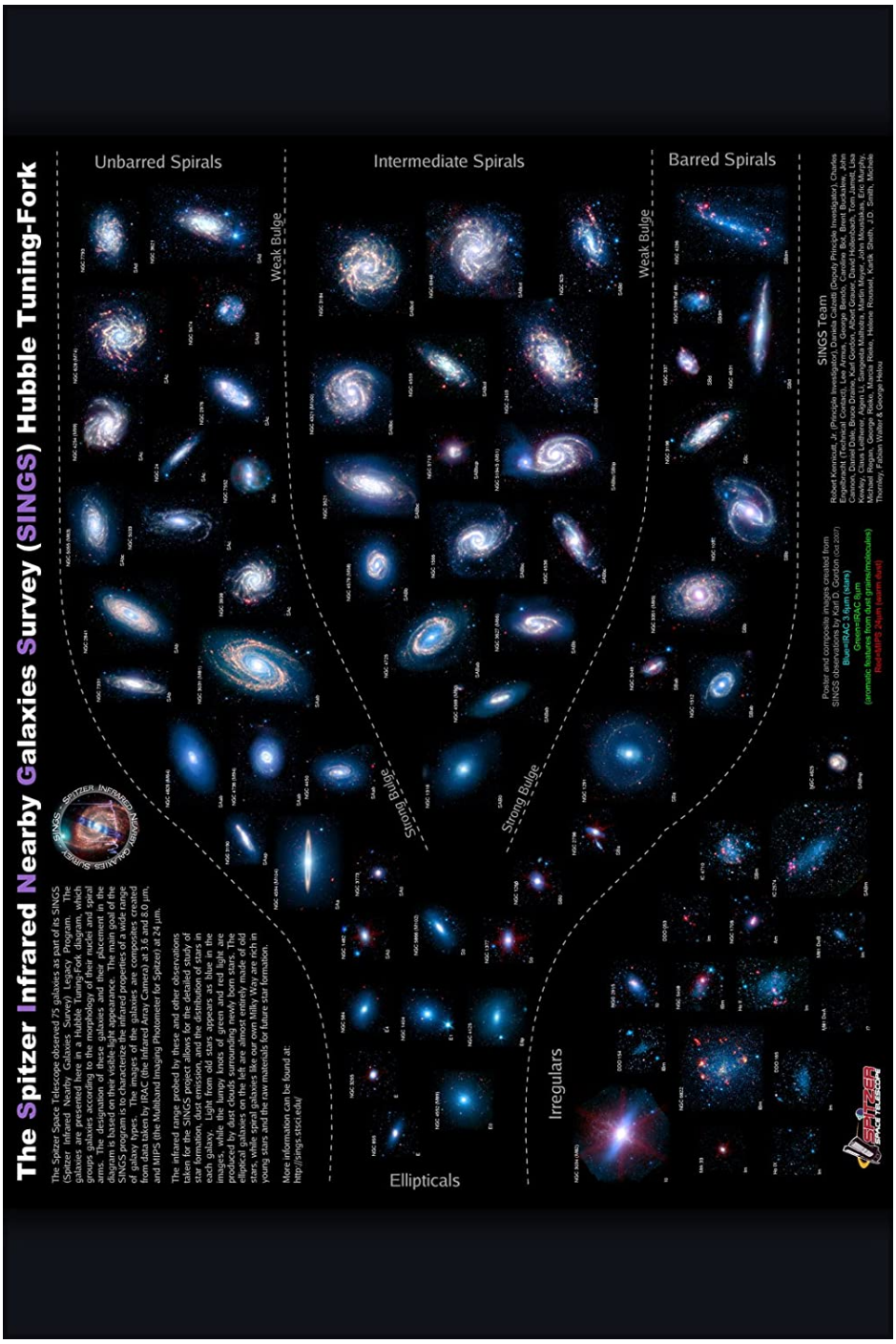

Figure 1.2: Hubble sequence in near infrared frequency. Credits: K. D. Gordon, 2007 composed from SINGS observations.

Since the non-axysimmetric structures in spiral galaxies were discovered, spiral arms and bars, many efforts have been made to explain their formation, evolution and their influence on galaxies. Of course galaxies are not simple objects and their study must be done carefully.

1.1 Spiral galaxies discs

A spiral galaxy is a complex system, and there is no monolithic gravitational potential able to describe it. Therefore, to model such complex system, it is needed to use different gravitational potentials, usually divided in axisymmetric and non-axisymmetric ones. The axisymmetric background contains a dark matter halo, a bulge, and a disc; while the non-axisymmetric components include spiral arms and stellar bars (in some cases). Particularly interesting is the baryonic evolution in the disc where stellar formation or development of non-axisymmetric structures, among others, take place.

The thin disc is a flat distribution of gas, dust and stars with a wide range of ages. It contains the spiral arms, molecular clouds, and it is the place where star formation happens, etc. It is thought to be formed by dissipation during the collapse of the protogalactic gas cloud. The thick disc is a fainter component seen in some galaxies. It is made of a population of old, metal-poor stars and is thought it could had be made as a result of heating by accretion of satellite galaxies.

In a sample of 36 edge-on undisturbed disc galaxies and spanning a wide range of mass, Yoachim & Dalcanton (2006) measured the structural parameters in the R-band. They require both a thick and a thin disc to fit the data. They argued that the observed structural parameters agree well with the properties of thick and thin discs for the Milky Way and stellar populations in nearby galaxies. Their general conclusions are:

1. thick discs have a scale-height at least 2 times larger than thin disks;
2. thick discs have systematically larger scale-lengths than thin discs;
3. in low-mass galaxies, the thick disc can dominate the total R-band luminosity;
4. the thick disc comprises 5%–40% of the total baryonic mass of our galaxy.

Particularly for the Milky Way, the thick disc has a scale-height about 0.75 ± 0.07 kpc and an exponential scale-length of 4.1 ± 0.4 kpc (from SEGUE photometry), and for the thin disc is about 250 to 300 pc and 2 to 4 kpc respectively. Larger scale-height means a higher velocity dispersion, differentiating both disc, but also the thick disc stellar population is older and more metal-poor than the stars in the thin disc.

According to Veltz et al. (2008) in the Milky Way there are three kinematically stellar components:

- thin disk - z_0 225 pc and $\sigma_z \pm 18$ km s^{-1},

- thick disk - z_0 1048 pc and $\sigma\pm$ 40 km s^{-1},
- halo component - $\sigma\pm$ 65 km s^{-1}.

1.1.1 General features

Discs are a flattened radial distribution of dust, gas and stars falling exponentially in density as radial distance increases, including the thin and the thick disks showing different chemical compositions and kinematics. Discs approximate very close to radial hydrostatic equilibrium, rotate differentially and the main population of stars is young, known as Population I, due to the large concentration of star forming gas.

It is hard to determine how large a disc is because there is no a clear physical limit. A measurable quantity is the surface brightness, that can be approximated by an exponential $I(R)\ \alpha\ e^{-\frac{R}{h}}$ depending on the radius and a scalelength. Now defining the isophotal radius, a disc size is estimated, usually when R_{25} [1] is reached. According to Fathi et al. (2010) the radial distribution of stars i.e. scalelength, is independent of the morphological type and in average is about 3.8 $\pm$ 2.0 kpc in four optical bands. The vertical brightness can be modeled as a sech$^2(\frac{z}{z_0})$, and the scaleheight z_0 correlates with the rotation velocity, a very useful property to estimate the thickness of a disc if it is not seen edge-on (van der Kruit, 1988a).

1.2 Stellar kinematics and stability in discs

Considering axial symmetry and a flat rotation curve, the vertical stellar disc dynamics can be studied relating the Poisson equation

$$\frac{dK_z}{dz} = -4\pi G\rho(z) \tag{1.1}$$

and the Jeans equation

$$\frac{d}{dz}\left[\rho(z)\sigma_z^2(z)\right] = \rho(z)K_z, \tag{1.2}$$

where K_z is the gravitational force component, ρ is the density and σ_z is the velocity dispersion. Equating 1.1 and 1.2 it is obtained

$$\sigma_z(R) = \sqrt{c\pi G\Sigma(R)z_0}, \tag{1.3}$$

where c is a constant that varies between 3/2 for an exponential to 2 for an isothermal distribution and $\Sigma(R)$ is the stellar surface density. Equation 1.3 (van der Kruit, 1988b) is the hydrostatic equilibrium relating the vertical distribution of stars and their mean

[1] Surface brightness of 25 mag arcsec^2 in the B band.

vertical velocity dispersion to the distribution of mass.

The Toomre's criterion (Toomre, 1964)

$$Q = \frac{\sigma_R \kappa}{3.36 G \Sigma}, \tag{1.4}$$

is a parameter to establish galactic disc stability to local axisymmetric disturbances and depends on the stellar radial velocity dispersion σ_R, the epicyclic frequency κ and the local mass surface density Σ. At small scales it becomes a Jeans-type stability, where random motions driven by the kinetic energy neutralize the gravity collapse. Local stability requires $Q > 1$.

1.3 Spiral arms and bars

The main substructures formed in the galactic disc are the spiral arms and bars. Both are perturbations on the disc and their effects should be considered on the galactic evolution.

Sometimes spiral arms have a well-defined two-armed pattern, known as "grand design", whereas in others cases the spiral structure is flocculent (Elmegreen & Elmegreen, 1984). Since the spiral arms come in a wide variety of shapes, their dynamical and physical structure have to be delimited for a better galactic evolution comprehension. The most important properties are: the locus, number of arms, pitch angle, scale-height and scale-length, mass and radial force component, density law along the spiral arm, internal and external limits and the pattern speed (Sellwood & Masters, 2021).

Although galactic bars can develop structures like bumps or x-shape structures, they can be thought as an unified block made of stars at the center of the galaxy. Bars play an important role in the galactic evolution, but it depends on their properties like the length, axis ratios (triaxial systems), density law, mass and the pattern speed (Athanassoula, 2016).

1.4 Analysing the disc stellar dynamics: Steady models

The main advantage of a complete steady galactic model is its simplicity and a low consume of computational resources. A first proxy to study stellar dynamics is by building a full galactic model including a dark matter halo, a disc and a bulge, and for the non-axisymmetric contribution could be chosen spiral arms and bars. The full model, then, is very flexible to change its properties in its different components, for

instance for the background potential varying from a massive early-type galaxy (Sa) to a less massive late-type galaxy (Sc) and for the non axisymmetric ones, in the case of the spiral arms, pitch angle, angular speed, amplitude, mass, length, respectively. For the bars, the mass, shape, extension, and pattern speed can also be modified to represent different possible bars observed in real galaxies (Patsis & Tsigaridi, 2017; Chaves-Velasquez et al., 2019; Patsis & Athanassoula, 2019).

The selection of a galactic configuration, along the space parameters according to the Hubble sequence, also its flexibility allows changes in the different galactic components i.e. distinct dark matter halos (Navarro et al., 1996), number of spiral arms, thin and thick dynamical discs etc. This model including appropriate initial conditions for the disc, despite of its simplicity, will bring a plausible clue of the stellar behavior in different galactic configurations.

The former description can be used as a support to constrain the universe of parameters, setting the most important dynamical and structural characteristics. The natural next approach, would be to consider improved potentials. For instance, a model which includes spiral arms and a bar, based on COBE/DIRBE infrared data (Weiland et al., 1994; Freudenreich, 1998).

After the initial conditions are suitably determined (specific galaxies modeling), models like those found in Pichardo et al. (2003, 2004) can be used to study the stellar dynamics in a more accurate way. The stellar dynamics is related to the influence of non-axisymmetric perturbers, and this model for the spiral arms and the bar could be taken into account. The new model, will produce a reliable view of stellar dynamics, able to be complemented with N-body simulations. The improved model was postponed due its considerable larger consume of computational resources than the first, more simple, cosine model.

1.5 Radial Migration

In 2002, Sellwood & Binney (2002) (hereafter SB02) explored the interaction between the spiral arms and the stars.

In the perturber pattern rotating reference frame, the Jacobi's integral E_j is conserved $E_j = E - \Omega_{sp} L$, where E and L are the energy and the angular momentum of a star in an inertial reference frame and Ω_{sp} is the pattern speed of the perturbation, for example, the spiral arms. Then, a change in energy and L are related by

$$\Delta E = \Omega_{sp} \Delta L. \tag{1.5}$$

Considering the "radial action" J_R[1] which is a measure of the distance from the circular-orbit curve or a measurement of the stellar eccentricity in a rosette, the increment of energy ΔE can be determined by

$$dE = \frac{\partial E}{\partial J_R} dJ_R + \frac{\partial E}{\partial L} dL, \tag{1.6}$$

where $\frac{\partial E}{\partial J_R}$ becomes the radial frequency ω_R and $\frac{\partial E}{\partial L}$ is the circular frequency Ω. Eliminating ΔE from 1.5 and 1.6 it is obtained

$$\Delta J_R = \frac{\Omega_{sp} - \Omega}{\omega_R} \Delta L, \tag{1.7}$$

then, changes in L at corotation do not cause changes in J_R, i.e. do not change the circularity of the orbit of a star, while in other places do.

Now, at Lindblad resonances ω_R obeys

$$\omega_R = \pm m(\Omega_{sp} - \Omega), \tag{1.8}$$

where m is the number of spirals arms. Combining 1.7 and 1.8 it is obtained

$$\Delta J_R = \pm \frac{1}{m} \Delta L, \tag{1.9}$$

minus sign is applied to ILR and plus sign to OLR.

An alternative way to identify if there is or not radial migration is to study changes in L_z and simultaneously, changes in the orbital eccentricity. In this case, around the main resonances, but focused in corotation, if there are changes in L_z and no changes in eccentricity, it can be interpreted as radial migration, because the star changes its radius but not its circularity due to the interaction with non-axisymmetric structures. This method is equivalent to the method proposed by SB02.

1.5.1 Radial migration "in context"

There is not a general agreement in the literature about some definitions. For instance, Minchev & Famaey (2010) studied spiral-bar resonances overlapping due to different pattern speeds for the non-axisymmetric structures in a steady potential. They used the concept of radial migration (RM) as any change in L, which is strongly redistributed in the disk, speeding up the disk mixing. For this study, the definitions stated by SB02 and Schönrich & Binney (2009) are adopted, briefly described as follows.

A change in L can only be driven by non-axisymmetric forces. In other words, spiral arms, bars or molecular clouds and it is divided in two branches: "churning"

[1]For more details see section 3.5 of Binney & Tremaine (2008).

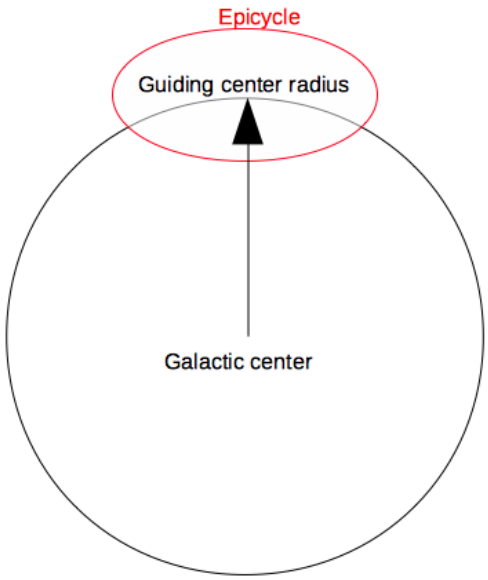

Figure 1.3: The black curve is the guiding center radius where the star orbits in average, and the red curve is the epicyclic where the star describes rosettes.

which means a change in L but not in the eccentricity of the stellar orbit, called RM and "stirring" (also called blurring by some authors) implying both changes in L and eccentricity, known as dynamical stellar heating or simply heating. The principal difference between RM and heating is that the first one changes permanently the radial metallicity distribution in the galaxy due to a net increase or decrease of its "guiding radius", which is the mean radius where the star describes rosettes due to the epicycles (see Figure 1.3), while the second one does not change permanently the metallicity distribution because it has not a fixed "guiding radius" (Vera-Ciro et al., 2014).

There have been different ways to study RM since SB02 proposed this mechanism to move stars by resonances, likely inward or outward, from their birth places; stationary models and N-body + SPH simulations are the principal tools. There is a general consensus on the effects of RM on the galactic evolution, although some works show fundamental discrepancies.

As far as stationary models is concerned, using a simplistic stationary galactic model for a galaxy, where the spiral arms and the bar (Dehnen, 2000) are represented by a cosine potential, Minchev & Famaey (2010) report that the resonance overlapping of the bar and spiral structure induces a nonlinear response, leading to a strong redistribution of angular momentum in the disk. They propose the resonance overlapping as a new mechanism to mix the disk due to stellar migration and conclude that is a more efficient process than transient spiral arms, since it takes only 3 Gyr to heat up the disk, while for the spiral arms takes 9 Gyr to reach the same effect.

An important addition to the understanding of RM in the context of a full galactic model and its individual components has been carried out by Martinez-Medina et al. (2016), showing the different regimes where each component acts. Separating between heating and RM, they split individual contributions of each component finding that the radial mixing of the stellar disc at the inner radii (inside 5 kpc in their model) is produced by the joint action of the perturbers, and it is dominated by radial heating while at outer radii (beyond 9 kpc in their model), the changes of angular momentum for each particle, is caused mostly by the spiral arms dynamical influence and dominated by radial migration, preserving their eccentricities at the corotation resonance. Martinez-Medina et al. (2017) used a different chemical tagging jointly a potential model to provide a restriction to the abundance gradient of the disk, at all times and radii. They show that the impact of RM can be discerned by the metallicity distribution of the stellar disk, constraining the structural and dynamical parameters of the spiral arms in the Milky Way, to fit the metallicity distribution function (MDF, which shows a particular stellar metallicity, for instance, [Fe/H]) of a population of stars shapes which are sensitive to the scale radius of the arms, the pattern speed, and the pitch angle. Also, they explain how some stars exhibit a chemical content that does not correspond with their current location due to RM. The authors achieved their results using a background axisymmetric potential, and a model formed by a two-armed 3D density distribution made of individual inhomogeneous oblate spheroids (Pichardo et al., 2003) and for the bar, they selected the triaxial bar model of Pichardo et al. (2004); this is an inhomogeneous ellipsoid built as the superposition of a large number of homogeneous ellipsoids, to obtain a smooth radial decline.

Kubryk et al. (2013) studied the effects of RM (for them, any change in the radial stellar orbit) and chemical evolution in a barred dominated galaxy. Using N-body and SPH codes, they include one stellar disk, one gaseous disk where star formation could happens and a live spherical halo. They find different behaviours for gas and star particles as they are dissipative and non-dissipative systems, respectively. Stars are highly affected by RM while gas remains near its initial radius, except at the galactic center where the bar favors inwards accretion. Even the metallicity profile of the galaxy is relatively flat and the stellar metallicity dispersion is high at the end of the simulation, they argue that it can not be directly associated to RM, even the stars experienced a strong RM along the simulation. They claim that RM depends tightly on the strength of inhomogeneities in the gravitational potential (arms or bars), the duration of the RM (the longer the inhomogeneities act, the larger the effect) and the steepness of abundance profiles at the time most of the stars are formed. Those factors may cancel each other and mask the effects of RM on chemical evolution, downplaying the role of the dynamical phenomenon.

In contrast, Loebman et al. (2016) using an N-body+SPH simulation, show that for a Milky Way-like galaxy, in the inner disk, the shape of the MDF is skewed toward

low metallicities and, outside the solar position the shape of the MDF is skewed toward high metallicities. Comparing their results with the APOGEE (Eisenstein et al., 2011) data release 12 observation, they assert that star heating is very modest and the shift in the skewness is a natural consequence of radial migration caused by spiral arms resonance mechanism at corotation.

In accordance with SB02, RM is mainly induced at the corotation resonance, however the stellar distribution of the whole disc can be modified. Using N-body +SPH simulations, Grand et al. (2012) found that the spiral arms are transient features, whose pattern speeds decrease with radius. This produces different coratation radii and leads to strong efficient migration. Similarilly, the disk can be affected by bars that loses angular momentum and its pattern speed "slows down" with time (Halle et al., 2018), widening the corotation radius. According to Comparetta & Quillen (2012), the disk is also affected by particles migrating outwards when they are at low eccentricity and lag a short lived local density peak. Perturbing the disk with "molecular clouds" to seed spiral patterns, Vera-Ciro et al. (2014) found that strongly affect the thin disk, but they can not conclude if the thick disk is a relic of RM; in contrast, Martinez-Medina et al. (2015) conclude that the increase in vertical velocity dispersion induced by the spiral arms is small and do not induce a significant vertical disk thickening, but if a bar is present, the vertical velocity dispersion increases considerably, mostly within the region covered by the bar.

It is well known that interaction between galaxies modify the stellar dynamics, because the gravitational field of each galaxy affects the stellar orbits of the other. Under this standpoint radial mixing can also be studied. Bird et al. (2012) explored the radial mixing behavior in the framework of an infalling galaxy, finding spiral arms development, and an increase of migration that would add considerable dispersion to the age-metallicity relation of solar neighborhood stars. At the solar position, the disc can broaden until 1.15 kpc, nevertheless they conclude it is not enough to create the thick disc. Also they found that in the outer parts of the disc there is a considerable radial and perpendicular heating. Using test particles of a Galaxy-sized model orbited by a dwarf galaxy, Quillen et al. (2009) studied the external parts of the disc, reporting the induce of a warp, the flattening of the metallicity gradients due to stellar migration (any radial displacement) and spiral structure development.

The Milky Way is the chemically best known galaxy. In the solar neighborhood there are more metal-rich stars that were born in inner Galactocentric radii (Feuillet et al., 2018), allowing the study of the thin and thick disk in the Galaxy independently. Grieves et al. (2018) combined stellar ages and MARVELS radial velocities (Ge et al., 2008) to explore local chemo-kinematics near the Milky Way's plane. They found that the thin disk has stars of all ages at large radii (after excluding high eccentric stars), and positive [Fe/H] skewness in the outskirts, suggesting that radial migration is important in the metallicity scatter of the thin disc. Using a detailed thin disc chemical evolution

model in N-body simulations for a MW-like galaxy, Minchev et al. (2013) study the impact of in-situ chemical enrichment and radial mixing in the solar neighborhood. They find that, due to radial mixing from mergers followed by additional radial mixing driven by the bar and spiral, old metal-poor high-[a/Fe], usually associated with a thick disc are in the solar vicinity, thus the thick disc could be a natural consequence of stellar migration. Also Roškar et al. (2011) report the formation of the thick disc as a natural process, because the stellar migrated population preserve its vertical energy, but at larger radii, the disc surface density falls and the restoring force decreases, then oscillations in the vertical direction increase.

A different conclusion is given by Minchev et al. (2012a). They analyzed the velocity dispersion in the vertical σ_z direction of migrating populations in Tree-SPH N-body simulations. They found that the contribution to σ_z is negative and cools the disc in smaller radii than a bars' corotation radius. Vera-Ciro et al. (2014) found that migrators are stars heavily biased with low vertical velocity dispersion, and respond easily to non-axisymmetric perturbations, but do not see enough changes in the vertical structure to thick the disc, supporting Minchev et al. (2012a) conclusions. In contrast, they report that outward migrators cool down whereas inward migrators heat up the thin disc.

In a different scenario, combining observations from The AMBRE project (Guiglion et al., 2016) with a simple Galactic model (taken from Kubryk et al. 2013), Prantzos et al. (2017) consider separately stellar blurring and churning, and are able to explain the "double-branch" Li behavior, observed in the thin and thick Galactic disks. This last is formed by stars with ages larger than 9 Gyr.

Not only individual stars are affected by RM. N-body simulations show that in a Milky Way-like disk, star clusters migrate to the inner region of the Galaxy, resulting in a fast disintegration of the cluster due to a strong tidal disruption (Fujii & Baba, 2012). Following red-giant stars close the Galactic disk plane using CoRoT-APOGEE data (Anders et al., 2017a), open clusters are less prone to tidal disruption while migrate from the inner parts of the disk up to 5 - 8 kpc, steeping the local intermediate-age cluster metallicity gradient in the Solar neighborhood (Anders et al., 2017b).

There has been an intense debate among researcher about the importance of RM in galactic evolution. Using N-body tree-SPH simulations, Minchev et al. (2012b) found that a disc can triple its extent and flattens its initial radial metallicity gradients because of radial mixing (any change in L) due to bar and spiral instabilities driven by secular evolution, then the stars in the outskirts have high velocity dispersion in the radial direction. Analyzing the spontaneously-forming spiral structure and the angular momentum exchange in an isolated galactic disk, Roškar et al. (2012) found that the spiral structure is transient in amplitude and some stars are tossed from one coratation radius to another, reaching up to 5 kpc in only 0.5 Gyr. On the contrary, for the specific case of the Sun, Klačka et al. (2012) obtain significantly different radial migration

of the Sun, reporting that migrates less than 0.4 kpc if there was a four-armed spiral structure in the Galaxy, while distances between 0.3 - 1.2 kpc can be reached from its origin, if there was a two-armed spiral pattern. Their results are practically insensitive on the spiral structure strength.

Observational support for the influence of RM in different types of disk galaxies is proposed by Ruiz-Lara et al. (2017). Through a galactic surface brightness study from CALIFA survey, they find that RM mixes the stellar content flattening the radial stellar properties, but it strongly depends on the surface brightness profile. Unfortunately they cannot quantify its importance in shaping spiral galaxies, and consider processes like star formation or satellite accretion that might play a significant role. Also analyzing the radial distribution of the oxygen abundances with MUSE, Sánchez-Menguiano et al. (2018) using a sample of 102 spiral galaxies, found that some galaxies show lower (higher) oxygen abundance values in the inner (outer) regions than the expected and derived the distribution of slopes for the abundance gradient and found a large dispersion in the distribution of slopes. They suggest that radial motions might play an important role shaping the abundance profiles. Additionally, an interesting way to quantify how far the stars can travel in a galaxy, due to the observed galactic metal mixing, was proposed by Sánchez et al. (2015), estimating a typical mixing scale length $r_{mix} \sim 0.4 r_e$, with r_e the effective radius, for the NGC 6754 galaxy. The r_{mix} could be associated with dynamical effects.

Recent works show some discrepancies between observational data and simulations. Using analytically based simulations, Daniel et al. (2019) found that even when a star is subject to RM (strictly in corotation), this can be also heated by the ultra harmonic resonances overlapping, produced by transient spiral arms that have their own corotation radius between 4 and 10 kpc, because they have different pattern speeds. Up to 40% of stars that experience RM in the solar surroundings also experience resonant overlapping (Daniel et al., 2019).

Zhuang et al. (2019) explored the influence of radial mixing of a bar and spiral arms, using the radial stellar metallicity in a sample of 244 CALIFA galaxies. Using the stellar population profile, find that the effects produced by radial mixing, do not show strong correlations with stellar population gradients, concluding that radial mixing only provides a secondary influence on the gradients.

Assuming that it is possible to infer the formation radius of a star (knowing elemental abundances and age and the metallicity profile of the ISM at the time of formation), and using orbital information derived from Gaia DR2 data and radial velocities, Feltzing et al. (2020) found that about half of their star sample (red giant branch stars) have experienced churning or blurring. They also find that only 10% experienced RM and between 5-7% of stars have never experienced radial mixing.

1.5.2 Observations: Metallicity distribution functions in galaxies

Since the middle of the last century, the idea of traveling stars from their birth places to a new location was in the mind of the astronomers. Chemically speaking, the evolution of spiral galaxies show traits stellar (and gas) radial displacements (Ohnishi, 1975) and in the density-wave theory of young stars (Lin et al., 1969). Recently, for The Milky Way, the best known galaxy with high resolution observation, shows the connection between the MDF and radial migration. This link explains the shapes of the MDF, arguing that the migration of stars is needed to justify the positive skewness in the outer disc, as can be seen in Figure 1.4 (Hayden et al., 2015).

More recently, the great galactic surveys have provided much information about external galaxies, even to make statistical analysis for disc galaxies, along the Hubble sequence. Figure 1.5 shows the resolved MDF for near spiral galaxies, showing the skewness also observed in the Galaxy. This skewness in the MDF cannot be explained only taking into account evolutionary chemical models, therefore it is necessary to consider the stellar radial migration produced by dynamical effects (Mejía-Narváez et al., 2020).

1.6 The Problem and Motivation

This PhD thesis project proposes a comprehensive, and at the same time, detailed study of the efficiency of important dynamical phenomenologies in disc galaxies, caused mainly by one large-scale non-axisymmetric features: spiral arms. Among the problems that will be tackled are radial mixing: radial migration and radial heating, and mimic their effects on the chemical elements distribution within discs, in different morphological types of galaxies. This phenomenology has been mainly studied from the theoretical point of view, in the Milky Way, where chemical elements distribution and dynamical studies are better observed. More recently, surveys such as CALIFA or SDSS/MaNGA, have allowed to observe with some confidence, phenomenologies such as radial migration, providing the information on kinematics and chemical elements distributions. Here, it is proposed then to extend theoretical studies within the Milky Way, to all type of disc galaxies in a near future.

The purpose is to understand what are the main factors that dictate the effectiveness and extension of radial migration (and its consequences in the chemical elements distribution for instance), in two different types of disc galaxies, from the early smoother types, to the cold late types. Morphological and dynamical differences among galaxies will for sure induce variations in the stellar dynamics.

This thesis is organized as follows. In chapter 2 are described the axisymmetric and spiral potentials, and the initial conditions that were used for the test-particles simulations. In chapter 3 are presented the rotation curves of the specific galactic models for Sa and Sc galaxies. In chapter 4 are presented the diagnostics to study the radial migration and their results. Finally, in chapter 5 are presented the discussion

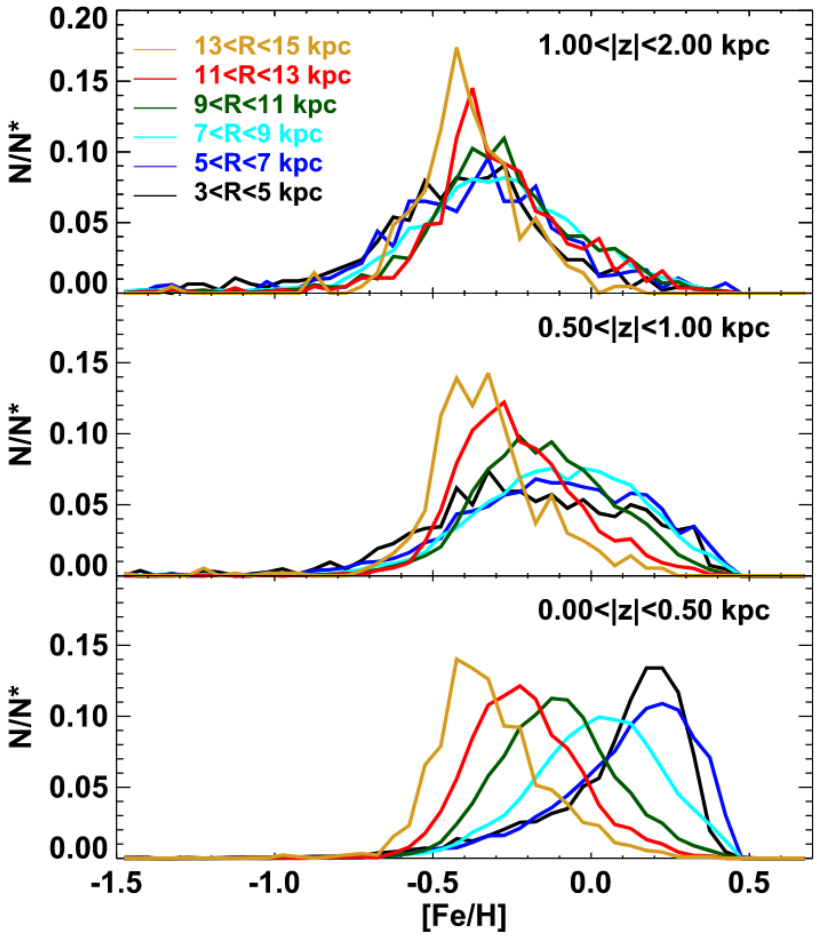

Figure 1.4: Observed MDFs of the Milky Way for different radii and height in z. The bottom panel shows the negative (inner radii) and positive (outer radii) skewness, signal of radial migration. Figure 5 taken from Hayden et al. (2015).

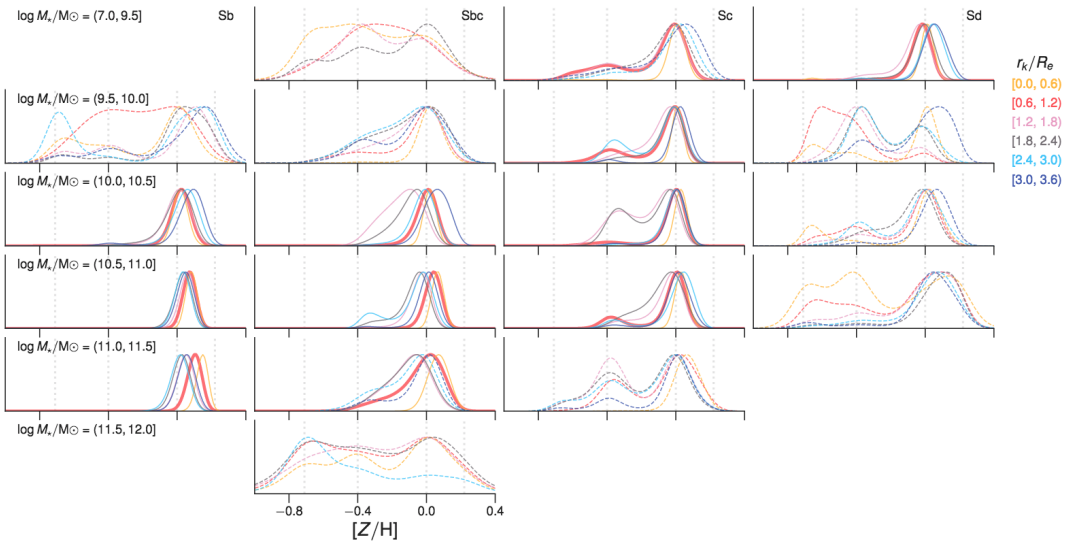

Figure 1.5: Observed MDF as a function of morphological type and different radii of a sub sample of near spiral galaxies, showing the negative (inner radii) and positive (outer radii) skewness, signal of radial migration. Figure 6 taken from Mejía-Narváez et al. (2020).

and conclusions achieved during this Ph.D. project.

Chapter 2

Test-particles simulations

Nowadays, theoretical studies of galactic dynamics need to be verified through numerical simulations designed beneath observational databases, resulting from great current surveys. In this context, the era of large databases and the theoretical predictions of galaxies provide a good theoretical-observational picture of the matter contained and observed in galactic structures.

There are two approaches to study the stellar dynamics in galaxies: stationary models and N-body simulations. The first one is based on a constant gravitational potential produced by the imposed axisymmetric and non-axisymmetric components. On the other hand, N-body simulations provides a complete evolutive description of the problem, in the sense of the Poisson and Boltzmann equations, hence, the galaxy relaxes itself and forms the structures allowed from its initial conditions. In N-body simulations the potentials and forces are changing at each moment and this is their main advantage, i.e., self-consistency: if there is a change in the density, there will be a change in the forces as well. Even the N-body simulations are a great tool, the resolution becomes important because the higher the resolution, the most expensive the simulation, and the non-adjustability represent disadvantages of those codes if a systematic study is needed.

Depending on what exactly is wanted to be achieved, the computational approach must be chosen. For the study of stellar dynamics, stationary models emerge as a suitable option. So, for the purpose of this work, test-particles simulations have been chosen. The aim is a systematic analysis of the individual stellar orbits affected by the structural and dynamical parameters of the spiral arms in a galaxy, that may produce radial migration.

In this sense, the conveniences of steady potentials are:

- Mathematically simple and computationally cheap.
- They are fully adaptable and allow to built-up specific galaxies by controlling their parameters values.

- The study of dynamics, in particular the stellar orbits can be developed with very high precision.
- Have a large number of particles with a low computational cost.
- These models are orbital-consistent, this means that orbits follow the imposed potentials given the orbital support.

In the next sections, the potentials for the axisymmetric background, the spiral arms and the initial conditions used to build different proposed galactic models are described, meanwhile in chapter 3 the particular cases of Sa and Sc galaxies, equations of motion and technical issues of the computational code are treated.

2.1 Axisymmetric potentials

The galactic model used in this work is represented by a 3D steady state composed potential. It consists of a Plummer (Plummer, 1911) for the bulge, a Miyamoto-Nagai (Miyamoto & Nagai, 1975) distribution for the disc, and for the dark matter halo, we adopted a Hernquist profile (Hernquist, 1990).

Considering the gravitational constant G=1, then, the Galactic units are fixed and the longitude is given in kpc, velocity in 10 km s^{-1}, mass in 2.32 $\times 10^7 M_\odot$, potential in 100 km^2 s^{-2}.

The density (ρ_B) for the bulge has the form:

$$\rho_B(R,z) = \frac{3b_1^2 M_B}{4\pi(R^2+z^2+b_1^2)^{5/2}}, \tag{2.1}$$

where M_B is the bulge mass, $R = \sqrt{x^2+y^2}$ and b_1 is the radial scale-length of the bulge. Then, the potential is:

$$\Phi_B(R,z) = -\frac{M_B}{\left(R^2+z^2+b_1^2\right)^{1/2}}, \tag{2.2}$$

and the forces are:

$$F_{Bx}(x,y,z) = -\frac{xM_B}{\left(R^2+z^2+b_1^2\right)^{3/2}}, \tag{2.3a}$$

$$F_{By}(x,y,z) = -\frac{yM_B}{\left(R^2+z^2+b_1^2\right)^{3/2}}, \tag{2.3b}$$

$$F_{Bz}(x,y,z) = -\frac{zM_B}{\left(R^2+z^2+b_1^2\right)^{3/2}}, \tag{2.3c}$$

For the disc, the expression for the density is:

$$\rho_D(R,z) = \frac{b^2 M_D}{4\pi} \frac{a_2^2 R^2 + \left(a_2 + 3\sqrt{z^2+b_2^2}\right)\left(a_2+\sqrt{z^2+b_2^2}\right)^2}{\left(R^2+\left(a_2+\sqrt{z^2+b_2^2}\right)^2\right)^{5/2}(z^2+b_2^2)^{3/2}} \tag{2.4}$$

where M_D is the disk mass, again $R = \sqrt{x^2+y^2}$ and a_2 and b_2 are the disk scale-lengths. The associated potential has the form:

$$\Phi_D(R,z) = -\frac{M_D}{\left(R^2+\left[a_2^2+\left(z^2+b_2^2\right)^{1/2}\right]^2\right)^{1/2}}, \tag{2.5}$$

It is interesting that depending on the selection of the a_2 and b_2 parameters can be represented a spherical system or a infinitely thin disk.

For the disc, the forces are:

$$F_{Dx}(x,y,z) = -\frac{xM_D}{\left(x^2+y^2+\left[a_2^2+\left(z^2+b_2^2\right)^{1/2}\right]^2\right)^{3/2}}, \tag{2.6a}$$

$$F_{Dy}(x,y,z) = -\frac{yM_D}{\left(x^2+y^2+\left[a_2^2+\left(z^2+b_2^2\right)^{1/2}\right]^2\right)^{3/2}}, \tag{2.6b}$$

$$F_{Dz}(x,y,z) = -\frac{zM_D\left(a_2+\left(z^2+b_2^2\right)^{1/2}\right)}{\left(x^2+y^2+\left[a_2^2+\left(z^2+b_2^2\right)^{1/2}\right]^2\right)^{3/2}\left(z^2+b_2^2\right)^{1/2}}, \tag{2.6c}$$

Finally the density (ρ_H) for the halo is given by:

$$\rho_H = \frac{M_H}{2\pi}\frac{a_3}{r}\frac{1}{(r+a_3)^3}. \tag{2.7}$$

M_H is the total halo mass, $r = \sqrt{x^2+y^2+z^2}$ and a_3 is a scale-length. Its potential is:

$$\Phi_H(r) = -\frac{GM_H}{r+a_3}, \tag{2.8}$$

and the corresponding forces are:

$$F_{Hx}(x,y,z) = -\frac{xGM_H}{r(r+a_3)^2}, \tag{2.9a}$$

$$F_{Hy}(x,y,z) = -\frac{yGM_H}{r(r+a_3)^2}, \tag{2.9b}$$

$$F_{Hz}(x,y,z) = -\frac{zGM_H}{r(r+a_3)^2}. \tag{2.9c}$$

2.2 Spiral arms: cosine potential

The Tight-Winding Approximation (TWA) is a two-dimensional potential that simulates the Lin & Shu (1964) spiral arms. It is based on the idea of density waves proposed by Lindblad (1960) and developed under the assumptions of a steady and low amplitude perturbations and small pitch angles. This expression is known as well as the cosine potential.

The cosine potential to model the spiral arms gravitational contribution is maybe the most used in the literature. It is a simple and complete analytic expression including its derivatives. A 3D spiral contribution is used in this work.

Here, the spiral arm potential with a vertical contribution was taken from Patsis & Grosbøl (1996),

$$\Phi_{\rm s}(R,\phi,z) = f(R)\cos[2\phi + g(R)]\mathrm{sech}^2\left[\frac{z}{z_0}\right], \tag{2.10}$$

where (R,ϕ,z) are the cylindrical coordinates in a non-inertial reference frame rotating with the pattern speed of the spiral arms, $f(R) = -AR\exp^{(-\epsilon_s R)}$ is the amplitude function of the perturbation being A and $\epsilon_s = \frac{1}{R_s}$ the amplitude and the inverse of the radial scale-length of the spiral arm. The geometry of the spiral pattern (*locus*) is given by

$$g(R) = -\frac{2}{N\tan i_p}\ln[1 + (R/R_s)^N], \tag{2.11}$$

where i_p is the pitch angle, R_s is the start position for the spiral arms and N is a constant that shapes the starting point of the spiral arms (Roberts et al., 1979). In the present work, N is set to 100 (see Pichardo et al. 2003 for more details).

Now, the forces for the spiral arms are:

$$F_{xs}(x,y,z) = AR^{-1}\exp^{\epsilon_s R}\left\{x\cos\left(\frac{2}{N\tan i_p}\ln\left[1+\left(\frac{R}{R_s}\right)^N\right]\right)\right.$$
$$\left(2-\frac{\epsilon_s(x^2-y^2)}{R}-\frac{x^2-y^2}{R^2}+\frac{4xyR^{N-2}}{\tan i_p\,(R_s^N+R^n)}\right)+$$
$$2\sin\left(\frac{2}{N\tan i_p}\ln\left[1+\left(\frac{R}{R_s}\right)^N\right]\right)$$
$$\left.\left(y-\frac{x^2y\epsilon_s}{R}-\frac{(x^2-y^2)xR^{N-2}}{\tan i_p(R_s^N+R^n)}-\frac{x^2y}{R^2}\right)\right\}\operatorname{sech}^2\left(\frac{z}{z_0}\right), \tag{2.12a}$$

$$F_{ys}(x,y,z) = AR^{-1}\exp^{\epsilon_s R}\left\{y\cos\left(\frac{2}{N\tan i_p}\ln\left[1+\left(\frac{R}{R_s}\right)^N\right]\right)\right.$$
$$\left(2-\frac{\epsilon_s(x^2-y^2)}{R}-\frac{x^2-y^2}{R^2}+\frac{4xyR^{N-2}}{\tan i_p\,(R_s^N+R^n)}\right)+$$
$$2\sin\left(\frac{2}{N\tan i_p}\ln\left[1+\left(\frac{R}{R_s}\right)^N\right]\right)$$
$$\left.\left(x-\frac{xy^2\epsilon_s}{R}-\frac{(x^2-y^2)yR^{N-2}}{\tan i_p(R_s^N+R^n)}-\frac{xy^2}{R^2}\right)\right\}\operatorname{sech}^2\left(\frac{z}{z_0}\right), \tag{2.12b}$$

$$F_{\rm zs}(x,y,z) = -AR\exp^{(-\epsilon_s R)}\cos\left[2\phi+-\frac{2}{N\tan i_p}\ln\left[1+(R/R_s)^N\right]\right]$$
$$\left(\frac{-2\operatorname{sech}^2\left(\frac{z}{z_0}\right)\tanh\left(\frac{z}{z_0}\right)}{z_0}\right). \tag{2.12c}$$

2.3 Initial conditions

To specify the positions and velocities of the disc test particles, the work of Hernquist (1993) is used, a technique resting in Jeans equations and for sake of completeness it is briefly described below.

Disc particle positions are determined once the density profile is specified by using, for instance, the von Newmann rejection technique (Press et al., 1992).

To determine their velocities we employ the second moment of the Collisionless Boltzmann Equation for an axisymmetric distribution:

$$v_c^2 - <v_\phi>^2 = \sigma_\phi^2 - \sigma_R^2 - \frac{R}{\Sigma}\frac{\partial(\Sigma\sigma_R^2)}{\partial R}, \tag{2.13}$$

where v_c is the circular velocity, v_ϕ is the azimuthal velocity, σ_ϕ and σ_R are the azimuthal and radial velocity dispersions, where it has been assumed that the velocity ellipsoid is aligned with the coordinate axes. This expression can be simplified even further by assuming:

$$\sigma_R^2(R) \propto \Sigma(R), \tag{2.14}$$

and that the azimuthal dispersion is given by the epicyclic approximation[1] as:

$$\sigma_\phi^2(R) = \sigma_R^2 \frac{\kappa^2}{4\Omega_c^2}, \tag{2.15}$$

where κ, the epicycle frequency is

$$\kappa = \left(4\Omega_c^2 + R\frac{d\Omega_c^2}{dR}\right), \tag{2.16}$$

and Ω_c, the angular frequency is

$$\Omega_c(R) = \left(\frac{1}{R}\frac{\partial\Phi}{\partial R}\right)^{1/2}, \tag{2.17}$$

where Φ is the background potential.

With these assumptions Equation 2.13 reduces to

$$v_c^2 - < v_\phi >^2 = \sigma_R^2 \left[\frac{\kappa^2}{4\Omega^2} - 1 - 2\frac{\partial(\ln\Sigma)}{\partial \ln R}\right]. \tag{2.18}$$

The radial dispersion velocity can be specified to a given radius, $R_\bullet$, using the Toomre $Q_\bullet$ parameter as a constraint

$$\sigma_R(R_\bullet) = Q_\bullet \frac{3.36G\Sigma}{\kappa^2}, \tag{2.19}$$

we take $Q_\bullet = 1.2$ at $R_\bullet = 2a_2$, where a_2 is the disc radial scalelength, to ensure local stability. The vertical dispersion is given by

$$\sigma_z^2 = \pi G\Sigma(R) b_2, \tag{2.20}$$

where b_2 is the disc vertical scaleheight.

Finally, the cartesian velocities can be obtained from Gaussian distributions with dispersions σ_z, σ_R and σ_ϕ and combining these last two with Equation 2.18 to obtain the azimuthal streaming velocity.

[1] For more details see section 3.2.3 of Binney & Tremaine (2008).

2.4 Caveats of the model

Even if the steady model is a powerful tool, there are some caveats that must be considered:

- The potentials are not self-consistent because they do not satisfy the Poisson and Boltzmann equations.
- They do not allow to study the galaxy evolution. They do not evolve in time.
- The cosine potential is a mathematical solution and it is restricted to be used with small pitch angles for the spiral arms. However, this is a first approximation and it is important to notice the fact of this supposition.
- The models only consider the rotation curve of the galaxies, instead of considering the entire kinematic maps.
- To set the initial conditions, it is important to focus in the fact that the epicyclic approximation is used, which means that the stellar orbits are considered near, or at least very circular.
- Even in this study the central regions of the galaxies are not being considered in the general analysis, it is important to mention that the cosine potential has a spurious central structure like a bar. Although, this spurious bar can be subtracted from the potential, it was left because the purpose of this project was focused on the effect of the spiral arms mainly at the corotation region.

Chapter 3

Galactic models

With the aim to study the influence of the spiral arms parameters on different types of isolated galaxies and quantify their effects on radial migration, a large number of simulations with test particles were carried out. In the particular case of this study, all the expressions for the potentials and the forces are completely analytical, and that is what reduces the computational time. Based on that, a large number of different types of galaxies can be modeled and it allows to do an exploration in the galactic parameters in both, the axisymmetric and non-axisymmetric potentials.

The orbits of the test particles are computed individually to study their behaviour, where the equations of motion (Binney & Tremaine, 2008):

$$\mathbf{a} = -\nabla\Phi - 2\Omega_{sp} \times \mathbf{v} - \Omega_{sp} \times (\Omega_{sp} \times \mathbf{r}) = -\nabla\Phi_{eff} - 2\Omega_{sp} \times \mathbf{v}, \tag{3.1}$$

are solved in the non-inertial reference frame system, rotating with a constant angular velocity given by the spiral arms pattern speed $\Omega_{\rm sp}$, where $\mathbf{a}$, $\Phi_{eff} = \Phi(r) - \frac{1}{2}|\Omega_{sp} \times \mathbf{r}|^2$, $\mathbf{v}$, $\mathbf{r}$, $-2\Omega_{sp} \times \mathbf{v}$ and $-\Omega_{sp} \times (\Omega_{sp} \times \mathbf{r})$ are the acceleration, effective potential, velocity, position, Coriolis and centrifugal forces respectively. The orbits of the test particles in this galactic model are followed by 5 Gyr using a Runge-Kutta integrator (Press et al., 1992) and the Jacobi energy

$$E_J \equiv \frac{1}{2}\mathbf{v}^2 + \Phi_{axi} + \Phi_{sp} - \frac{1}{2}|\Omega_{sp} \times \mathbf{r}|^2, \tag{3.2}$$

has a relative error $(E_{J_{ini}} - E_{J_{fin}})/E_{J_{ini}}$ around 10^{-14}. It is important to mention that the Jacobi energy is the only quantity that is conserved in the rotating reference frame and it is very useful to ensure the accuracy of the calculations: on the rotating reference frame, the potential is again time-independent. Each galactic model has its own set of resonances, depending on its characteristics and they are clarified later.

The extent of the spiral arms is principally due to an efficient exchange of angular momentum of the stars between the main resonances of the galaxies. Theoretically, the spiral arms go from the ILR to the OLR, but, in accordance with Contopoulos

& Grosbøl (1986), the maximum response in density is around the 4:1 resonance, for strong spiral arms and there, they must end due to the different orientations of the stellar orbits inside and outside this resonance. However, if the spirals are nearly weak, the gap formed precisely in 4:1 is small and the response in density can be prolonged until CR, meaning that the linear theory can be valid for weak spirals, where the strong non-linear effects are much less important than in the case of strong arms, causing gaps in 6:1, 8:1 and other resonances.

In all cases, the spiral arms are grown adiabatically during the first Gyr, to avoid a non-negligible transient response of the orbits resulting from an abrupt introduction of the spiral arms, which may lead to a spurious or non physical response. One Gyr is enough time to guarantee the smooth transition from a pure axi-symmetric potential to a potential where the non axi-symmetric one has been introduced, because the time needed to complete an entire orbit at the corotation resonance is smaller, about a half Gyr for the longest period.

Different lapses of time are used to explore the influence of the parameters on the stellar dynamics, clearly specified in each case. To study radial migration, the concept of "restricted migration" has been defined, having in mind the fact that if the Jacobi energy is conserved, then no net stellar migration can occur because this migration becomes cyclical. However, the effect of the spiral arms can be seen even in this conservative approach. Here, the radial migration refers to restricted migration.

Two different galactic models have been selected for two reasons: the Sa and Sc galaxies. The first one is that the Sa galaxies are more massive in general than Sc galaxies and the second one is that is more difficult to perturb the disk with spiral arms in a Sa than in a Sc galaxy. With this, the two extremes of the normal spiral galaxies are covered and in a certain way we can conclude that the possible results obtained in a Sb galaxy are between the results presented here. The adopted parameters of the axisymmetric galactic potential, for each morphological galaxy type, are summarized in Table 3.1. The background potential and the quotients between the masses are chosen like it was performed in Pérez-Villegas et al. (2012, 2013). It should be stressed that all Sa (Sc) models possess the same axisymmetric background, the difference among each model is in the spiral arm parameters as it is shown in Table 3.2. It is worth mentioning that, in the literature, there are many efforts to build mass models to fit observed rotation curves of spiral galaxies, for instance, a large number of fits can be consulted in Sofue (2016) and more recently in Kalinova et al. (2017) and reference therein.

This work studies a large number of models where some of the relevant parameters of the spiral arms potential such as the radial scale length, $R_{\rm sp}$, the pattern speed, $\Omega_{\rm sp}$, the pitch angle, $i_{\rm p}$, and the amplitude were varied. A fiducial case for each galactic type was adopted to compare its results with those obtained in the other models, in order to verify if the RM is larger or smaller, isolating the effects of each parameter of the spiral arms. Those fiducial cases are shaded in Table 3.2 respectively. The values for the radial scale-length of the spiral arms, $R_{\rm sp}$, are consistent with the results of the work of Mata-Chávez et al. (2019) who found that this scale is larger by 5% -

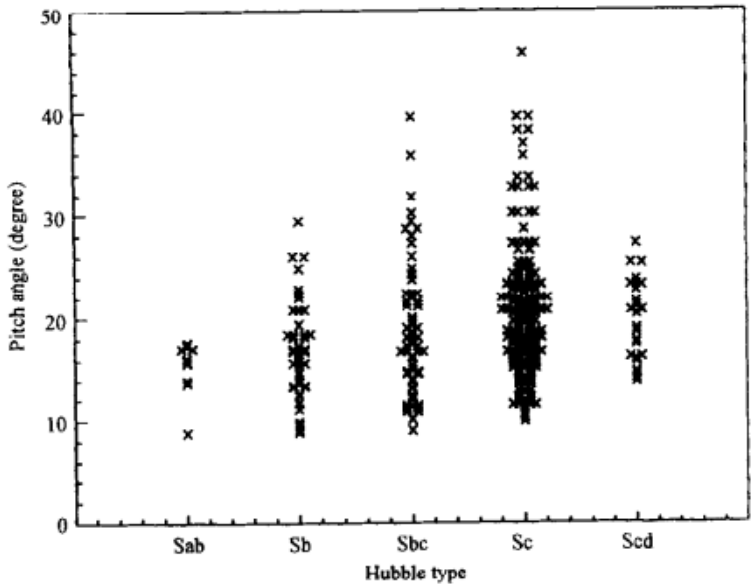

Figure 3.1: Pitch angle range of different galactic types. Taken from Ma et al. (2000).

40% than the radial scale-length of the disc of a Milky Way-like galaxy. Also, for the pitch angle (Figure 3.1) was included a maximum value of $i_{\rm p} = 40°$ (Ma et al., 2000; Yu & Ho, 2020) since larger values may lead to a model dominated by chaotic orbits, if the chaotic behaviour becomes pervasive, the orbits supporting the spiral arms will be destroyed (Pérez-Villegas et al., 2012, 2013, 2015). An interesting study where the pitch angle can be linked to the super massive black hole and the mass of the hosting galaxy is make by Davis et al. (2017, 2019).

Regarding the pattern speed values used here, they are consistent with the results by Fathi et al. (2009). They found in a sample of 10 spirals using the Tremaine–Weinberg method with $\rm H_\alpha$ observations, that the derived gas kinematics of disc galaxies can be used to derive the pattern speed with enough precision if the star formation is well spread in the galaxy.

Figure 3.2 shows the rotation curve and the contribution of each component of the Sa (top left panel) and Sc (top right panel) models. Following the expressions of the epicycle (Equation 2.16) and angular frequencies (Equation 2.17), the positions of the different resonances for each galactic model are estimated (bottom panel of Figure 3.2), depending on the spiral arms pattern $\Omega_{\rm sp}$ and when $\Omega_{\rm sp} = \Omega - \frac{\kappa}{2}$, $\Omega_{\rm sp} = \Omega + \frac{\kappa}{2}$, and $\Omega_{\rm sp} = \Omega$, the positions of the Inner Lindblad Resonance (ILR), the Outter Lindblad Resonance (OLR), and the corotation resonance (CR) are fixed, respectively. The positions of the resonances for both models are given in Table 3.3.

Figure 3.3 shows the test-particle distribution at $t = 0$ for the Sa and Sc galaxies. The number of particles in all simulations (Sa and Sc models) are one million distributed

Table 3.1: Axisymmetric parameters for the Sa and Sc models.

Parameters of the Sa and Sc galactic models		
Axisymmetric background		
Parameter	Value	
	Sa	Sc
b_1[kpc]	2.5	1
a_2[kpc]	7	5.3
b_2[kpc]	1.5	0.25
a_3[kpc]	33	36
V_c [km s^{-1}]	320	170
$M_B[10^{11} M_\odot]$	1.1	0.1
$M_D[10^{11} M_\odot]$	2.2	0.51
$M_H[10^{12} M_\odot]$	1.6	0.48

Table 3.2: Values for the parameters of the spiral arms model adopted for the Sa and Sc galaxies, to study their role in the radial migration in the disk.

Spiral arms parameters of the adopted models								
Parameter	A_{Sa}	B_{Sa}	C_{Sa}	D_{Sa}	A_{Sc}	B_{Sc}	C_{Sc}	D_{Sc}
R_{sp} [kpc]	7	8.75	7	7	5.31	6.64	5.31	5.31
i_p [°]	20	20	30	20	20	20	40	20
Ω_{sp} [km s^{-1}kpc^{-1}]	20	20	20	20	15	15	15	20
A [$km^2 s^{-2}$kpc^{-1}]	950	950	950	650	650	650	650	650

The blue and orange full columns show the fiducial cases for the Sa and Sc galaxies, respectively.

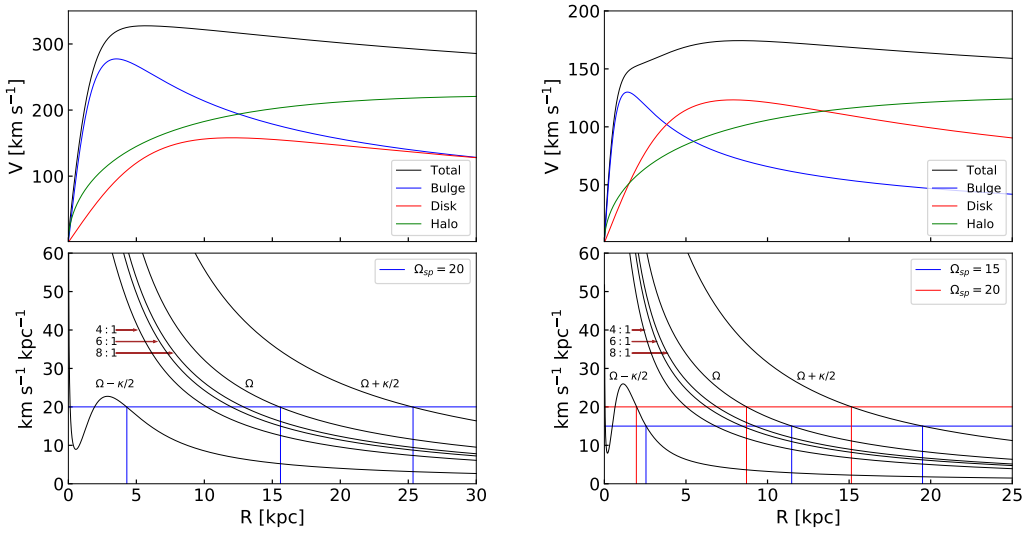

(a) ***Sa galaxy*** **(b)** ***Sc galaxy***

Figure 3.2: Top panel shows the rotation curve of the early and late type galaxy models for the axisymmetric background potential. Bottom panel shows the resonances positions of the models for the two pattern speeds used in this work (see Table 3.2).

Table 3.3: Resonance positions for the Sa and Sc models. Ω_{sp} for the Sa model is 20 km s^{-1} kpc^{-1} and for the model Sc there are two different pattern speeds, 15 and 20 km s^{-1} kpc^{-1}, fixing two different sets of resonances.

	Sa	Sc
Resonance	$\Omega_{sp} = 20$	$\Omega_{sp} = 15$ / 20
	Position [kpc]	
ILR	4.3	2.55 / 1.96
Inner 4/1	10.2	6.7 / 5
Inner 6/1	11.96	8.4 / 6.25
Inner 8/1	12.87	9.2 / 7
CR	15.6	11.48 / 8.71
Outer 4/1	18.33	13.7 / 10.42
Outer 6/1	19.24	14.56 / 11.17
Outer 8/1	21	16.26 / 12.42
OLR	25.35	19.5 / 15.14

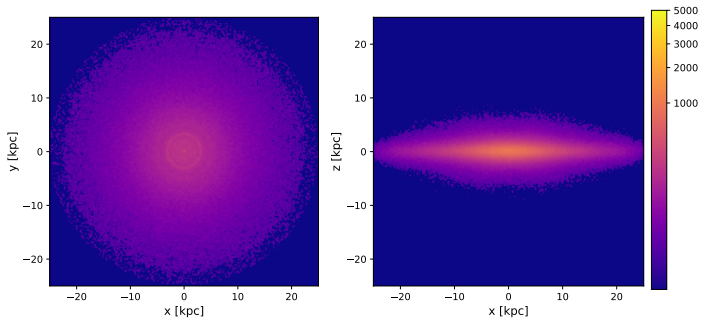

(a) ***Sa galaxy.***

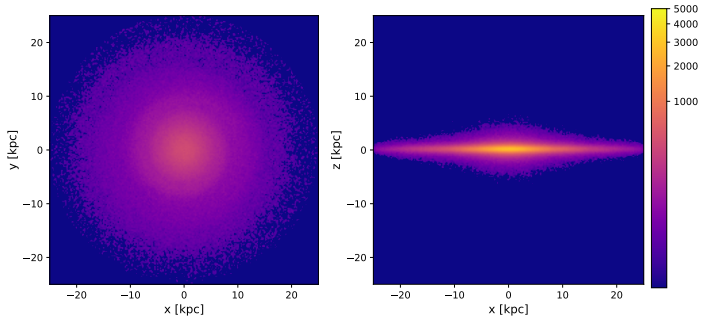

(b) ***Sc galaxy.***

Figure 3.3: Particle distribution at $t = 0$ for the Sa (top panels) and Sc (bottom panels) galaxy models. The colour bar shows the particle density.

in the disc, in accordance with the total potential formed by the bulge, disc and the dark matter halo.

Chapter 4

Results and Analysis

In order to analyse the radial migration, it is estimated, in three different times, the changes in angular momentum in the z-component $\Delta L_z = L_{z,f} - L_{z,i}$, radius $\Delta R = R_f - R_i$ and eccentricity $\Delta\text{ecc} = \text{ecc}_f - \text{ecc}_i$, from the initial time t_i to the final time t_f, where $L_{z,i}$, R_i, and ecc_i are the values of the each particle at t_i, and $L_{z,f}$, R_f, and ecc_f are the values of the same particle at t_f.

For the eccentricity, was taken the following expression (Arifyanto & Fuchs, 2006; Minchev et al., 2012a)

$$\text{ecc} = \sqrt{\frac{u^2 + \frac{\kappa^2}{\Omega^2}v^2}{r^2\kappa^2}}, \tag{4.1}$$

where u is the radial velocity respect to the galactic center, $v = V_c - V_\phi$ with V_c and V_ϕ the circular and tangential velocities respectively, κ is the radial epicyclic frequency, Ω is the angular frequency and r is the galactocentric distance at a given time.

Due to the fact that the cosine potential shows a spurious bar-like component in the central part (Pérez-Villegas, 2013) which might cause non physical variations of the eccentricity in the central region within 5 and 3 kpc (Sa and Sc galaxies), we avoid that region for our analysis.

4.1 Early-type spiral galaxy (Sa)

In this section, the results of ΔL_z ΔR and Δecc of the Sa galaxy type are presented. In each subsection, the results are discussed separately to show independently the effect of the spiral arms parameters on RM.

4.1.1 Changes in L_z

Figure 4.1 shows the ΔL_z along the radial distance, R_i, for the four models presented here. From top to bottom, each row represents the models A_{Sa}, B_{Sa}, C_{Sa}, D_{Sa}, where

the fiducial case is A_{Sa} (see Table 3.2) and from left to right, each column shows ΔL_z between different time intervals from 2-3, 3-4, and 2-4 Gyr.

For the model A_{Sa} (first row in Figure 4.1), around the CR region the particles have larger ΔL_z than in other radius, and that they are spread in a diagonal centered at this resonance. Around CR resonance, the particles have a maximum of $|\Delta L_z| \sim 2000$ kpc km s^{-1} in the three different intervals of time.

For the model B_{Sa} (second row in Figure 4.1), the scale length of the spiral arms is 1.25 times larger than for the model A_{Sa}, and $|\Delta L_z|$, ~ 2500 kpc km s^{-1}. Also it is clear that for this model the particles are spread along the radius in a wider way than for model A_{Sa}, and it does not depend on the time intervals, as can be seen in the different columns of the second row. In the third column, seems to be a larger change than in the other two intervals of time, and it can be attributed to the cumulative effect due a larger time of analysis.

Model C_{Sa}(third row in Figure 4.1) has a pitch angle larger by 10^{o} with respect to the model A_{Sa}, and $|\Delta L_z|$ is similar for all the time intervals and there is not a relevant difference respect to the model A_{Sa}, except that the diagonal formed around the CR is sharper than in model A_{Sa}.

Finally, for Model D_{Sa} (fourth row in Figure 4.1), the spiral arm amplitude has been decreased, then $|\Delta L_z| \sim 1500$ kpc km s^{-1} and is smaller compared to model A_{Sa}. Again, as it was expected, the larger ΔL_z and in the spread particles around CR in A_{Sa} (or smaller for D_{Sa}) are directly caused due to the amplitude of the spiral arms.

4.1.2 Changes in R

Figure 4.2 shows the changes in radii, ΔR, of the stellar orbits for the Sa models. Anew, the first row is the fiducial case (see Table 3.2). Some differences can be found in ΔR, among the time intervals of 1 and 2 Gyr around CR, but principally in the OLR, where the different behaviour is evident (third panel). Around the CR, ΔR is smaller than 10 kpc and the particles are spread in a diagonal, like they were spread in the ΔL_z analisys. In the first two panels, ΔR seems to be larger in OLR than in CR, however, the number of particles is small. Those large displacements were also observed in N-body simulations, where particles with very high radial migration were called "extreme migrators" by Halle et al. (2018). In particular, in those simulations, this behaviour was attributed to the bar OLR, while for our simulations, these are due to the spiral arms. For all times, ridges are connected with the position of the resonances, where the larger displacement is observed.

In the second row (B_{Sa}), ΔR is bigger than in A_{Sa}. In these panels, more particles near CR and OLR populate the zone around $\Delta R \sim 10$ kpc, either increasing or decreasing their radii, and these displacements are larger than in model A_{Sa}.

The row showing the results of model C_{Sa}, is very similar to the fiducial model, not only in magnitude of the changes in radii, but in the shapes formed around CR and the OLR. As can be seen for the case C_{Sa}, a different pitch angle has not much influence on the behavior of the stellar orbits, compared to the Model A_{Sa}. Around the region

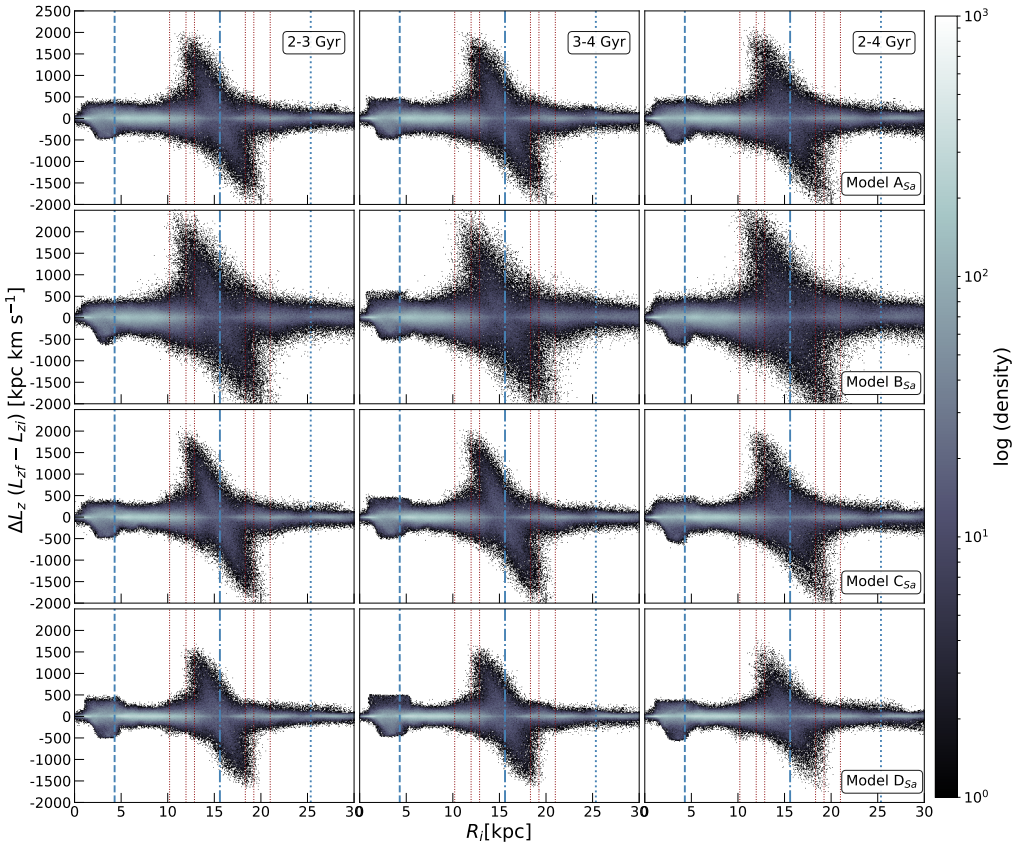

Figure 4.1: Changes in L_z, given in kpc km s^{-1}, for three different intervals of time (columns). Rows correspond to Models A_{Sa}, B_{Sa}, C_{Sa} and D_{Sa}, respectively. The blue dashed, dashed-dotted and dotted lines indicate the Inner, corotation and the Outer Lindblad resonances of the system, while the red ones designate the ultra-harmonic resonances (4:1, 6:1, 8:1, 1:8, 1:6, and 1:4, from left to right).

where the ultra harmonic resonances inside CR are located, approximately 13 kpc, a zone with ridges is formed, possibly due to the effect of these resonances.

The fourth row, where the amplitude has been decreased, the effect in the radii of the particles is even smaller than in the case C_{Sa}, confirming the findings in the L_z analysis. For the Model D_{Sa}, the largest displacements are slightly larger than 5 kpc (inward or outward) in the CR region, while in distances close to the OLR, $|\Delta R|$ can reach more than 10 kpc. This phenomenon were associated with the "extreme migrators", formerly discussed. In this case, a zone with ridges in radii around the ultra harmonic resonances ($\sim$ 13 kpc) is also formed.

Until now, the Model B_{Sa} shows the larger changes in both, L_z and R, which is a trace of the process of RM. Then, a larger R_{sp} produces more RM. To confirm this assumption, $|\Delta ecc|$ is analysed in the next section.

4.1.3 Changes in eccentricity

As a last diagnosis, Δecc is analysed and the results are shown in Figure 4.3, which has the same structure than Figure 4.1 and Figure 4.2. Recalling the fact that RM has large changes in L_z, R and small or none changes in ecc in the resonances regions, principally in CR, Figure 4.3 allows to figure out if the exploration of the parameters of the spiral arms produce RM or heating.

Among the three first rows of Figure 4.3, Model B_{Sa} is the one that has a larger R_{sp} and this results in a stronger spiral arm. Even when Δecc is larger in B_{Sa}, along the radial distance, it is clear that mainly in the CR resonance, changes in eccentricity are lower, or at least, remain as in the surroundings radii, where there is no change in L_z nor R and actually there is change in ecc. This is, in different places than in CR or OLR, there are heating instead of RM.

For the Model D_{Sa}, the effect is less clear, due to the weakness of the spiral arms compared to the fiducial case. However, the same phenomenon occurs in this model, like in the other previous three.

4.1.4 Quantifying radial migration

After examining $|\Delta L_z|$, $|\Delta R|$ and $|\Delta ecc|$ in the previous sections, though a systematic study of the spiral arms parameters, the evidence suggests that there is RM in all models, but the most important parameter is the radial scale length R_{sp} of the arms.

To quantify this affirmation, Figure 4.4 shows the histograms of the particles that originally were in a certain bin, and after 4 Gyr (from 0 to 4), were moved from its "birth" place. The size of the bins is 3 kpc and are normalized to the initial number of particles at t=0.

In the blue bin, the shape of the curves seems to be symmetrical with respect to the center, but in the rest, all the shapes of the curves show a positive (negative) skewness if the bin is before (after) the corotation radius. The green and red bins are particularly of interest, because they are around the CR resonance, where RM occurs, and this

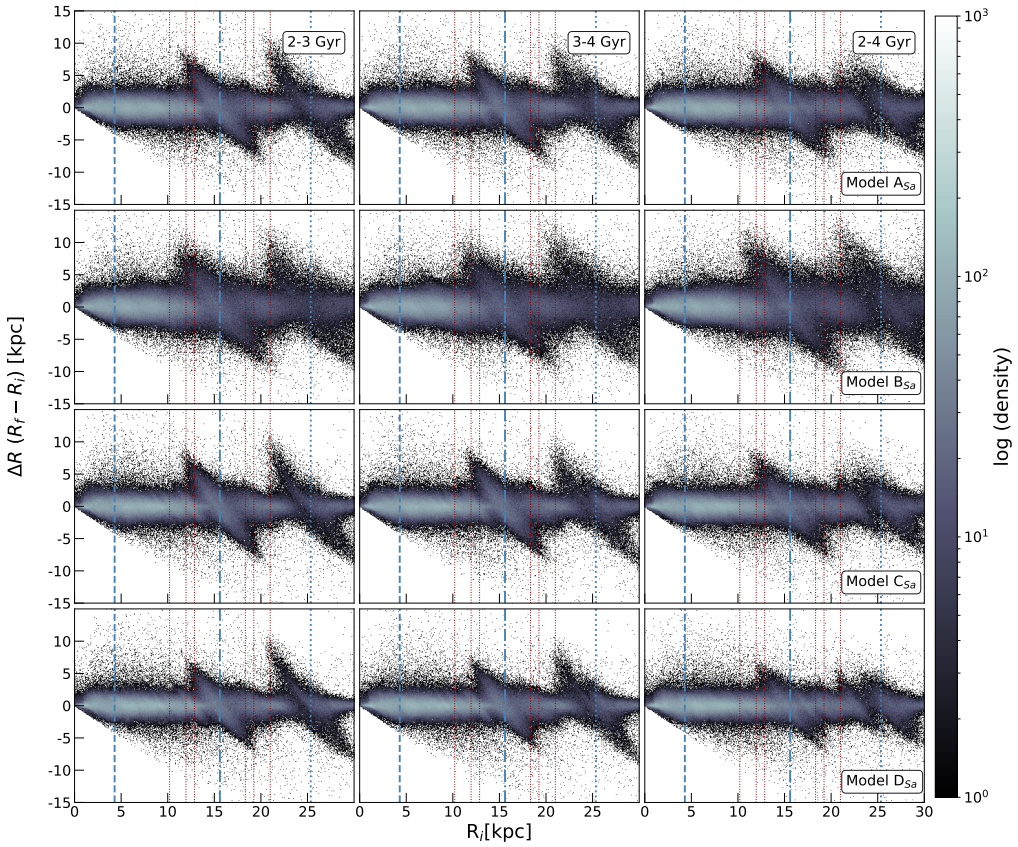

Figure 4.2: Changes in R as a function of the initial radius of the particles, given in kpc, for three different intervals of time (columns). Rows correspond to Models A_{Sa}, B_{Sa}, C_{Sa} and D_{Sa}, respectively. The blue dashed, dashed-dotted and dotted lines indicate the Inner, corotation and the Outer Lindblad resonances of the system, while the red ones designate the ultra-harmonic resonances (4:1, 6:1, 8:1, 1:8, 1:6, and 1:4, from left to right).

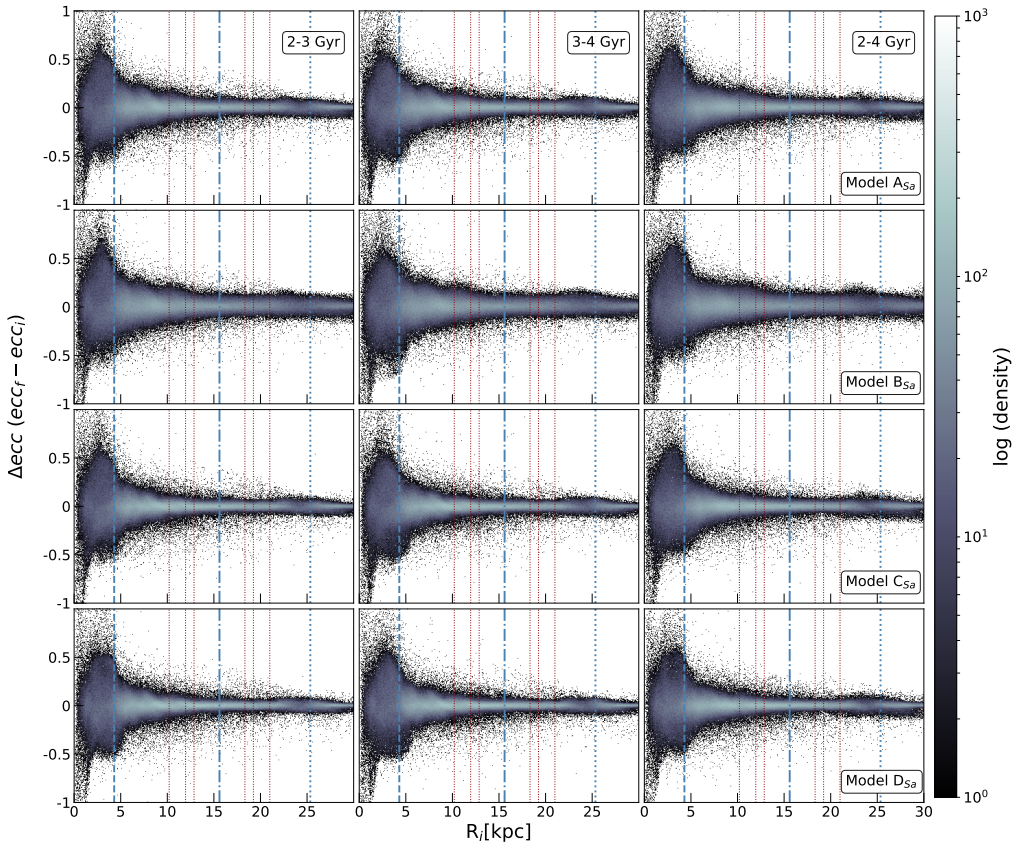

Figure 4.3: Changes in *ecc* as a function of the initial radius of the particles, for three different intervals of time (columns). Rows correspond to Models A_{Sa}, B_{Sa}, C_{Sa} and D_{Sa}, respectively. The blue dashed, dashed-dotted and dotted lines indicate the Inner, corotation and the Outer Lindblad resonances of the system, while the red ones designate the ultra-harmonic resonances (4:1, 6:1, 8:1, 1:8, 1:6, and 1:4, from left to right).

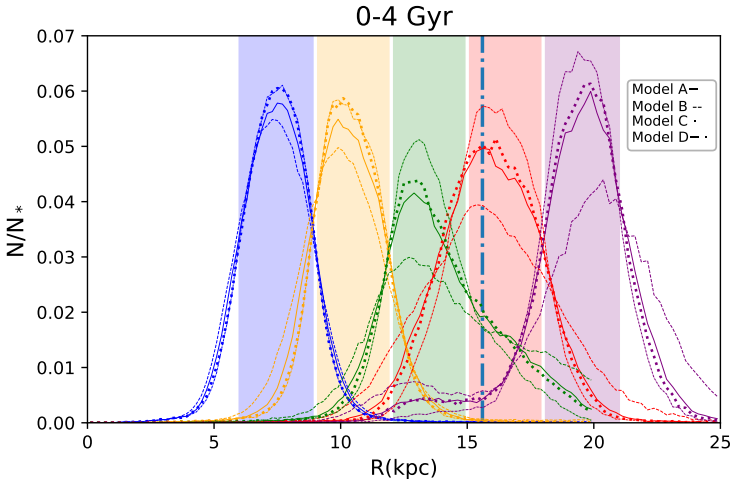

Figure 4.4: Histograms of the number of particles for all models consisting of 5 bins of 3 kpc length starting in 6 kpc. The blue dashed-dotted correspond to the corotation resonance of the system. Each coloured bin represents the initial radii at $t = 0$ and the curves are the distribution of the same particles at $t = 4$ Gyr. The green and red bins are located around the corotation resonance, it is clear that the dispersion of particles is larger in this zone than in other places for all models. However, Model B_{Sa} (dashed lines) spreads more particles originally in the green and red coloured bins to other places. Histograms are normalized to the initial number of particles at $t = 0$.

effect is more evident. The green and red dashed lines in the histogram in those bins, from 12 to 15 and 15 to 18 kpc, represent the case where R_{sp} is larger and move more particles than other models. Model A_{Sa} (solid line), in the bins around CR (green and red), moves $\sim$ 52 % of the particles originally placed there at t=0 Gyr, while Model B_{Sa} (dashed line), in the same bins, moves $\sim$ 60% of the particles. It means that the model B_{Sa} produces displacements in the stars of more than 3 kpc $\sim$ 10% higher than the Model A_{Sa}, which is in good agreement with the results achieved while $\Delta L_z, \Delta R$ and Δecc were studied.

4.1.5 Comparing spiral arms radial scale length

Given the results of the previous sections, it is clear that the spiral arms R_{sp} is the parameter with the highest migration production, and it has been established after the tests, that it is sufficient to analyze the change in L_z to compare different spiral scale lengths in the same galaxy.

Figure 4.5 shows ΔL_z for four different R_{sp} in different times. From top to bottom, the S_{sp} is increased from 0.5, 0.75, 1 and 1.25 times the disc radial scale length $a_2 = 7$ kpc, and the respective values are 3.5, 5.25, 7 and 8.75 kpc. It is clear that the effect on the test particles grows systematically from small changes around 500, up to five times, 2500 kpc km s^{-1} large ΔL_z.

4.1.6 Radial migration in a non-conservative potential

Until now, the concept of "restricted" radial migration has been studied. As the Jacobi energy is conserved, the radial migration is not durable and the particles oscillate around the corotation resonance. However, the results shown above are useful for determining the influence of the spiral arms on stellar orbits. According to SB02, a non-conservative potential is needed to produce effective migration.

Figure 4.6 shows the evolution of a Sa galaxy when the spiral arms are adiabatically introduced, from $t = 0$ to $t = 1$ Gyr, where the Jacobi energy is not conserved.

The green and red dashed lines in the nearest bins to CR (also green and red), exhibit the same behaviour than for the case where the Jacobi energy is conserved. The Model B_{Sa} disperses more particles than any other model. For the model A_{Sa}, the 41 and 47 % of the particles that initially where in the third and four bins, are spread outside to a new position, and in comparison with the model B_{Sa}, model A_{Sa} produces lees RM, because model B_{Sa} spreads 51 and 54 % of the particles in the same bins. This represents a higher RM by about 10 and 7% respectively.

4.1.7 Cuts in z direction

In agreement with the previous tests, any combination of parameters of the spiral arms produces radial migration, although the most important is R_{sp}. Initially, the particles have a distribution in radius, but also in the z direction. Similarly, the spiral arms have

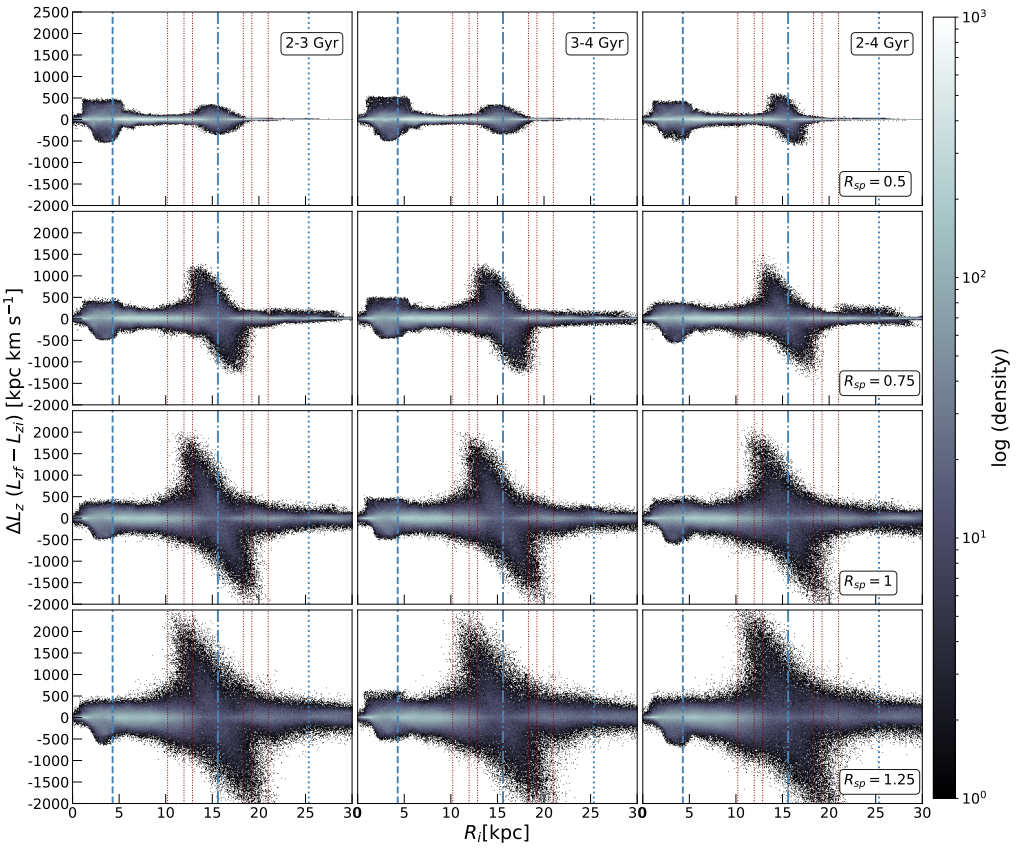

Figure 4.5: Changes in L_z as a function of the initial radius of the particles, for three different intervals of time (columns). Rows correspond to Models where R_{sp}= 0.5 a_2, 0.75 a_2, a_2, and 1.25 a_2, where a_2 = 7 kpc. The blue dashed, dashed-dotted and dotted lines indicate the Inner, corotation and the Outer Lindblad resonances of the system, while the red ones designate the ultra-harmonic resonances (4:1, 6:1, 8:1, 1:8, 1:6, and 1:4, from left to right).

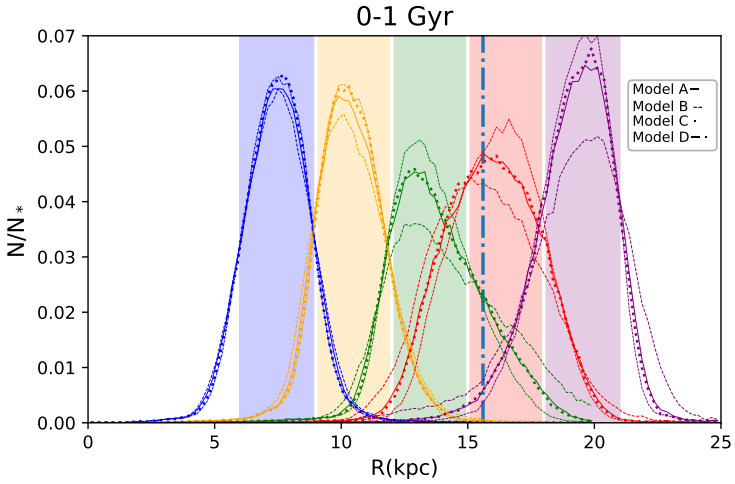

Figure 4.6: Histograms of the number of particles for all models consisting of 5 bins of 3 kpc length starting in 6 kpc. The blue dashed-dotted correspond to the corotation resonance of the system. Each coloured bin represents the initial radii at $t = 0$ and the curves are the distribution of the same particles at $t = 4$ Gyr. The green and red bins are located around the corotation resonance, it is clear that the dispersion of particles is larger in this zone than in other places for all models. However, model B_{Sa} (dashed lines) spreads more particles originally in the green and red coloured bins to other places. Histograms are normalized to the initial number of particles at $t = 0$.

a vertical contribution to the plane, represented by a hyperbolic secant. The question naturally arises whether all particles are affected in the same way if they are near the galactic plane or if they are above or below it.

Figure 4.7 shows ΔL_z of the particles with |z| < 0.5 kpc, roughly 70% and Figure 4.8 shows the particles with |z| > 0.5 kpc. In both cases, the density is lower than in Figure 4.1 (no z cuts), but it is clear that particles near the galactic plane are more affected and reach the larger ΔL_z, thus, the particles with small z are very prone to move radially due to the spiral arms, strongly modifying the stellar dynamics. If this were not the case, the particles with |z| > 0.5 kpc, would show large changes in L_z and this is not seen in Figure 4.7 and Figure 4.8, so this trend supports the previous claim.

Like in the case of the study of ΔL_z making cuts in z direction, Figure 4.9, Figure 4.10, Figure 4.11 and Figure 4.12, show the results of the equivalent analysis in ΔR and Δecc. It confirms the facts seen in ΔL_z. Qualitatively, the particles near the plane are more affected by RM than the particles that are at higher z.

Summary 1: Sa galaxy

- In all models for the Sa galaxy, always there is RM mainly at the CR, no matter the set of spiral arm parameters.
- In the models, the most important parameter for the production of RM is the spiral arm scale-length, tossing the 53 and $\sim 60\%$ for Model A_{Sa} and Model B_{Sa}, respectably, for their original bins at $t = 0$. Those particles preserve the circularity of their orbits, evidencing the existence of RM. These stellar movements cause positive (negative) skewness inside (outside) of the radial particle distribution around the CR.
- There are particles that move further than 10 kpc, inward or outwards, from their initial positions. These particles are called "extreme migrators" (Halle et al., 2018).
- The changes in Lz increase as a function of the spiral arm scale-length, R_{sp}. This states that RM depends on this parameter.
- If the potential is non-conservative, effective RM is produced in accordance with Sellwood & Binney (2002).
- The particles with $|z| < 0.5$ kpc are the most affected by the spiral arms and show the largest changes in L_z.

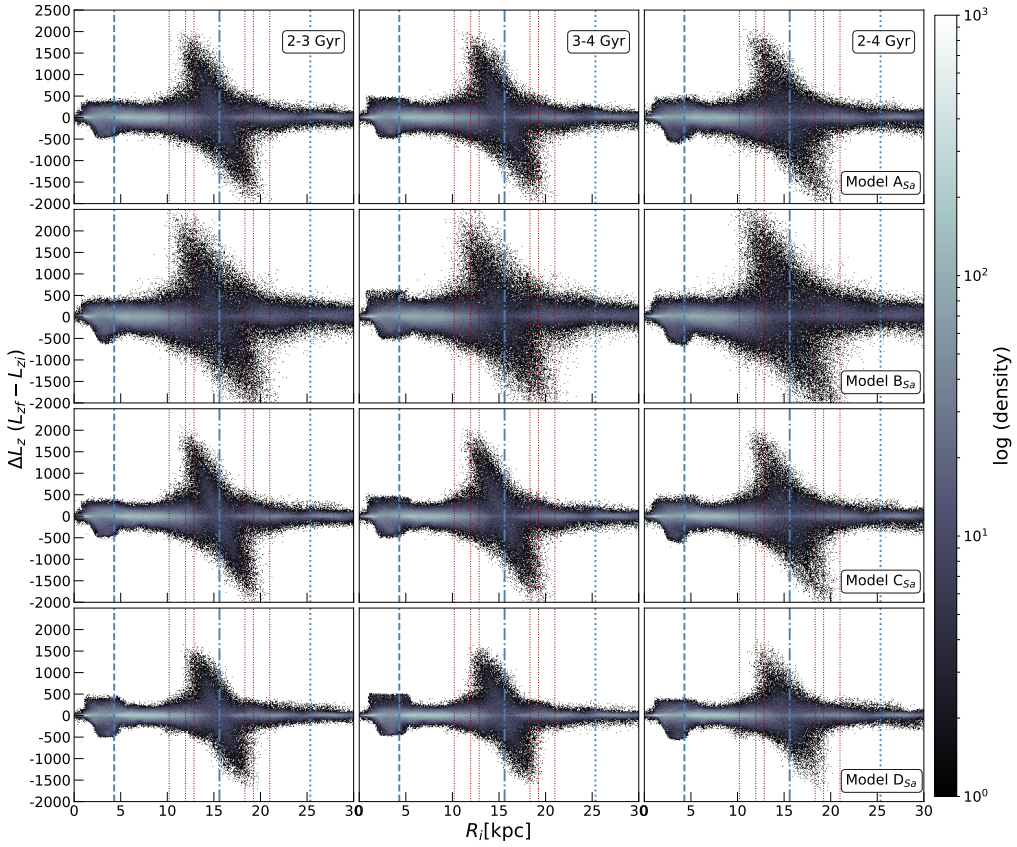

Figure 4.7: Changes in L_z as a function of the initial radius of the particles, given in kpc km s^{-1} with |z| $<$ 0.5 kpc, for three different intervals of time (columns). Rows correspond to Models A$_{Sa}$, B$_{Sa}$, C$_{Sa}$ and D$_{Sa}$, respectively. The blue dashed, dashed-dotted and dotted lines indicate the Inner, corotation and the Outer Lindblad resonances of the system, while the red ones designate the ultra-harmonic resonances (4:1, 6:1, 8:1, 1:8, 1:6, and 1:4, from left to right). Results are very similar to those seen in Figure 4.1, but the density is slightly lower and no substantial differences are observed.

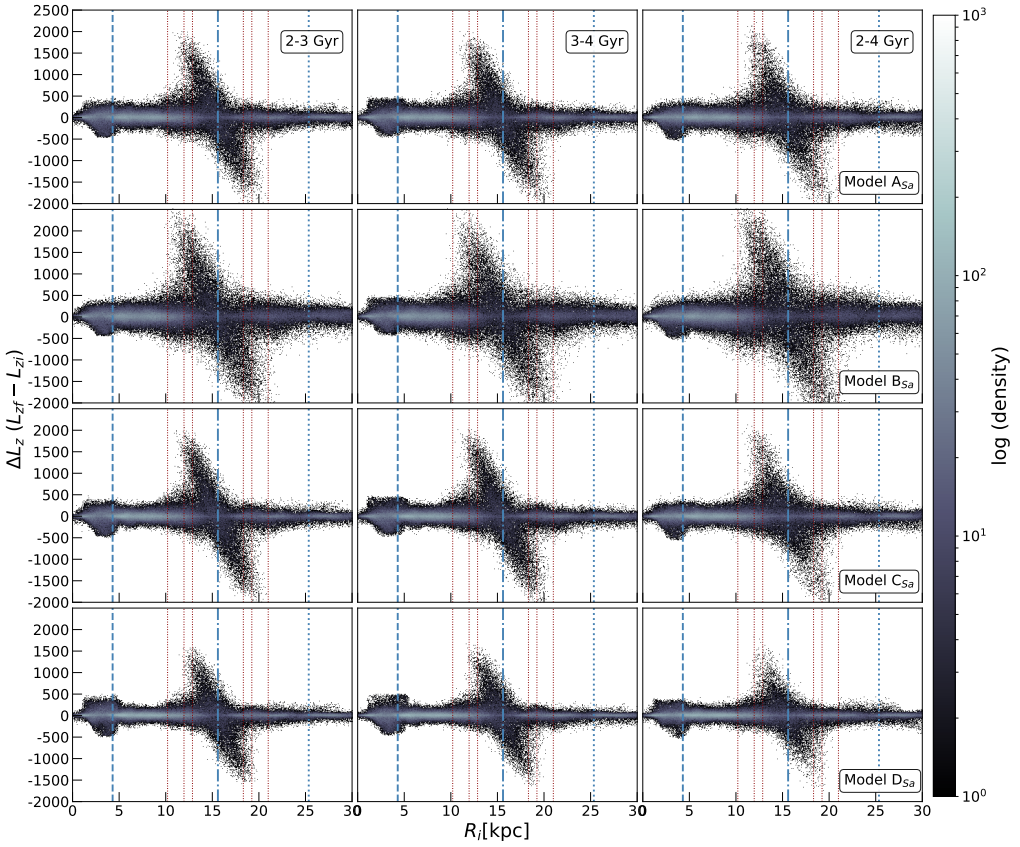

Figure 4.8: Changes in L_z as a function of the initial radius of the particles, given in kpc km s^{-1} with |z| $>$ 0.5 kpc, for three different intervals of time (columns). Rows correspond to Models A$_{Sa}$, B$_{Sa}$, C$_{Sa}$ and D$_{Sa}$, respectively. The blue dashed, dashed-dotted and dotted lines indicate the Inner, corotation and the Outer Lindblad resonances of the system, while the red ones designate the ultra-harmonic resonances (4:1, 6:1, 8:1, 1:8, 1:6, and 1:4, from left to right). Results are very similar to those seen in Figure 4.7, but the density is slightly lower and no substantial differences are observed.

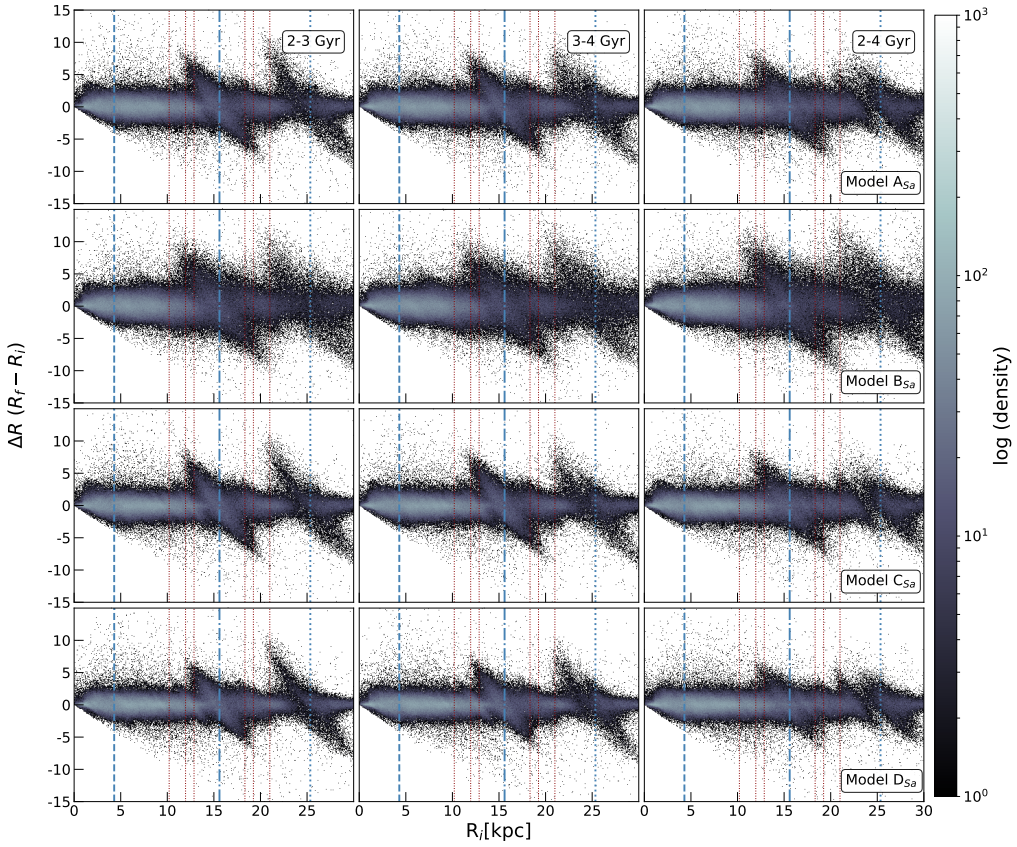

Figure 4.9: Changes in R as a function of the initial radius of the particles, given in kpc, for three different intervals of time (columns). Rows correspond to Models A_{Sa}, B_{Sa}, C_{Sa} and D_{Sa}, respectively. The blue dashed, dashed-dotted and dotted lines indicate the Inner, corotation and the Outer Lindblad resonances of the system, while the red ones designate the ultra-harmonic resonances (4:1, 6:1, 8:1, 1:8, 1:6, and 1:4, from left to right). Here are shown all the particles with $|z| < 0.5$ kpc (about the 70% of the total) and the density falls compared with Figure 4.2.

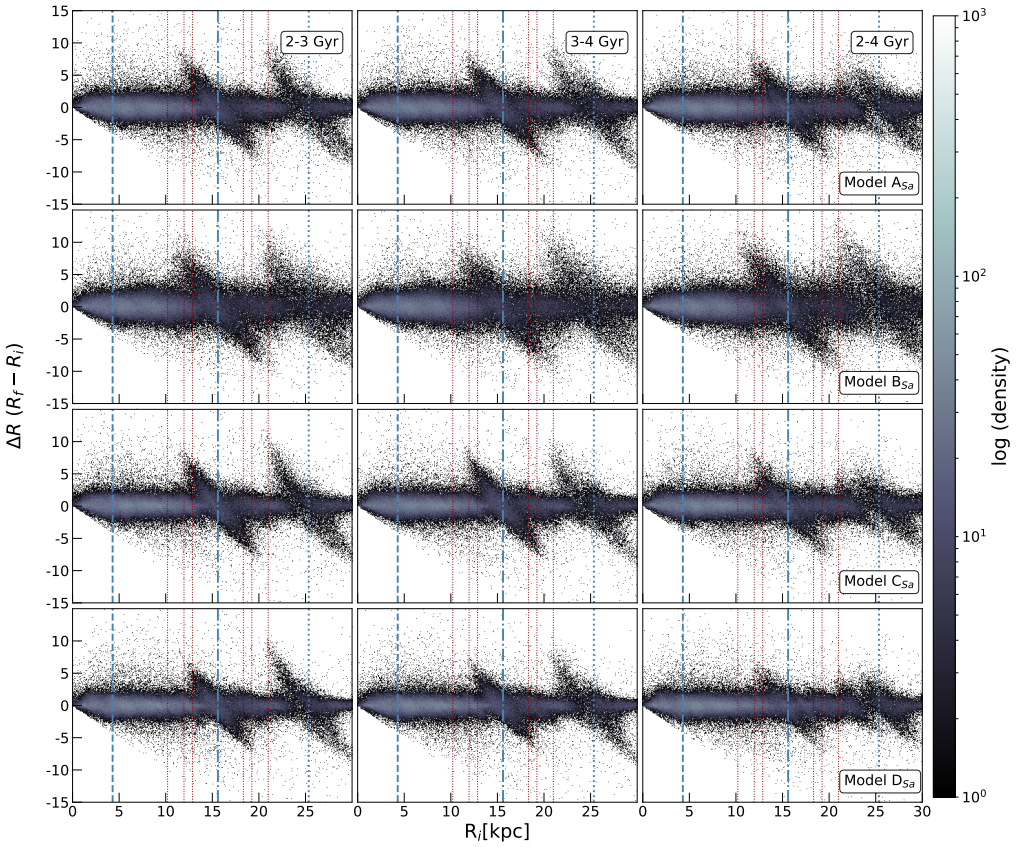

Figure 4.10: Same as figure Figure 4.9. Here are shown the particles with $|z| > 0.5$ kpc ($\sim 30\%$ of the total).

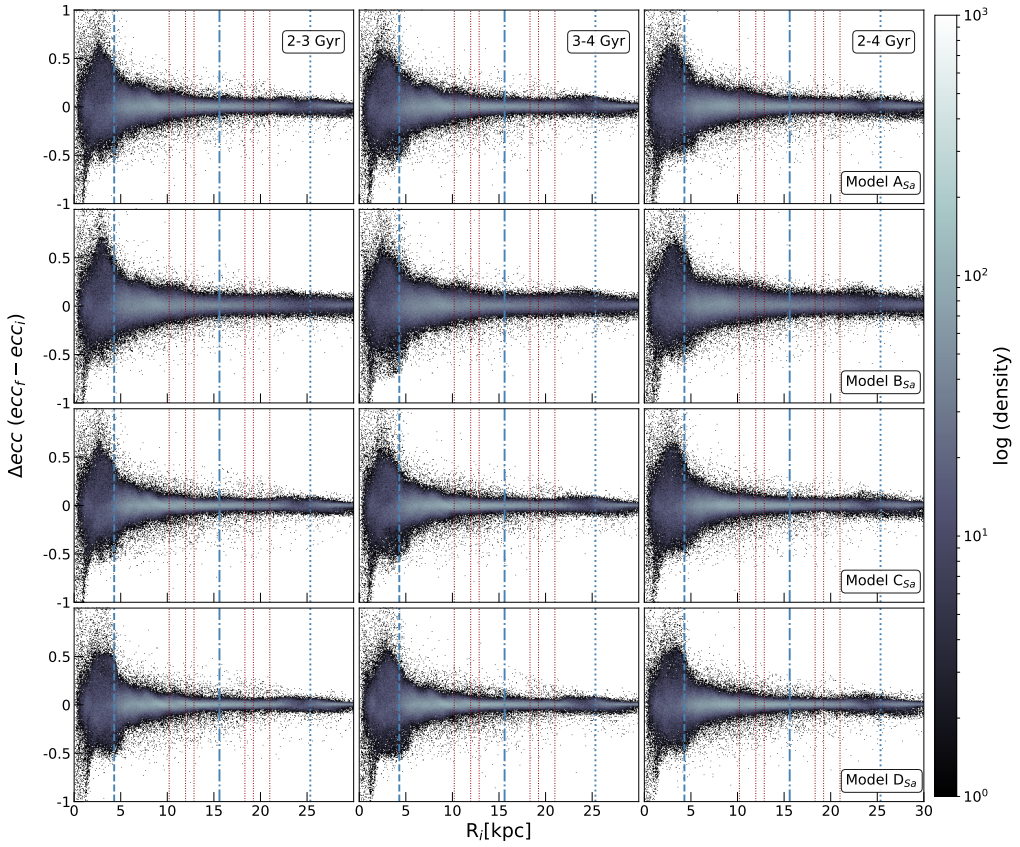

Figure 4.11: Changes in *ecc* as a function of the initial radius of the particles, for three different intervals of time (columns). Rows correspond to Models A_{Sa}, B_{Sa}, C_{Sa} and D_{Sa}, respectively. The blue dashed, dashed-dotted and dotted lines indicate the Inner, corotation and the Outer Lindblad resonances of the system, while the red ones designate the ultra-harmonic resonances (4:1, 6:1, 8:1, 1:8, 1:6, and 1:4, from left to right). All particles with $|z| < 0.5$ kpc (about 70% of the total) are plotted here and in comparison with Figure 4.3, the density decreases, but the general behaviour remains.

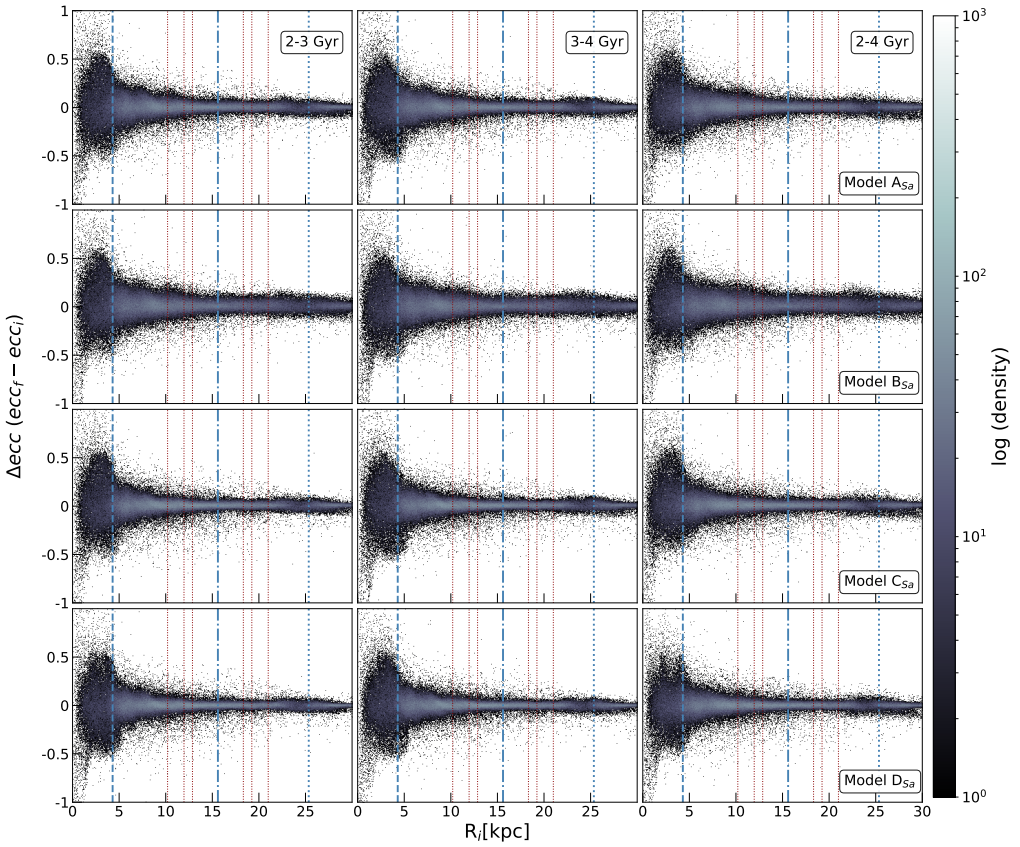

Figure 4.12: Same as Figure 4.11. Here are shown all the particles with $|z| > 0.5$ kpc ($\sim$ 30% of the total).

4.2 Late-type spiral galaxy (Sc)

4.2.1 Changes in L_z

Figure 4.13 shows the ΔL_z as function of the initial galactocentric distance, R_i, for the S_c models. From top to bottom, each row corresponds to the evolution of the different models as described in chapter 3, and from left to right, each column shows ΔL_z between different time intervals 2-3, 3-4, and 2-4 Gyr.

For the fiducial model A_{Sc} (first row in Figure 4.13), the particles showing larger changes in ΔL_z are seen around the CR region, where they are spread in a diagonal centered at this resonance, independently of the chosen time interval, with a maximum of $|\Delta L_z| \sim 1000$ kpc km s^{-1}. When the difference in time is 1 Gyr (two first panels), the ΔL_z seems to have a similar behaviour, but for the difference in time of 2 Gyr (third panel), the accumulative effect could be the responsible of the larger changes seen in ΔL_z and the spread in R_i.

Looking at Model B_{Sc}, for which the radial scale, $R_{\rm sp}$, of the spiral arms has been increased by around 25% with respect to the fiducial model A_{Sc} (second line in Figure 4.13), it shows an increase in ΔL_z, clearly exceeding the maximum value found in Model A_{Sc}, no matter the time. Around CR, not only larger changes in ΔL_z than in Model A_{Sc} occur, but also a larger spread in R is seen. In the surrounding of CR, a zone of dispersed particles is formed.

Regarding Model C_{Sc} (third line in Figure 4.13), which has a pitch angle larger by a factor of two with respect to the fiducial Model A_{Sc}, ΔL_z seems to have a similar evolution for all the considered time intervals and is only slightly larger than the changes shown in Model A_{Sc}. Finally, for Model D_{Sc} (fourth line in Figure 4.13), similar to the fiducial Model A_{Sc} but with a lager pattern speed, $\Omega_{\rm sp}$, for the spiral arms, it can be seen that $|\Delta L_z|$ is similar to the one observed in the CR of Model A_{Sc}. Notice that the location of the CR radius is closer to the centre and they cannot be compared directly, however, the overall behaviour is similar.

4.2.2 Changes in R

Figure 4.14 is similar to Figure 4.13, but it shows the change in radii, ΔR, of the stellar orbits. In the first row (the fiducial Model A_{Sc}), ΔR is larger than 5 kpc for time intervals of 1 Gyr around CR and the OLR and less than 5 kpc in other regions. The cumulative effect in two Gyr is clearly seen in the third panel, where ΔR can reach up to 10 kpc in the OLR region. It seems that OLR has a stronger effect compared to CR, however, the number of particles spread in OLR is fewer than in CR. Those large displacements were discussed in 4.1.2

For Model B_{Sc} (second row), ΔR is bigger than in the fiducial Model A_{Sc}. In these panels, particles near CR and OLR can travel more than 10 kpc (inward or outward), these displacements are significantly larger than those observed in model A_{Sc}. On the

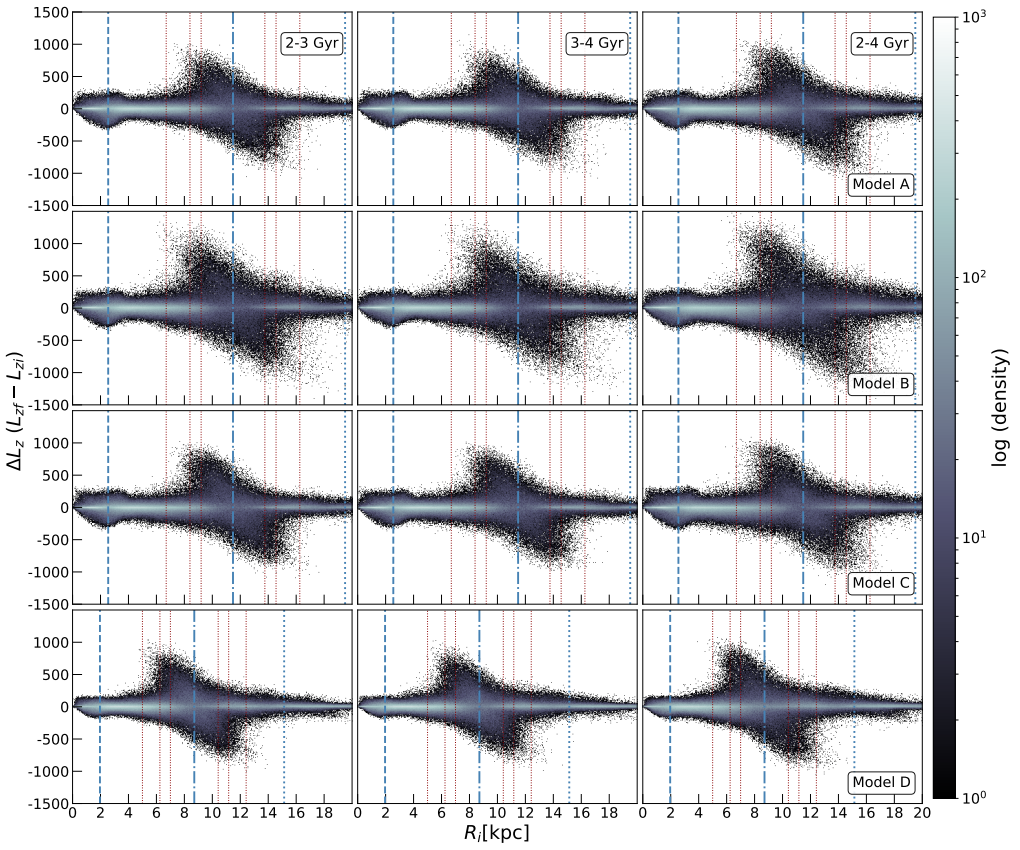

Figure 4.13: Changes in L_z as a function of the initial radius of the particles, given in kpc km s^{-1}, for three different intervals of time (columns). Rows correspond to Models A_{Sc}, B_{Sc}, C_{Sc}, and D_{Sc}, respectively. The blue dashed, dashed-dotted, and dotted lines indicate the Inner, corotation and the Outer Lindblad resonances of the system while, the red ones designate the ultra-harmonic resonances (4:1, 6:1, 8:1, 1:8, 1:6, and 1:4, from left to right). The colour bar shows the particle density in a logarithm scale.

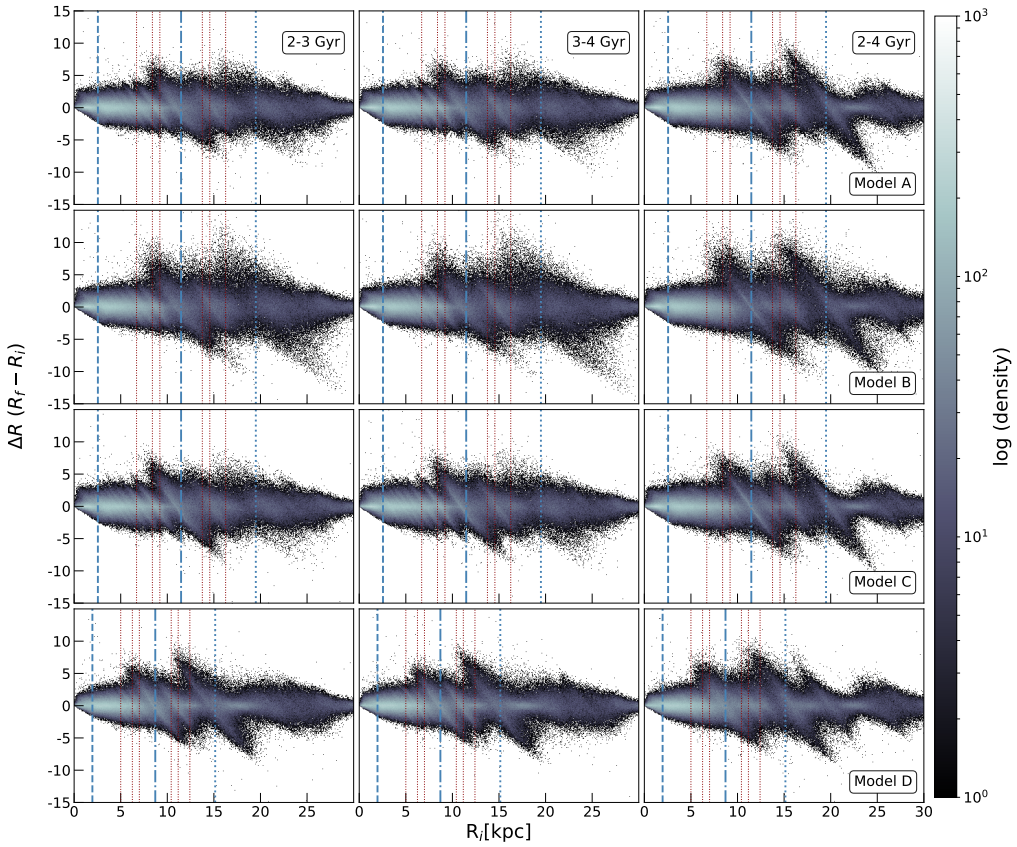

Figure 4.14: Changes in R as a function of the initial radius of the particles, given in kpc, for three different intervals of time (columns). Rows correspond to Models A_{Sc}, B_{Sc}, C_{Sc} and D_{Sc}, respectively. The blue dashed, dashed-dotted and dotted lines indicate the Inner, corotation and the Outer Lindblad resonances of the system, while the red ones designate the ultra-harmonic resonances (4:1, 6:1, 8:1, 1:8, 1:6, and 1:4, from left to right).

other hand, both Models C_{Sc} and D_{Sc} show a similar global behaviour than Model A_{Sc}, with small differences. For instance, the ridges around the resonances in Model C_{Sc} are more well defined than in Model A_{Sc} while, in Model D_{Sc}, the change ΔR in the OLR is larger than in the region around corotation.

Despite all parameters of the spiral arms play a role in the process of radial migration, clearly, the most relevant (like in the *Sa* models), is the radial scale length $R_{\rm sp}$ of the spiral arms (Model B_{Sc}), leading to larger changes in L_z and R, as is shown in the results of Figure 4.13 and Figure 4.14, respectively.

4.2.3 Changes in eccentricity

To disentangle between radial migration and radial heating, the changes in eccentricity are determined as defined in Equation 4.1. Figure 4.15 shows Δecc as a function of the initial radii R_i at the same three time intervals shown in Figure 4.13 and Figure 4.14. It can be seen that in the central region Δecc increases by large values but it is due, in part, to the cosine spiral arms model since it has a non-physical bar-like behaviour and, for the purposes of this study, this region is ignored. However, for all models around CR, large changes in L_z (Figure 4.13) are observed, but small changes in ecc (Figure 4.15) in CR and other resonances like the OLR, indicating that the stellar orbits can move inwards or outwards preserving nearly circular orbits which is precisely the mechanism of radial migration.

4.2.4 Quantifying radial migration

In order to quantify the effect of modifying the value of the parameters of the spiral arms in the radial migration, the initial and the final position of each particle in the S_c models are analysed. Figure 4.16 shows the particle distribution from $t = 0$ to $t = 4$ Gyr. Each coloured 3 kpc-size bin represents the initial position of the particles, and the colour curves are the final particle distribution. Each curve is normalized to the number of particles in its corresponding bin at $t = 0$ Gyr. The solid, dashed and dotted lines correspond to Model A_{Sc}, Model B_{Sc} and Model C_{Sc}, respectively. For clarity, Model D_{Sc} is shown separately since the pattern speed of the spiral arms is larger in this case, and the position of its resonances are closer to the central region (Figure 4.16, bottom panel). It can be noticed from this figure that after 4 Gyr, the shapes of the curves of the first bins closer to the inner region of the galaxy are similar and roughly symmetrical, suggesting that radial migration is small. However, the situation is completely different for the bins closer to the corotation resonance. All the shapes of the curves show a positive (negative) skewness if the bin is before (after) the corotation radius, indicating that radial migration is operating and moving particles to larger (smaller) distances from their original positions. This is particularly more clearly seen in Model B (dashed-line, upper panel of Figure 4.16). Also, some positive skewness can be appreciated in Model D_{Sc} for the curve just before the OLR with particles moving up to 10 kpc. These results are in agreement with the results

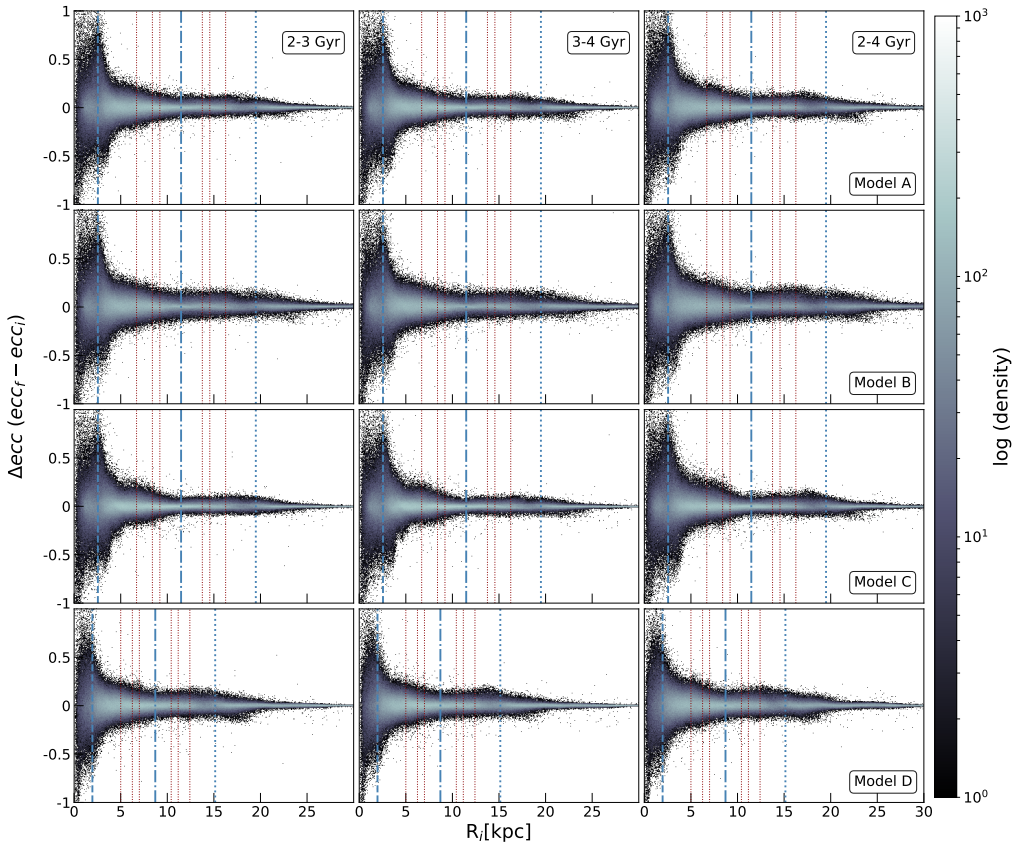

Figure 4.15: Changes in eccentricity as a function of the initial radius of the particles, for three different intervals of time given by the columns as in Figure 4.13. Rows indicate Models A_{Sc}, B_{Sc}, C_{Sc} and D_{Sc}. The blue dashed, dashed-dotted and dotted lines are the Inner, corotation and the Outer Lindblad resonances of the system, while the red ones designate the ultra-harmonic resonances (4:1, 6:1, 8:1, 1:8, 1:6, and 1:4, from left to right).

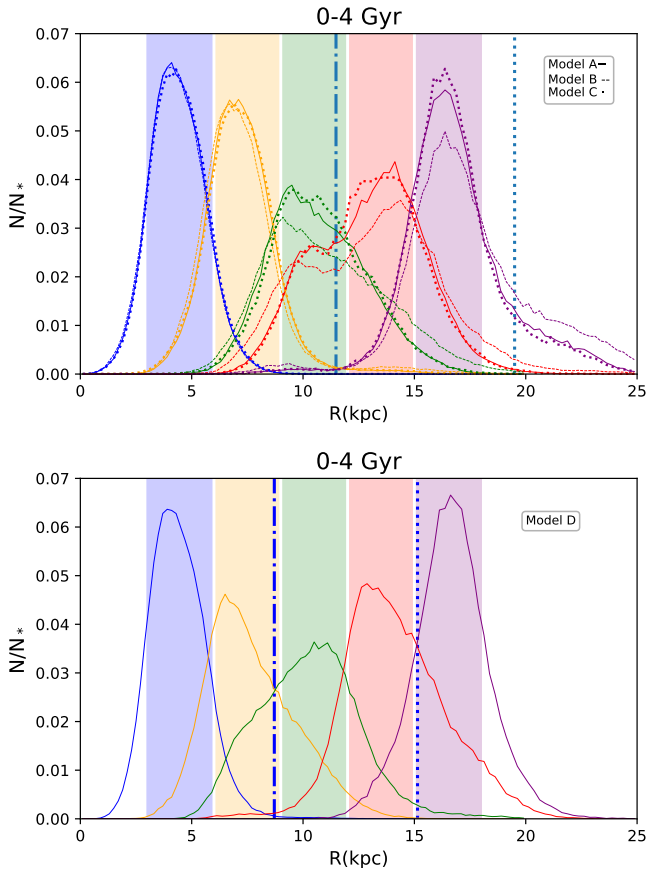

Figure 4.16: Top row shows the histograms of the number of particles for Models A_{Sc}, B_{Sc} and C_{Sc} consisting of 5 bins of 3 kpc length starting in 3 kpc. The blue dashed-dotted and dotted lines correspond to the corotation and the Outer Lindblad resonances of the system. Each coloured bin represents the initial radii at $t = 0$ and the curves are the distribution of the same particles at $t = 4$ Gyr. The green and red bins are located around the corotation resonance, it is clear that the dispersion of particles is larger in this zone than in other places for all models. However, model B_{Sc} (dashed lines) spreads more particles originally in the green and red coloured bins to other places. Bottom row is the same than top row, but only for model D_{Sc}, where the resonances are placed in other zones due to the different pattern speed of the spiral arms. Histograms are normalized to the initial number of particles at $t = 0$.

found in previous subsections. This skweness could be used to indirectly determine the position of the principal resonances and, if the rotation curve of the galaxy is known, the pattern speed could be estimated.

For Model A_{Sc}, the 50 , 55 and 41 % of the particles originally found at the third, fourth and fifth bins (9-12, 12-15 and 15-18 kpc, respectively) at t = 0 Gyr, are spread beyond their initial bin. These numbers are slightly different for the Model C_{Sc}, but not enough to make a big difference. Instead, Model B_{Sc} has 59, 62 and 50 % of particles that leave their original radial bin, showing a difference in the behaviour of the particles around the main resonances of the system. This model has an increment about 10% of particles that migrate compared to the Model A_{Sc}. For the Model D_{Sc}, the bins around CR are the second, third, and fourth, with a spread particles of 50, 47, and 34 %, respectively. As it was mentioned before, this comparison is not straightforward due to the differences in the resonances positions.

Summary 2: Sc galaxy

- All models for the Sc galaxy show radial migration mainly at the CR, no matter the combination of parameters.
- As it was seen in the Sa galaxy models, also the spiral arm scale-length produces a larger RM than other spiral arm parameters in the Sc models. For Model A_{Sc}, $\sim$ 50% of the particles around CR move from their original place, and for the Model B_{Sc} the percentage is increased by 10%. Again, the particle distributions have a positive (negative) skewness inside (outside) the surroundings of CR.
- There are particles that move more than 10 kpc, inward or outwards. These particles are known as "extreme migrators" Halle et al. (2018).

4.3 Comparison of radial migration in Sa and Sc galaxies

Even when the two galactic models are quite different, it is interesting to compare the values of RM between them. The main results are discussed in Summary 1 and Summary 2, where it can be confirmed that RM affects the hot and the cold dynamical systems almost in the same proportion.

In the fiducial models (A_{Sa} and A_{Sc}), the produced RM around CR is larger for the Model A_{Sc} than for the Model A_{Sa}, based on the displaced particles from their original bins for both galaxies. Figure 4.17 shows the RM for each galaxy and the bins are 3 kpc sized.

In order to make a more accurate comparison between Sa and Sc galaxies, the particles distributions were normalized by their corresponding CR. Then, the comparison

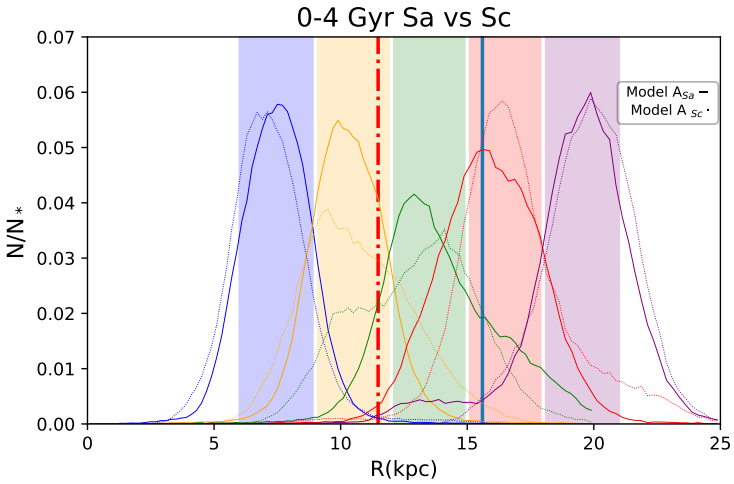

Figure 4.17: Histograms of the number of particles for the fiducial models, consisting of 5 bins of 3 kpc length starting in 6 kpc. The blue solid line corresponds to the corotation resonance of the Sa galaxy and the dashed-dotted red line corresponds to the corotation resonance of the Sc galaxy. Each coloured bin represents the initial radii at $t = 0$ and the curves are the distribution of the same particles at $t = 4$ Gyr. The green and red bins are located around the corotation resonance, and it is clear that the dispersion of particles is larger in this zone than in other places (see 4.1.4 and 4.2.4). However, Model A_{Sc} (solid line) spreads more particles originally in the green and red coloured bins to other places, than Model A_{Sa} (dotted line), in their respective CR. Histograms are normalized to the initial number of particles at $t = 0$.

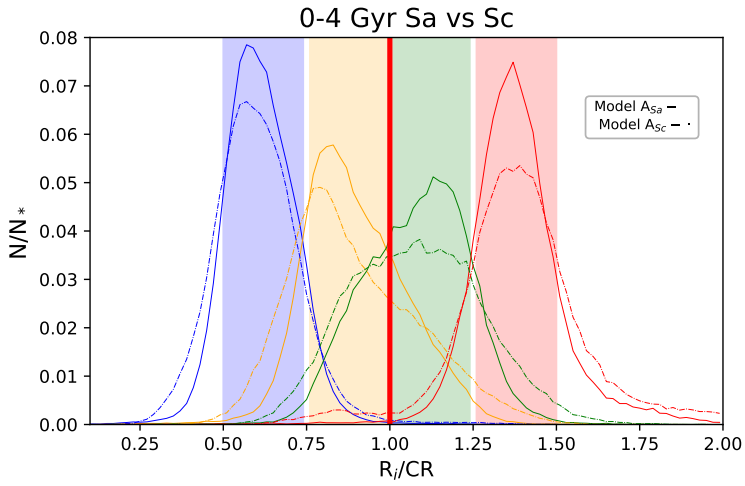

Figure 4.18: Histograms normalized to the corresponding CR for the Sa and Sc galaxies. The red vertical line is the position of the two normalized CR.

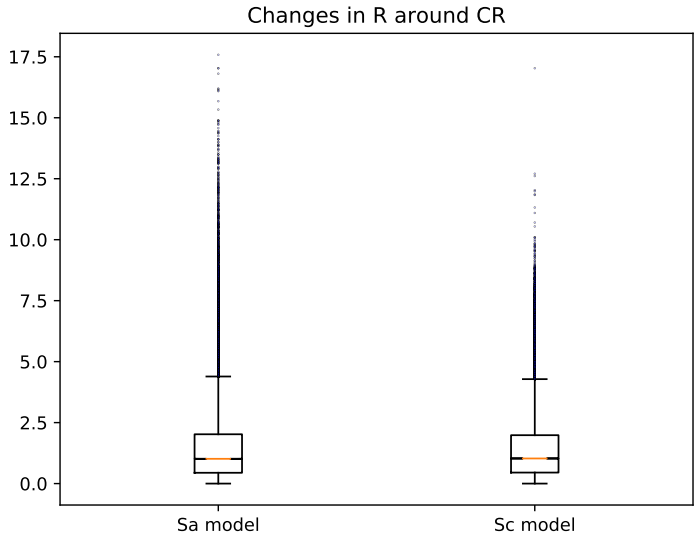

Figure 4.19: Changes in R of the surroundings of the CR of the fiducial models for the Sa and Sc galaxies.

of RM is made in the regions around their own CR in both galaxies. With this, the bin size is different in each model.

Figure 4.18 shows the normalized histogram from t=0 to t = 4 Gyr, where it is clear that the Sc galaxy has a larger RM than the Sa galaxy. Figure 4.19 shows the changes in radius for both galaxies, in their respective CR surroundings. The Sa galaxy has more "extreme migrators" than the Sc galaxy, but there are more driven stars by the Sc galaxy with small radial changes. Table 4.1 summarizes the characteristic values of the particle distributions: median, standard deviation (σ), and the asymmetry of the data distribution (skewness) of each bin presented in Figure 4.18.

Table 4.1: Characteristic values of the particle distribution of each bin in the Sa and Sc galaxy models. The colour bin is the same as in Figure 4.18.

	Coloured bin	Sa	Sc
Median	blue	0.61	0.59
	yellow	0.88	0.86
	green	1.09	1.08
	red	1.37	1.39
σ	blue	0.11	0.13
	yellow	0.15	0.19
	green	0.15	0.2
	red	0.14	0.2
Skewness	blue	0.57	0.84
	yellow	0.27	0.54
	green	-0.17	0.19
	red	0.22	0.01

Chapter 5

Conclusions

It is important to have in mind that radial migration can be studied in different ways. This work focuses on the effect of radial migration on individual stars and isolated galaxies through a systematic study. In the literature, this is first study devoted to analyze the individual contribution to RM due to each spiral arms parameters. It is worth mentioning that steady potentials played a key role to achieve the goals of this Ph.D. thesis.

Here, a series of simulations using a fully analytical galactic model of an early-type and a late-type spiral galaxy, were performed to study the effect of the structural and dynamical parameters of the spiral arms on radial migration. The spiral arms potential was introduced adiabatically during the first Gyr to avoid a spurious response of the stellar distribution. To isolate the individual effect of each parameter of the spiral arms model, simulations where carried out varying, with respect to the fiducial Model A, the spiral radial scale length (Model B), the pitch angle (Model C), and the pattern speed (Model D), for each type of galaxy (Sa and Sc galaxies). In this work were studied the changes in L_z, R, and ecc of the disc particles in each model.

The main findings can be summarised as follows:

- The larger changes in L_z and R occur around corotation resonance, meanwhile the change in eccentricity, Δecc, around this region is smaller compared to its neighborhood. This is indicating that there is radial migration. This result is valid for a Sa and a Sc galaxy.

- The most important parameter in the production of radial migration turns out to be the radial scale length, $R_{\rm sp}$, of the spiral arms, generating the largest changes in L_z and R around corotation resonance and the smallest changes in the eccentricity around that region. For the Sa galaxy, the 53% (third and fourth bins of Figure 4.4) of the Model A_{Sa} and for the Model B_{Sa} 61 and 59% of the particles in the third and fourth bins (12-15 and 15-18 kpc) are tossed to another bin. This is just a little less than 10%. For the case of the Sc galaxy, 50, 55 and 41 % of the particles found at the third, fourth and fifth bins (9-12, 12-15, and 15-18

kpc, respectively) in Model A_{Sc}, are spread beyond their original bin, while these percentages are larger by 10% for Model B_{Sc} (top panel of Figure 4.16).

Furthermore, the radial distribution of particles shows a positive (negative) skewness inside (outside) corotation, a clear signature due to the spiral arms, for the two galactic types.

- In the models, there are particles that move inward or outward up to $\sim$ 15 and $\sim$ 10 kpc for the Sa and Sc galaxies, respectively (Figure 4.19). The CR and OLR contribute to those extreme migrators. This behavior is compatible with the results from the N-body simulations performed by Halle et al. (2018). Although, large changes in R are seen around the OLR in both galaxy models (Sa and Sc), there are no changes in L_z and *ecc*, because of that, those signatures cannot be called RM neither heating, according to the definition adopted in this work. Therefore, a detailed orbital study is needed in order to understand which dynamical processes are generating those large displacements.

- When the R_{sp} is systematically increased (3.5, 5.25, 7 and 8.75 kpc), changes in L_z from 500 up to 2500 are observed. This is a clear evidence that RM strongly depends on this parameter (Figure 4.5).

- For the case when the potential is non conservative (4.1.6), RM is also produced. The particles originally in the third and fourth bins are spread, being the 42 and 48% for the Model A_{Sa} and the 52 and 54% for the Model B_{Sa}, then, RM is about 10% larger for the Model B_{Sa} than for the Model A_{Sa} (see Figure 4.6).

- When the particles are selected for their initial height in z direction ($|z| < 0.5$ kpc or $|z| > 0.5$ kpc), no substantial changes respect to the analysis considering the whole particles are seen. The main difference lies in the density, but not in $\Delta L_z, \Delta R$ or Δecc (see 4.1.7). Then, the particles more affected by RM are those near the galactic plane.

- Comparing the effect of R_{sp} between Sa and Sc galaxies around their respective corotation resonances, it is found that the percentage of displaced particles are very similar, but is slightly larger for Sc galaxy than for the Sa one, due to the fact that Sc is dynamically cooler than the Sa galaxy (see 4.1.4, 4.2.4).

This set of simulations with a cosine model for the spiral arms, clearly shows that the radial scale length of the spiral arms plays a relevant role in defining at which extent the radial migration affects the stellar orbits of the disc. Additionally, it is wanted to stress that to have effective and lasting radial migration, the spiral arms should be transient (see Sellwood & Binney (2002)). Nevertheless, using a steady spiral potential a restricted radial migration can be seen. Even the spiral arms potential used here has a spurious structure like a bar in the central region, the particles within those radial distances are ignored, because the calculations are not physical. Additionally, this structure is not imposing a new set of resonances, also, this study focuses on the

regions around the spiral arms corotation resonance and at these distances, the effects of the spurious structure in the stellar orbits are minimal and can be safely ignored.

Even though a bi-symmetric long-lasting spiral arm was adopted, other types of spiral arms can be implemented such as flocculent or transient spiral arms with more than 2 arms. In the case of the flocculent arms, they can be represented by randomly seeding spherical structures (as a first approximation) along the spiral locus to mimic molecular clouds, following a certain potential spectrum. For the transient arms, a periodic function of time can be used, to grow or decrease the strength of the arm. From N-body simulations with transient spiral arms, it has been measured that the spiral arms lifetime is smaller than 500 Myr. Grand et al. (2014).

A sophisticated study, using a more realistic and variable potentials for the spiral arms, is necessary. That study should take into account the interplay of the structural and dynamical parameters of the spiral arms, including the chemical information that could provide an improved approach to the analysis of radial migration in disc galaxies. It should be kept in mind that not only the inner dynamical effects are able to incentive RM in a galaxy, also external effects can contribute to RM such as interaction of galaxies or satellites.

5.1 Future work

This Ph.D. project can go further in the following main topics:

- As it was shown in the plots of ΔR, there is a set of particles in the OLR that are experiencing large displacements, but this signal is not see in ΔL_z neither Δecc. It should be important to analyse the individual orbits of those particles in order to understand their behaviour.

- An stellar orbital study can be implemented to verify the individual behaviour of the particles in the potential, but it is a good idea to use a more realistic potential based on a mass distribution for the spiral arms. Then the results can be generalized to any kind of disc galaxy. Also, the stellar dynamics, according to the results showed in this work, can be linked to a chemical evolution description though the study of the shapes of the metallicity distribution functions and their role in the chemical evolution from the dynamical point of view.

- An improved spiral arm potential, imposed on an axisymmetric background, will be used to analyze the effect of the radial scale-length of the spiral arms (the most important parameter) on the disc radial migration. An alternate way to study the effect of the spiral arms parameters is to span the possible combinations of the parameters of the background potential in a certain type of galaxy, for instance, the mass and size of the bulge, disc, and/or halo according with the observational data.

- This study takes into account only the effects of the spiral arms on RM, but an important and interesting analysis can be performed including a galactic bar based on a mass model. This bar is not necessarily rotating with same pattern speed of the spiral arms. This decoupling imposes a new set of dynamical resonances, produced by the bar, and will be present along the disc, producing RM, heating or both.
- Additionally, a chemical tagging can be used to compare theoretical models, based on simulations, with observations of the great galactic surveys. This could provide a better understanding which chemical evolutionary models are able to reproduce the stellar chemical distribution of the galaxies.
- Also, using some clues in the shapes of the metallicity distribution functions, some dynamical characteristics of the galaxies can be estimated in a reasonable range, for example, the positions of the main resonances.

Appendix A

Publications

In this Appendix is presented the published paper that this Ph.D. project has as results.

A.1 The influence of the spiral arm parameters on radial migration in late type-like galaxies

Monthly Notices of the ROYAL ASTRONOMICAL SOCIETY

MNRAS **504,** 5919–5926 (2021) doi:10.1093/mnras/stab1241
Advance Access publication 2021 May 4

The influence of the spiral arm parameters on radial migration in late-type-like galaxies

Gerardo Martínez-Bautista,[1]★ Héctor Velázquez,[1]★ Angeles Pérez-Villegas [2]★ and Edmundo Moreno[1]

[1]*Instituto de Astronomía, Universidad Nacional Autónoma de México, A.P. 70-264, 04510 Ciudad de México, México*
[2]*Instituto de Astronomía, Universidad Nacional Autónoma de México, A.P. 106, C.P. 22800 Ensenada, B.C., México*

Accepted 2021 April 27. Received 2021 April 26; in original form 2021 March 22

ABSTRACT

We performed test-particle simulations of a spiral late-type-like galaxy to study the radial migration in a steady potential. Our model includes a bulge, a disc, a dark matter halo, and spiral arms represented by a cosine potential. We varied the structural and dynamical parameters of the spiral arms to study the influence of each configuration on the stellar orbits, such as the pitch angle, the radial scale length, and the pattern speed. We analysed the changes in the z component of the angular momentum (L_z), radius (R), and eccentricity of individual stars at different times. We found that the stellar orbits are affected by radial migration in all cases. Also, we found that the most relevant parameter to the radial migration phenomenon, in co-rotation, is the radial scale length of the spiral arms.

Key words: galaxies: disc – galaxies: kinematics and dynamics – galaxies: spiral – galaxies: structure.

1 INTRODUCTION

Spiral arms are one of the most striking and intriguing features in spiral galaxies. In recent years, there has been an intensive ongoing research in this field to have a better understanding why different spiral patterns are observed, spanning from flocculent, great design, and bisymmetric structures (e.g. Hart et al. 2018, and references therein). In a dynamical context, spiral arms play a relevant role in the stellar orbital dynamics by modifying the angular momentum, leading to some stars moving several kpc beyond the place where they were born, and/or by heating up the stellar disc (Edvardsson et al. 1993; Wielen, Fuchs & Dettbarn 1996). In a seminal work, Sellwood & Binney (2002) proposed a dynamical mechanism for explaining this physical process, the so-called radial mixing, which results from the interaction, in co-rotation (CR), of a perturbing potential, like a spiral arm, on the stellar orbits that move in a smooth galactic axisymmetric potential.

The basic mechanism consists in that a change in the specific orbital angular momentum in the z component, L_z, can be only driven by non-axisymmetric forces, like spiral arms, bars, or molecular clouds. The radial mixing is divided into two branches: 'churning', which means a change in L_z but not in the eccentricity of the stellar orbit, which is commonly referred to as radial migration, and 'blurring' implying changes in both L_z and eccentricity, and it is known as dynamical stellar heating or simply heating (Schönrich & Binney 2009).

However, it should be pointed out that in the literature there is not a general consensus on the definition of radial migration. Some authors consider that radial migration is a change in L_z but without a change in the orbital eccentricity (Vera-Ciro et al. 2014; Loebman et al. 2016; Martinez-Medina et al. 2016); none the less, blurring is considered by some as migration (Minchev & Famaey 2010). In this work, we will adopt the radial migration as a churning mechanism (Sellwood & Binney 2002; Schönrich & Binney 2009).

The study of radial mixing with restricted simulations using a steady galactic model with the spiral arms represented by a cosine potential and/or also by including a quadrupole bar has been extensively used in the literature (Quillen et al. 2009; Monari, Famaey & Siebert 2016a; Monari et al. 2016b; Hunt & Bovy 2018; Hunt et al. 2018a,b, 2019). In particular, Minchev & Famaey (2010) found that the overlapping of resonances is a more efficient mechanism than transient spiral arms alone to mix material due to stellar radial migration along the regions where this overlapping occurs in the disc. Similar results have been found by Martinez-Medina et al. (2016) employing spiral arms and bar models based on a mass distribution for these components (Pichardo et al. 2003; Pichardo, Martos & Moreno 2004). However, more detailed N-body + smoothed particle hydrodynamics (SPH) simulations show that these transient spiral arms could develop different pattern speeds, moving the CR radius in a more wider region of the disc giving rise to radial migration in this more ample region (Grand, Kawata & Cropper 2012). Also, in models with a bar where the slowdown of the bar pattern speed moves CR radius outwards they produce radial migration towards external regions of the disc (Halle et al. 2018).

Both radial migration and heating are not processes that can be measured directly; for this, we must resort to indirect studies through the metallicity distribution function (MDF hereafter). Recent surveys such as APOGEE for the Milky Way (Eisenstein et al. 2011) and CALIFA for external galaxies (Mejía-Narváez et al. 2020) have been measuring the stellar metallicity (Eisenstein et al. 2011) due to the information that can be extracted from the shape, skewness, and the extent of the MDF of a galaxy, giving us an insight about how radial migration has occurred (Hayden et al. 2015; Aumer, Binney & Schönrich 2016; Loebman et al. 2016; Martinez-Medina et al. 2017).

★ E-mail: gmartinez@astro.unam.mx (GM-B); hmv@astro.unam.mx (HV); mperez@astro.unam.mx (AP-V)

Furthermore, local chemo-kinematics studies near the disc plane of the Milky Way show that the thin disc component has stars of all ages at large radii with a positive [Fe/H] skewness in the outskirts, suggesting that radial migration has a relevant role in the metallicity scatter of the thin disc (Grieves et al. 2018).

In an *N*-body simulation of a Milky Way-like galaxy, it is found that stars with very eccentric orbits in the central region can be tossed several kpc outwards near the bar outer Lindblad resonance (OLR) and they are circularized after a few Gyr, so it can be seen as an 'inverse process to heating' (Halle et al. 2018; Khoperskov et al. 2020). Also, particles with a low eccentricity and lagging a short-lived local density peak can migrate outwards of the disc (Comparetta & Quillen 2012). The spiral arms induce an increase of the vertical velocity dispersion of the stars. However, this vertical heating is small and it does not account for the thickening of the disc, and hence the formation of the thick disc; even more, stars with very large vertical velocity dispersion are less prone to radially migrate (Vera-Ciro et al. 2014; Vera-Ciro, D'Onghia & Navarro 2016; Mikkola, McMillan & Hobbs 2020). In addition, it is seen in *N*-body Tree/SPH simulations that, in the presence of a bar, the vertical velocity dispersion of inward migrating populations is smaller than that of the non-migrating populations; therefore, the inward migrating stars have a negative contribution to the vertical heating by 'cooling' the disc at smaller radii than at the CR position of the bar (Minchev et al. 2012b). On the other hand, Roškar et al. (2011) suggested that radial migration would be a natural mechanism to contribute to the formation of the thick disc in the sense that despite the radial velocity dispersion is not increased, the migrating stellar population conserves its vertical energy and, at larger radii, the disc surface falls and in consequence its restoring force decreases. This could cause an increase in the vertical oscillations, favouring the formation of the thick disc.

On the observational side, data have accumulated in recent years indicating that this mechanism of radial migration has been working in our Galaxy and external galaxies. Radial metallicity gradients are of particular interest because they clearly can show the process of radial migration. Some simulations have shown that the initial radial metallicity gradient flattens due to the radial mixing produced by the bar and spiral arms (Minchev et al. 2012a). In particular, if the spiral structure is transient, this defines a CR region where stars may move from one radius to another, reaching up to 5 kpc in less than 0.5 Gyr (Roškar et al. 2011).

In simulations of restricted test particles, of a Milky Way-like model, with transient spiral arms and different pattern speeds, it is found that stars in CR, in addition to experiencing radial migration, also experience radial heating due to the overlap of ultra-harmonic resonances (Daniel et al. 2019). About 40 per cent of the stars in the solar neighbourhood have experienced both radial migration and heating by this overlapping of resonances. Furthermore, in a previous work, Klačka, Nagy & Jurči (2012) indicated that the Sun has migrated at most 1.2 kpc due to the action of spiral arms; however, recent numerical simulations suggest that these non-axisymmetric perturbations have caused a displacement of the Sun of around 3 kpc from its current position due to radial migration (Tsujimoto & Baba 2020).

Using observational data from the AMBRE project (de Laverny et al. 2013) and a semi-analytical model for the Milky Way (Kubryk, Prantzos & Athanassoula 2013), Prantzos et al. (2017) were able to explain the behaviour of the Li/H double branch versus metallicity observed in the local thin and thick disc components as a result of radial migration. Also, by combining the radial information and velocities from the second *Gaia* data release (DR2; Gaia Collaboration 2018) and assuming that it is possible to infer the formation radius of a sample of the branch of the red giants, it is found that some stars have experienced churning or blurring. From this sample, about 10 per cent have experienced radial migration while about 5–7 per cent of them have never been affected by this process (Feltzing, Bowers & Agertz 2020).

Through a galactic surface brightness study using a sample of the CALIFA survey, made by Ruiz-Lara et al. (2017), it is found that radial migration mixes the stellar content, flattening the radial stellar properties such as light, age, and metallicity distributions. However, it strongly depends on the disc characteristics of each galaxy. The authors also suggest that processes like star formation or accretion might be as important as radial migration in the mixing of the stellar properties. In an oxygen abundance study in a sample of spiral galaxies from MUSE, Sánchez-Menguiano et al. (2018) found that some of them have lower (higher) oxygen abundances in the inner (outer) regions than the expected distribution. Even more, they show a large dispersion in the slope distribution of these abundance gradients. Also, Zhuang et al. (2019) investigated the influence of radial migration due to a bar and the spiral arms in the stellar populations, using the radial stellar metallicity information, in a sample of 244 galaxies from CALIFA. They found that radial migration seems to play a secondary role since there is not a strong correlation among its effects and the stellar population gradients.

In order to study the possible influence of radial migration in late-type galaxies, we performed a series of simulations varying the structural and dynamical parameters of the spiral arms. This work is organized as follows. In Section 2, we describe our adopted late-type galaxy and spiral arms models. Section 3 presents the results of our simulations. Finally, a discussion and conclusions are drawn in Section 4.

2 TEST-PARTICLE SIMULATIONS

With the aim to study the influence of the spiral arms parameters on a late-type galaxy, we carry out simulations with test particles. For the sake of clarity, we briefly describe below the models used for this work.

2.1 The model for late-type galaxies

The galactic model for the late-type galaxy is represented by a 3D steady state composed potential. It consists of a Plummer profile with a mass of $M_{\rm B} = 10^{10}$ $\rm M_{\odot}$ and a scale length $r_{\rm B} = 1$ kpc for the bulge (Plummer 1911), a Miyamoto–Nagai distribution for the disc with a mass $M_{\rm D} = 5.1 \times 10^{10}$ $\rm M_{\odot}$ and with the scale lengths $a = 5.31$ kpc and $b = 0.25$ kpc, respectively (Miyamoto & Nagai 1975). For the halo, we adopted a Hernquist profile with a mass of $M_{\rm H} = 4.8 \times 10^{11}$ $\rm M_{\odot}$ and a scale length of $r_{\rm H} = 33$ kpc (Hernquist 1990). The contribution of each component to the rotation curve of the model is shown in the upper panel of Fig. 1.

Following Contopoulos & Grosbol (1986), we represent the spiral arms by the cosine potential:

$$\Phi_{\rm spiral}(R, \phi, z) = f(R)\cos[2\phi + g(R)]{\rm sech}^2\left[\frac{z}{z_0}\right], \quad (1)$$

where (R, ϕ, z) are the cylindrical coordinates in a non-inertial reference frame rotating with the spiral arms, $f(R) = -AR\exp(-R/R_{\rm sp})$ is the amplitude function of the perturbation being A and $R_{\rm sp}$ the amplitude and radial scale length of the spiral arm. The vertical contribution to the potential was taken from Patsis & Grosbol (1996).

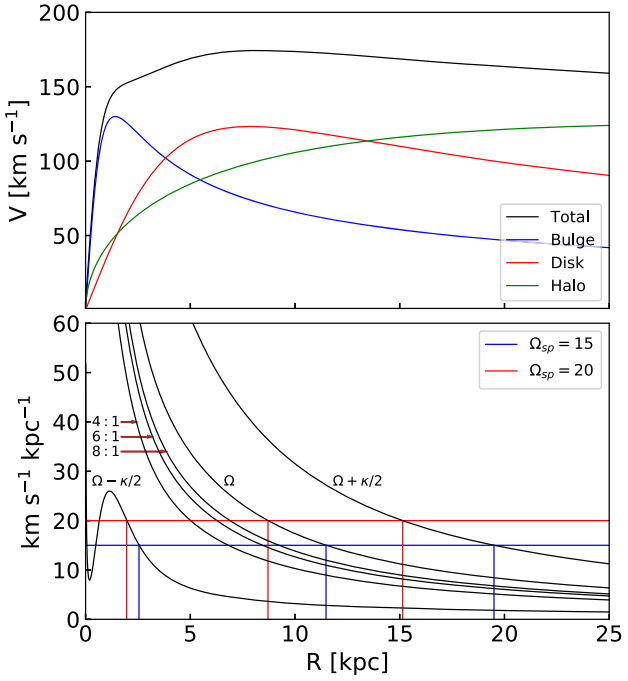

Figure 1. Top panel shows the rotation curve of our late-type galaxy model for the axisymmetric background potential. Bottom panel shows the resonance positions of the model for the two pattern speeds used in this work.

Table 1. Values for the parameters of the spiral arms model adopted in this work to study their role in the radial migration in the disc.

	Spiral arms parameters			
Parameter	A	B	C	D
R_{sp} (kpc)	5.31	6.64	5.31	5.31
i_p (°)	20	20	40	20
Ω_{sp} (km s^{-1} kpc^{-1})	15	15	15	20
A (km^2 s^{-2} kpc^{-1})	650	650	650	650

The geometry of the spiral pattern (*locus*) is given by

$$g(R) = -\frac{2}{N \tan i_p} \ln[1 + (R/R_s)^N], \tag{2}$$

where i_p is the pitch angle, R_s is the start position for the spiral arms, and N is a constant that shapes the starting point of the spiral arms (Roberts, Huntley & van Albada 1979). In this work, N is set to 100 (see Pichardo et al. 2003 for more details).

In this work, we study four models where we vary some of the relevant parameters of the spiral arms potential such as the radial scale length, R_{sp}, the patter speed, Ω_{sp}, and the pitch angle, i_p. In all these cases the amplitude was kept fixed and equal to $A = 650$ km^2 s^{-2} kpc^{-1}. In Fig. 1, we have summarized the different parameter values for the spiral arms models where, we have adopted Model A as our fiducial model. All models share the same axisymmetric background galactic potential. The values for the radial scale length of the spiral arms, R_{sp}, in Fig. 1 are consistent with the results of the work of Mata-Chávez et al. (2019) who found that this scale is larger by 5– 40 per cent than the radial scale length of the disc of a Milky Way-like galaxy. Also, for the pitch angle we included a maximum value of $i_p = 40°$ (Ma et al. 2000; Yu & Ho 2020) since larger values may lead to a model dominated by chaotic orbits, if the chaotic behaviour becomes pervasive, the orbits supporting the spiral arms will be destroyed (Pérez-Villegas et al. 2012; Pérez-Villegas, Pichardo & Moreno 2013, 2015). Meanwhile, the pattern speed values are consistent with the results by Fathi et al. (2009). Bottom panel of Fig. 1 shows the positions of the different resonances for our galaxy model. The blue line corresponds to spiral arms with a pattern speed of $\Omega_{sp} = 15$ km s^{-1} kpc^{-1} while the red line to a pattern speed of $\Omega_{sp} = 20$ km s^{-1} kpc^{-1}, and when $\Omega_{sp} = \Omega - \frac{\kappa}{2}$, $\Omega_{sp} = \Omega + \frac{\kappa}{2}$, and $\Omega_{sp} = \Omega$, the positions of the Inner Lindblad Resonance (ILR), the OLR, and the CR resonance are fixed, respectively. Table 1 gives the spiral arms parameters of our models.

The equations of motion are solved in the non-inertial reference frame system, rotating with a constant angular velocity given by the spiral arms pattern speed Ω_{sp}. The orbits of the test particles in this galaxy potential model are followed by 5 Gyr using a Runge–Kutta integrator (Press et al. 1992) with a Jacobi energy conservation better than 10^{-14}. In all cases, the spiral arms are grown adiabatically during the first Gyr, to avoid a non-negligible transient response of the orbits resulting from an abrupt introduction of this non-axisymmetric perturbation that may lead to a spurious radial migration.

2.2 Initial conditions for test particles

To specifying the positions and velocities of the disc test particles, we resort to the work of Hernquist (1993), a technique resting in Jeans equations and for sake of completeness we describe it briefly below.

Test particle positions are drawn from the Miyamoto–Nagai disc distribution and to determine their velocities we employ the second moment of the Collisionless Boltzmann Equation for an axisymmetric distribution:

$$v_c^2 - < v_\phi >^2 = \sigma_\phi^2 - \sigma_R^2 - \frac{R}{\Sigma} \frac{\partial(\Sigma \sigma_R^2)}{\partial R}, \tag{3}$$

where it has been assumed that the velocity ellipsoid is aligned with the coordinate axes. This expression can be simplified even further by assuming:

$$\sigma_R^2(R) \propto \Sigma(R), \tag{4}$$

and that the azimuthal dispersion is given by the epicyclic approximation as

$$\sigma_\phi^2(R) = \sigma_R^2 \frac{\kappa^2}{4\Omega^2}, \tag{5}$$

where κ and Ω are the epicycle and angular frequency, respectively.

With these assumptions, equation (3) reduces to

$$v_c^2 - < v_\phi >^2 = \sigma_R^2 \left[\frac{\kappa^2}{4\Omega^2} - 1 - 2 \frac{\partial(\ln \Sigma)}{\partial \ln R} \right]. \tag{6}$$

The radial dispersion velocity can be specified to a given radius, $R_\bullet$, using the Toomre Q parameter as a constraint

$$\sigma_R(R_\bullet) = Q_\bullet \frac{3.36 G \Sigma}{\kappa^2}, \tag{7}$$

we take $Q_\bullet = 1.2$ at $R_\bullet = 2a$ to ensure local stability. The vertical dispersion is given by

$$\sigma_z^2 = \pi G \Sigma(R) b. \tag{8}$$

Finally, the Cartesian velocities can be obtained from Gaussian distributions with dispersions σ_z, σ_R, and σ_ϕ and combining

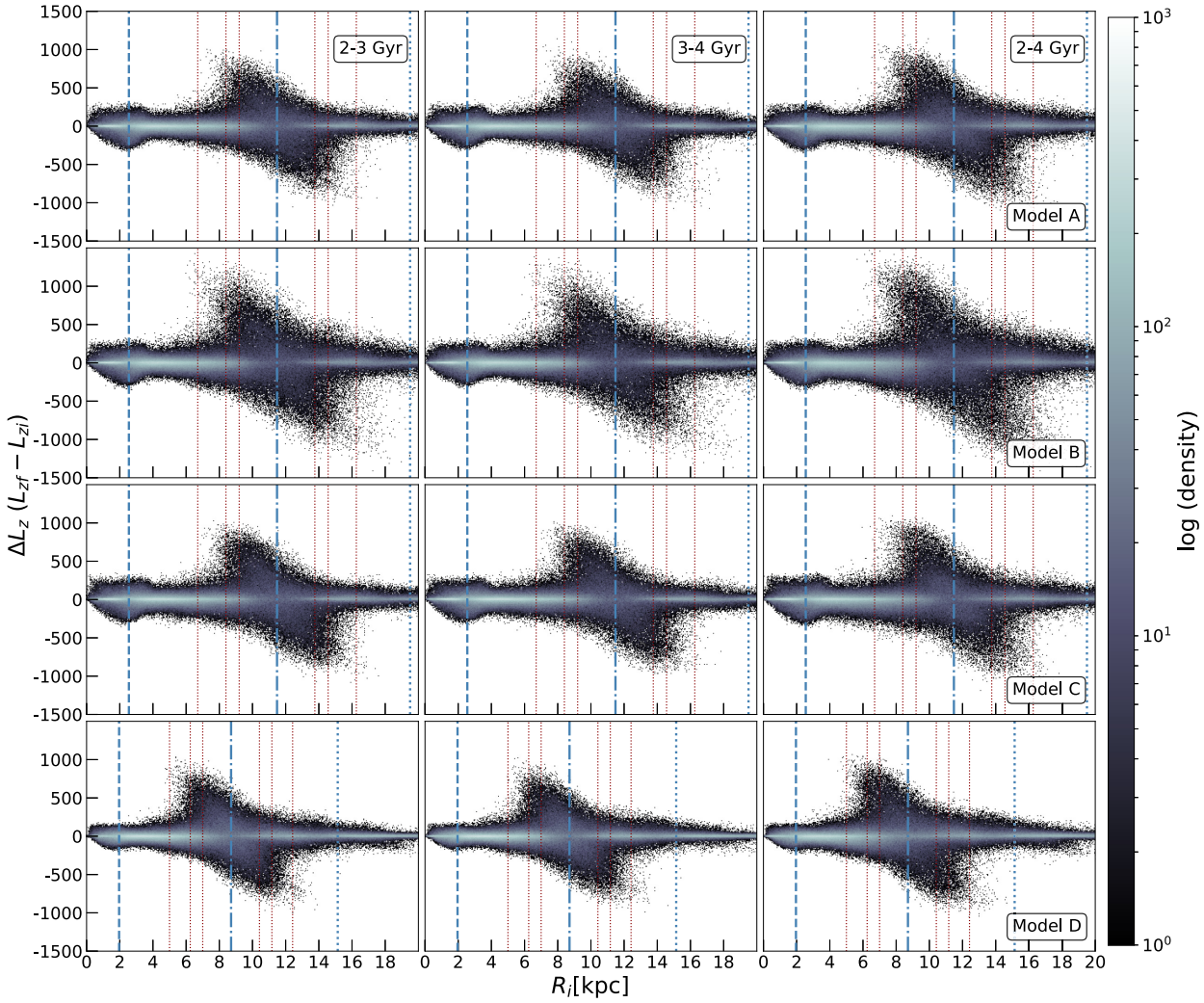

Figure 2. Changes in L_z, given in kpc km s^{-1}, for three different intervals of time (columns). Rows correspond to Models A, B, C, and D, respectively. The blue dashed, dash–dotted, and dotted lines indicate the ILR, CR, and OLR positions of the galaxy, while the red dotted lines indicate the ultra-harmonic resonances (4:1, 6:1, 8:1, 1:8, 1:6, and 1:4, from left to right). The colour bar shows the particle density in a logarithm scale.

these last two with equation (6) to obtain the azimuthal streaming velocity.

3 RADIAL MIGRATION

In order to analyse the radial migration, we estimate the change in angular momentum in the z-component ($\Delta L_z = L_{z,f} - L_{z,i}$), radius ($\Delta R = R_f - R_i$), and eccentricity ($\Delta \mathrm{ecc} = \mathrm{ecc}_f - \mathrm{ecc}_i$) in an interval of time from t_i to t_f. For the eccentricity, we take the following expression (Arifyanto & Fuchs 2006; Minchev et al. 2012a)

$$\mathrm{ecc} = \sqrt{\frac{u^2 + \frac{\kappa^2}{\Omega^2} v^2}{r^2 \kappa^2}}, \tag{9}$$

where u is the radial velocity respect to the galactic centre, $v = V_c - V_\phi$ with V_c and V_ϕ the circular and tangential velocities, respectively, κ is the radial epicyclic frequency, Ω is the angular frequency, and r is de galactocentric distance.

Due to the cosine potential shows a spurious bar-like component in the central part which might cause non-physical variations of the eccentricity in the central region within 3 kpc, we avoid that region for our analysis.

3.1 Changes in L_z

Fig. 2 shows the ΔL_z as function of the initial galactocentric distance, R_i, for our models. From top to bottom, each row corresponds to the evolution of the different models as described in Section 2.1, and from left to right, each column shows ΔL_z between different time intervals 2–3 Gyr, 3–4 Gyr, and 2–4 Gyr.

For our fiducial model A (first line in Fig. 2), the particles showing larger changes in ΔL_z are seen around the CR region, where they are spread in a diagonal centred at this resonance, independently of the chosen time interval, with a maximum of $|\Delta L_z| \sim 1000$ kpc km s^{-1}. When the difference in time is 1 Gyr (two first panels), the ΔL_z seems to have a similar behaviour, but for the difference in time of 2 Gyr (third panel), the accumulative effect could be the responsible of the larger changes seen in ΔL_z and the spread in R_i.

Looking at Model B, for which the radial scale, R_{sp}, of the spiral arms has been increased by around 25 per cent with respect to the fiducial model A (second line in Fig. 2), it shows an increase in ΔL_z, clearly exceeding the maximum value found in Model A, no matter the time. Around CR, not only larger changes in ΔL_z than in model A occur, but also a larger spread in R is seen. In the surrounding of CR, a zone of dispersed particles is formed.

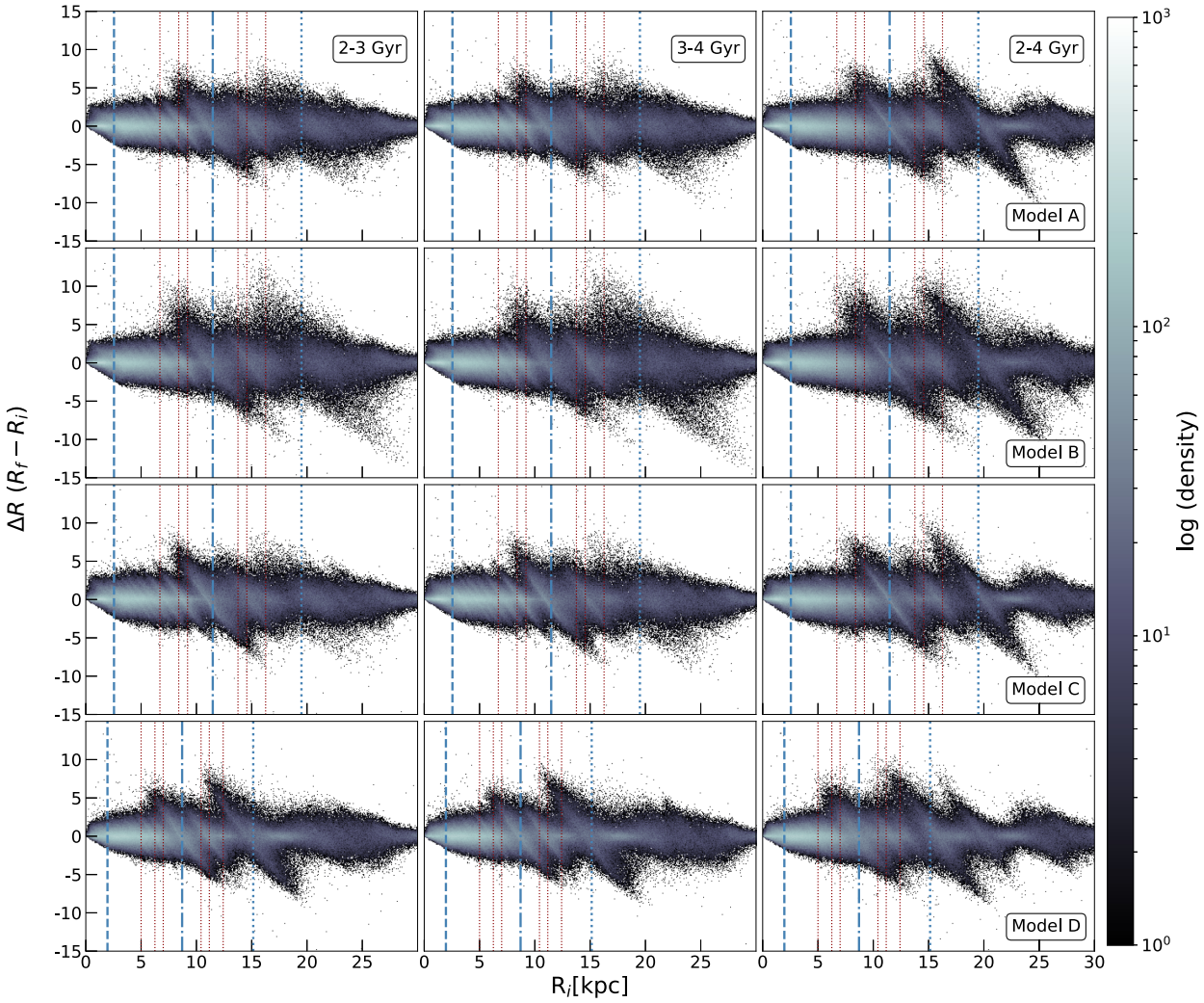

Figure 3. Changes in R, given in kpc, for three different intervals of time (columns). Rows correspond to Models A, B, C and D, respectively. The blue dashed, dash–dotted, and dotted lines indicate the ILR , CR, and OLR positions of the galaxy, while the red ones designate the ultra-harmonic resonances (4:1, 6:1, 8:1, 1:8, 1:6, and 1:4, from left to right).

Regarding Model C, which has a pitch angle larger by a factor of two with respect to the fiducial model A (third line in Fig. 2), ΔL_z seems to have a similar evolution for all the considered time intervals and is only slightly larger than the changes shown in Model A. Finally, for Model D, similar to the fiducial Model A but with a larger patter speed, Ω_{sp}, for the spiral arms (fourth line in Fig. 2), we can see that $|\Delta L_z|$ is similar to the one observed in the CR of Model A. Notice that the location of the CR radius is closer to the centre and they cannot be compared directly, however, the overall behaviour is similar.

3.2 Changes in R

Fig. 3 is similar to Fig. 2, but it shows the change in radii, ΔR, of the stellar orbits. In the first row (our fiducial Model A), ΔR is larger than 5 kpc for time intervals of 1 Gyr around CR and the OLR and less than 5 kpc in other regions. The cumulative effect in two Gyr is clearly seen in the third panel, where ΔR can reach up to 10 kpc in the OLR region. It seems that OLR has stronger effect compared to CR, however, the number of particles spread in OLR is fewer than in CR. Those large displacements were also observed in *N*-body simulations, where particles with very high radial migration were called 'extreme migrators' by Halle et al. (2018). In particular, in those simulations, this behaviour was attributed to the bar OLR, while for our simulations, these are due to the spiral arms. For all times, ridges are connected with the position of the resonances, where the larger displacement is observed.

For Model B (second row), ΔR is bigger than in our fiducial Model A. In these panels, particles near CR and OLR can travel more than 10 kpc (inward or outward), these displacements are significantly larger than those observed in Model A. On the other hand, both Models C and D show a similar global behaviour than Model A, with small differences. For instance, the ridges around the resonances in Model C are more well defined than in Model A while, in Model D, the change ΔR in the OLR is larger than in the region around CR.

Despite all parameters of the spiral arms play a role in the process of radial migration, clearly, the most relevant is the radial scale length R_{sp} of the spiral arms pattern (Model B), leading to larger changes in ΔL_z and ΔR as is shown in the results of Figs 2 and 3, respectively.

3.3 Changes in eccentricity

To disentangle between radial migration and radial heating, we determine the change in eccentricity as defined in equation (9). Fig. 4

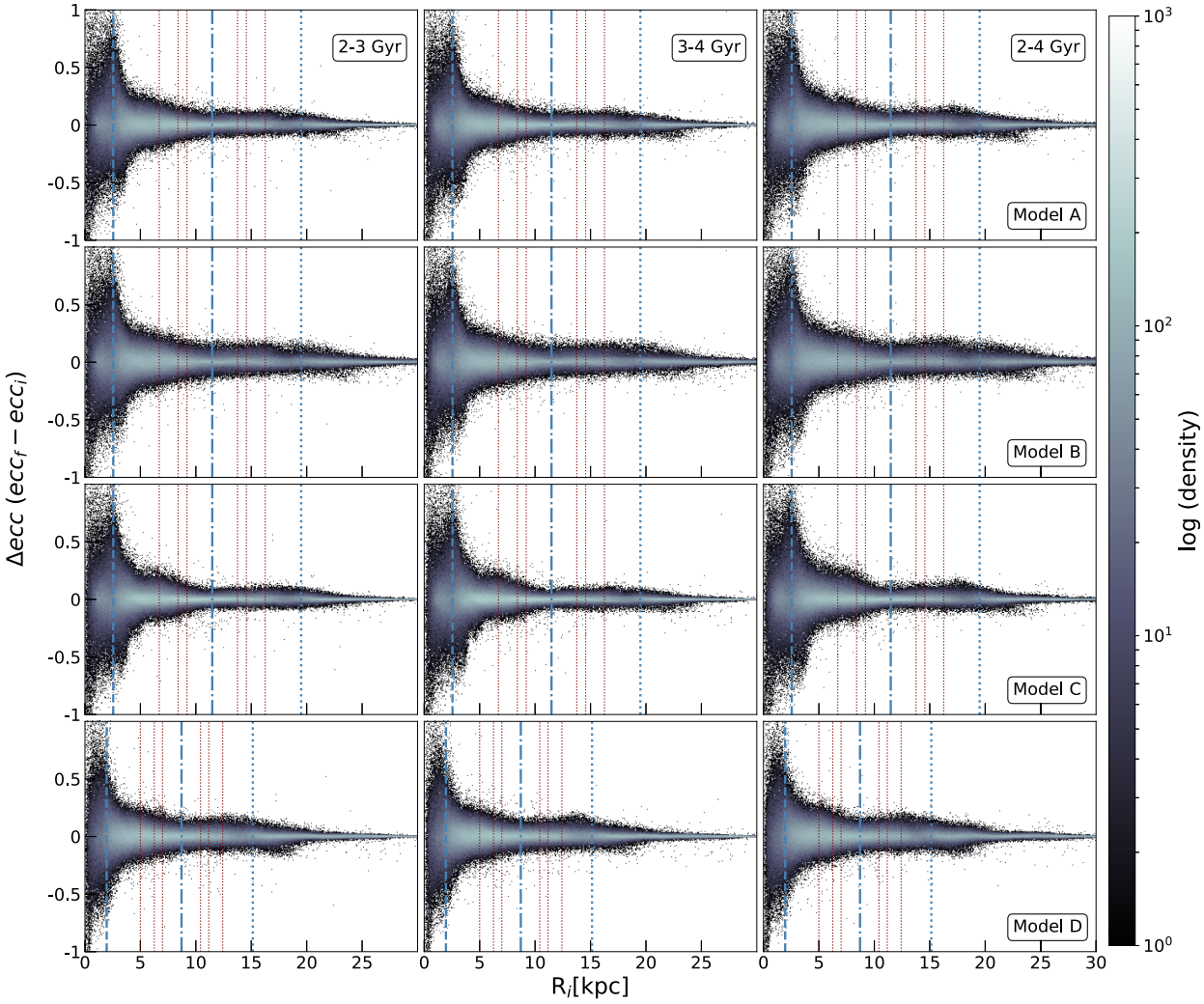

Figure 4. Changes in eccentricity for three different intervals of time given by the columns as in Fig. 2. Rows indicate Models A, B, C, and D. The blue dashed, dash–dotted, and dotted lines are the ILR, CR, and OLR positions of the galaxy, while the red ones designate the ultra-harmonic resonances (4:1, 6:1, 8:1, 1:8, 1:6, and 1:4, from left to right).

shows Δecc as a function of the initial radii R_i at the same three time intervals shown in Figs 2 and 3. It can be seen that in the central region Δecc increases by large values but it is due, in part, to the cosine spiral arms model since it has a non-physical bar-like behaviour and, for our purposes, this region is ignored. However, for all models around CR, we can observe large changes in L_z (Fig. 2) but small changes in ecc (Fig. 4) in CR and other resonances like the OLR, indicating that the stellar orbits can move inwards or outwards preserving nearly circular orbits which is precisely the mechanism of radial migration.

3.4 Quantifying the changes

In order to quantify the effect of modifying the value of the parameters of the spiral arms in the radial migration, we analyse the initial and the final position of each particle in our models. Fig. 5 shows the particle distribution from $t = 0$ to $t = 4$ Gyr. Each coloured 3 kpc-size bin represents the initial position of the particles, and the colour curves are the final particle distribution. Each curve is normalized to the number of particles in its corresponding bin at $t = 0$ Gyr. The solid, dashed, and dotted lines correspond to Model A, Model B, and Model C, respectively. For clarity, Model D is shown separately since the pattern speed of the spiral arms is larger in this case and hence the position of its resonances are closer to the central region (Fig. 5, bottom panel). It can be noticed from this figure that after 4 Gyr the shapes of the curves of the first bins closer to the inner region of the galaxy but not to CR are similar and roughly symmetrical suggesting that radial migration is small. However, the situation is completely different for the bins closer to the CR resonance, all the shapes of the curves show a positive (negative) skewness if the bin is before (after) the CR radius, indicating that radial migration is operating and moving particles to larger (smaller) distances from their original positions. This is particularly more clearly seen in Model B (dashed-line, upper panel of Fig. 5). Also, some positive skewness can be appreciated in Model D for the curve just before the OLR with particles moving up to 10 kpc. These results are in agreement with the results found in previous subsections. This skewness could be used to indirectly determine the position of the principal resonances and, if the rotation curve of the galaxy is known, the pattern speed could be estimated.

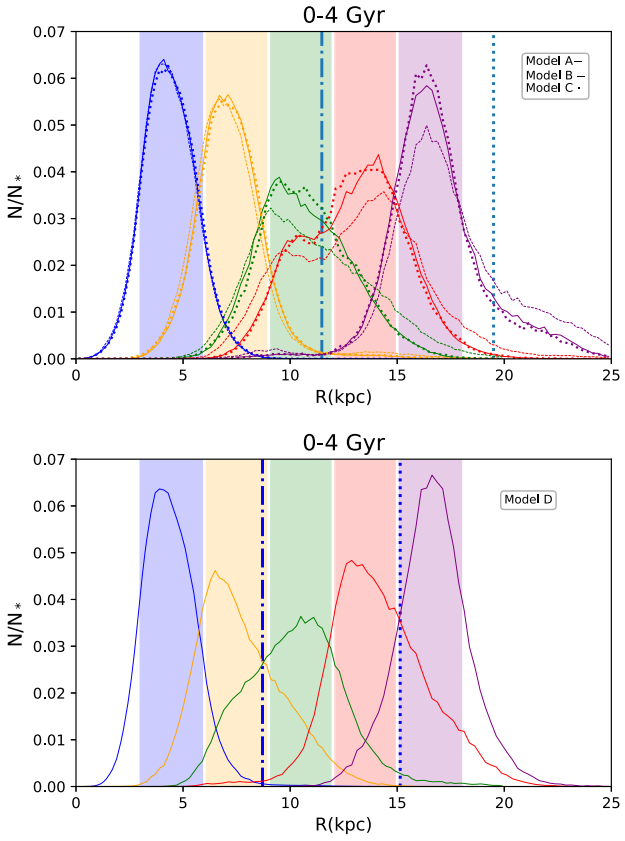

Figure 5. Top row shows the histograms of the number of particles for Models A, B, and C consisting of 5 bins of 3 kpc length starting in 3 kpc. The blue dash–dotted and dotted lines correspond to the CR and the OLR of the galaxy. Each coloured bin represents the initial radii and the curves are the distribution of the same particles after 4 Gyr. The green and red bins are located around the CR resonance, it is clear that the dispersion of particles is larger in this zone than in other places for all models. However, Model B (dashed lines) spreads more particles originally in the green and red coloured bins to other places. Bottom row is the same than top row, but only for Model D, where the resonances are placed in other zones due to the different pattern speed of the spiral arms. Histograms are normalized to the initial (t_0) number of particles.

For Model A, the 50, 55, and 41 per cent of the particles originally found at the third, fourth, and fifth bins (9–12, 12–15, and 15–18 kpc, respectively) at $t = 0$ Gyr, are spread beyond their initial bin. These numbers are slightly different for the Model C, but not enough to make a big difference. Instead, Model B has 59, 62, and 50 per cent of particles that leave their original radial bin, showing a difference in the behaviour of the particles around the main resonances of the system. This model has an increment about 10 per cent of particles that migrate compared to the Model A. For the Model D, the bins around CR are the second, third, and fourth, and the spread particles are 50, 47, and 34 per cent, respectively, as we mention before, this comparison is not straightforward due to the differences in the resonances positions.

4 DISCUSSION AND CONCLUSIONS

The study of radial migration has been addressed and analysed in different scenarios by several authors. For instance, star clusters can migrate to the inner region of our Galaxy, resulting in a fast disruption of these stellar systems due to a strong tidal field (Fujii & Baba 2012). On the contrary, while migrating from the inner parts of the disc up to $\sim$ 5–8 kpc, open clusters are less prone to tidal disruption. Therefore, in the solar neighbourhood, their metallicity is higher than the metallicity of the open clusters that were born there (Anders et al. 2017). Even more, a significant fraction of open clusters in the Milky Way can experience radial migration of about 1.5 kpc Gyr^{-1} (Chen & Zhao 2020).

Also, considering the framework of an infalling galaxy satellite, this will induce the formation of spiral arms and, hence, an increase in the stellar radial migration due to these non-axisymmetric perturbations. This would add considerable dispersion to the age–metallicity relationship in the solar neighbourhood and in the outer parts of the disc, but there is also a considerable radial and vertical heating (Bird, Kazantzidis & Weinberg 2012). In addition, a large number of old metal-poor high-[α/Fe] stars can be found in the solar neighbourhood due to radial mixing, caused by mergers and the subsequent formation of a central bar (Minchev, Chiappini & Martig 2013). Further, a warp and the spiral structure in the external parts caused by a perturbing satellite on to the Galactic disc flatten the metallicity gradients due to stellar migration (Quillen et al. 2009).

It is important to have in mind that radial migration can be studied in different ways; however, this work focuses on the effect of radial migration on individual stars and isolated galaxies, and in a future work we will study the MDF as a clue to radial migration.

We performed a series of simulations using a fully analytical galactic model of a late-type galaxy, to study the effect of the structural and dynamical parameters of the spiral arms on radial migration. We introduce adiabatically the spiral arms potential during the first Gyr to avoid a spurious response of the stellar distribution. To isolate the individual effect of each parameter of the spiral arms model, we carry out simulations where we varied, with respect to our fiducial Model A, the spiral radial scale length (Model B), the pitch angle (Model C), and the pattern speed (Model D). We study the changes in L_z, R, and ecc of the disc particles in each model.

We can summarize our main findings as follows:

(i) The larger changes ΔL_z and ΔR occur around CR; meanwhile, the change in eccentricity, Δecc, around this region is smaller compared to its neighbourhood. This indicates that there is radial migration.

(ii) The most important parameter in the production of radial migration turns out to be the radial scale length, $R_{\rm sp}$, of the spiral arms, generating the largest changes in L_z and R around CR and smaller changes in the eccentricity around that region. The 50, 55, and 41 per cent of the particles found at the third, fourth, and fifth bins (9–12, 12–15, and 15–18 kpc, respectively) in Model A are spread beyond their original bin, while these percentages are larger by 10 per cent for Model B (top panel of Fig. 5).
Furthermore, the radial distribution of particles shows a positive (negative) skewness inside (outside) CR, a clear signature due to the spiral arms.

(iii) In our models, there are particles that move inwards or outwards more than 10 kpc. The CR and OLR contribute to those extreme migrators. This behaviour is compatible with the results from the N-body simulations performed by Halle et al. (2018).

This set of simulations with a cosine model for the spiral arms clearly shows that the radial scale length of the spiral arms plays a relevant role in defining at what extent the radial migration affects the stellar orbits of the disc. Additionally, we want to stress that to have effective and lasting radial migration, the spiral arms should be transient (Sellwood & Binney 2002). Nevertheless, using a steady spiral potential we are able to see a restricted radial migration. We

are aware that a sophisticated study, using more realistic and variable potentials for the spiral arms, is necessary. That study should take into account the interplay of the structural and dynamical parameters of the spiral arms, including the chemical information that could provide an improved approach to the analysis of radial migration in disc galaxies.

ACKNOWLEDGEMENTS

We thank the anonymous referee for the review and suggestions that help us to improve this work. GMB acknowledges CONACYT for the PhD fellowship, and L. Martínez-Medina, E. Athanassoula, O. Valenzuela, and L. Aguilar for the interesting discussions and invaluable suggestions. GMB and HV were supported by the DGAPA-PAPIIT grant IN101918. APV acknowledges the DGAPA-PAPIIT grant IG100319. HV acknowledges the support from the Laboratorio Nacional de Supercómputo del Sureste-Conacyt, the Centro Nacional de Supercómputo-IPICYT-Conacyt, and Miztli of the DGTIC-UNAM. This research was partially supported through computational and human resources provided by the LAMOD UNAM project through the clusters Atocatl and Tochtli. LAMOD is a collaborative effort between the IA, ICN, and IQ institutes at UNAM.

DATA AVAILABILITY

The data used in this article will be shared on request to the corresponding author.

REFERENCES

Anders F. et al., 2017, A&A, 600, A70
Arifyanto M. I., Fuchs B., 2006, A&A, 449, 533
Aumer M., Binney J., Schönrich R., 2016, MNRAS, 459, 3326
Bird J. C., Kazantzidis S., Weinberg D. H., 2012, MNRAS, 420, 913
Chen Y. Q., Zhao G., 2020, MNRAS, 495, 2673
Comparetta J., Quillen A. C., 2012, preprint (arXiv:1207.5753)
Contopoulos G., Grosbol P., 1986, A&A, 155, 11
Daniel K. J., Schaffner D. A., McCluskey F., Fiedler Kawaguchi C., Loebman S., 2019, ApJ, 882, 111
de Laverny P., Recio-Blanco A., Worley C. C., De Pascale M., Hill V., Bijaoui A., 2013, The Messenger, 153, 18
Edvardsson B., Andersen J., Gustafsson B., Lambert D. L., Nissen P. E., Tomkin J., 1993, A&A, 500, 391
Eisenstein D. J. et al., 2011, AJ, 142, 72
Fathi K., Beckman J. E., Piñol-Ferrer N., Hernandez O., Martínez-Valpuesta I., Carignan C., 2009, ApJ, 704, 1657
Feltzing S., Bowers J. B., Agertz O., 2020, MNRAS, 493, 1419
Fujii M. S., Baba J., 2012, MNRAS, 427, L16
Gaia Collaboration, 2018, A&A, 616, A1
Grand R. J. J., Kawata D., Cropper M., 2012, MNRAS, 426, 167
Grieves N. et al., 2018, MNRAS, 481, 3244
Halle A., Di Matteo P., Haywood M., Combes F., 2018, A&A, 616, A86
Hart R. E., Bamford S. P., Keel W. C., Kruk S. J., Masters K. L., Simmons B. D., Smethurst R. J., 2018, MNRAS, 478, 932
Hayden M. R. et al., 2015, ApJ, 808, 132
Hernquist L., 1990, ApJ, 356, 359
Hernquist L., 1993, ApJS, 86, 389
Hunt J. A. S., Bovy J., 2018, MNRAS, 477, 3945
Hunt J. A. S. et al., 2018a, MNRAS, 474, 95
Hunt J. A. S., Hong J., Bovy J., Kawata D., Grand R. J. J., 2018b, MNRAS, 481, 3794
Hunt J. A. S., Bub M. W., Bovy J., Mackereth J. T., Trick W. H., Kawata D., 2019, MNRAS, 490, 1026
Khoperskov S., Di Matteo P., Haywood M., Gómez A., Snaith O. N., 2020, A&A, 638, A144
Klačka J., Nagy R., Jurči M., 2012, MNRAS, 427, 358
Kubryk M., Prantzos N., Athanassoula E., 2013, MNRAS, 436, 1479
Loebman S. R., Debattista V. P., Nidever D. L., Hayden M. R., Holtzman J. A., Clarke A. J., Roškar R., Valluri M., 2016, ApJ, 818, L6
Ma J., Zhao J.-l., Zhang F.-P., Peng Q.-H., 2000, Chin. Astron. Astrophys., 24, 435
Martinez-Medina L. A., Pichardo B., Moreno E., Peimbert A., 2016, MNRAS, 463, 459
Martinez-Medina L. A., Pichardo B., Peimbert A., Carigi L., 2017, MNRAS, 468, 3615
Mata-Chávez M. D., Velázquez H., Pichardo B., Valenzuela O., Roca-Fábrega S., Hernández-Toledo H., Aquino-Ortíz E., 2019, ApJ, 876, 6
Mejía-Narváez A., Sánchez S. F., Lacerda E. A. D., Carigi L., Galbany L., Husemann B., García-Benito R., 2020, MNRAS, 499, 4838
Mikkola D., McMillan P. J., Hobbs D., 2020, MNRAS, 495, 3295
Minchev I., Famaey B., 2010, ApJ, 722, 112
Minchev I., Famaey B., Quillen A. C., Di Matteo P., Combes F., Vlajić M., Erwin P., Bland-Hawthorn J., 2012a, A&A, 548, A126
Minchev I., Famaey B., Quillen A. C., Dehnen W., Martig M., Siebert A., 2012b, A&A, 548, A127
Minchev I., Chiappini C., Martig M., 2013, A&A, 558, A9
Miyamoto M., Nagai R., 1975, PASJ, 27, 533
Monari G., Famaey B., Siebert A., 2016a, MNRAS, 457, 2569
Monari G., Famaey B., Siebert A., Grand R. J. J., Kawata D., Boily C., 2016b, MNRAS, 461, 3835
Patsis P. A., Grosbol P., 1996, A&A, 315, 371
Pérez-Villegas A., Pichardo B., Moreno E., Peimbert A., Velázquez H. M., 2012, ApJ, 745, L14
Pérez-Villegas A., Pichardo B., Moreno E., 2013, ApJ, 772, 91
Pérez-Villegas A., Pichardo B., Moreno E., 2015, ApJ, 809, 170
Pichardo B., Martos M., Moreno E., Espresate J., 2003, ApJ, 582, 230
Pichardo B., Martos M., Moreno E., 2004, ApJ, 609, 144
Plummer H. C., 1911, MNRAS, 71, 460
Prantzos N., de Laverny P., Guiglion G., Recio-Blanco A., Worley C. C., 2017, A&A, 606, A132
Press W. H., Teukolsky S. A., Vetterling W. T., Flannery B. P., 1992, Numerical Recipes in FORTRAN. The Art of Scientific Computing. Cambridge Univ. Press, Cambridge
Quillen A. C., Minchev I., Bland-Hawthorn J., Haywood M., 2009, MNRAS, 397, 1599
Roberts W. W. J., Huntley J. M., van Albada G. D., 1979, ApJ, 233, 67
Roškar R., Debattista V. P., Loebman S. R., Ivezić Z., Quinn T. R., 2011, in Johns-Krull C., Browning M. K., West A. A., eds, ASP Conf. Ser. Vol. 448, 16th Cambridge Workshop on Cool Stars, Stellar Systems, and the Sun. Astron. Soc. Pac., San Francisco, p. 371
Ruiz-Lara T. et al., 2017, A&A, 604, A4
Sánchez-Menguiano L. et al., 2018, A&A, 609, A119
Schönrich R., Binney J., 2009, MNRAS, 396, 203
Sellwood J. A., Binney J. J., 2002, MNRAS, 336, 785
Tsujimoto T., Baba J., 2020, ApJ, 904, 137
Vera-Ciro C., D'Onghia E., Navarro J., Abadi M., 2014, ApJ, 794, 173
Vera-Ciro C., D'Onghia E., Navarro J. F., 2016, ApJ, 833, 42
Wielen R., Fuchs B., Dettbarn C., 1996, A&A, 314, 438
Yu S.-Y., Ho L. C., 2020, ApJ, 900, 150
Zhuang Y., Leaman R., van de Ven G., Zibetti S., Gallazzi A., Zhu L., Falcón-Barroso J., Lyubenova M., 2019, MNRAS, 483, 1862

This paper has been typeset from a TEX/LATEX file prepared by the author.

Bibliography

Abazajian K., et al., 2003, AJ, 126, 2081 2

Anders F., et al., 2017a, A&A, 597, A30 12

Anders F., et al., 2017b, A&A, 600, A70 12

Arifyanto M. I., Fuchs B., 2006, A&A, 449, 533 33

Arp H., 1966, ApJS, 14, 1 2

Athanassoula E., 2016, in Laurikainen E., Peletier R., Gadotti D., eds, Astrophysics and Space Science Library Vol. 418, Galactic Bulges. p. 391 (arXiv:1503.04804), doi:10.1007/978-3-319-19378-6_14 6

Binney J., Tremaine S., 2008, Galactic Dynamics: Second Edition 8, 22, 25

Bird J. C., Kazantzidis S., Weinberg D. H., 2012, MNRAS, 420, 913 11

Chaves-Velasquez L., Patsis P. A., Puerari I., Moreno E., Pichardo B., 2019, ApJ, 871, 79 7

Comparetta J., Quillen A. C., 2012, arXiv e-prints, p. arXiv:1207.5753 11

Contopoulos G., Grosbøl P., 1986, A&A, 155, 11 25

Copernicus N., 1543, De revolutionibus orbium coelestium 1

Daniel K. J., Schaffner D. A., McCluskey F., Fiedler Kawaguchi C., Loebman S., 2019, ApJ, 882, 111 13

Davis B. L., Graham A. W., Seigar M. S., 2017, MNRAS, 471, 2187 27

Davis B. L., Graham A. W., Cameron E., 2019, ApJ, 873, 85 27

Dehnen W., 2000, AJ, 119, 800 9

Eisenstein D. J., et al., 2011, AJ, 142, 72 11

Elmegreen D. M., Elmegreen B. G., 1984, ApJS, 54, 127 6

Fathi K., Beckman J. E., Piñol-Ferrer N., Hernandez O., Martínez-Valpuesta I., Carignan C., 2009, The Astrophysical Journal, 704, 1657 27

Fathi K., Allen M., Boch T., Hatziminaoglou E., Peletier R. F., 2010, MNRAS, 406, 1595 5

Feltzing S., Bowers J. B., Agertz O., 2020, MNRAS, 493, 1419 13

Feuillet D. K., et al., 2018, MNRAS, 477, 2326 11

Freudenreich H. T., 1998, ApJ, 492, 495 7

Fujii M. S., Baba J., 2012, MNRAS, 427, L16 12

Ge J., et al., 2008, in AAS/Division for Planetary Sciences Meeting Abstracts #40. p. 1.06 11

Grand R. J. J., Kawata D., Cropper M., 2012, MNRAS, 426, 167 11

Grand R. J. J., Kawata D., Cropper M., 2014, MNRAS, 439, 623 63

Grieves N., et al., 2018, MNRAS, 481, 3244 11

Guiglion G., de Laverny P., Recio-Blanco A., Worley C. C., De Pascale M., Masseron T., Prantzos N., Mikolaitis Š., 2016, A&A, 595, A18 12

Halle A., Di Matteo P., Haywood M., Combes F., 2018, A&A, 616, A86 11, 34, 43, 56, 62

Hayden M. R., et al., 2015, ApJ, 808, 132 xi, 14, 15

Hernquist L., 1990, ApJ, 356, 359 18

Hernquist L., 1993, ApJS, 86, 389 21

Hubble E. P., 1936, Realm of the Nebulae xi, 1, 2

Kalinova V., et al., 2017, MNRAS, 469, 2539 26

Klačka J., Nagy R., Jurči M., 2012, MNRAS, 427, 358 12

Kubryk M., Prantzos N., Athanassoula E., 2013, MNRAS, 436, 1479 10, 12

Leavitt H. S., Pickering E. C., 1912, Harvard College Observatory Circular, 173, 1 2

Lin C. C., Shu F. H., 1964, ApJ, 140, 646 20

Lin C. C., Yuan C., Shu F. H., 1969, ApJ, 155, 721 14

Lindblad P. O., 1960, Stockholms Observatoriums Annaler, 4, 4 20

Loebman S. R., Debattista V. P., Nidever D. L., Hayden M. R., Holtzman J. A., Clarke A. J., Roškar R., Valluri M., 2016, ApJ, 818, L6 10

Ma J., Zhao J.-l., Zhang F.-p., Peng Q.-h., 2000, Chinese Astron. Astrophys., 24, 435 xi, 27

Martinez-Medina L. A., Pichardo B., Pérez-Villegas A., Moreno E., 2015, ApJ, 802, 109 11

Martinez-Medina L. A., Pichardo B., Moreno E., Peimbert A., 2016, MNRAS, 463, 459 10

Martinez-Medina L. A., Pichardo B., Peimbert A., Carigi L., 2017, MNRAS, 468, 3615 10

Mata-Chávez M. D., Velázquez H., Pichardo B., Valenzuela O., Roca-Fábrega S., Hernández-Toledo H., Aquino-Ortíz E., 2019, ApJ, 876, 6 26

Mejía-Narváez A., Sánchez S. F., Lacerda E. A. D., Carigi L., Galbany L., Husemann B., García-Benito R., 2020, MNRAS, 499, 4838 xi, 14, 16

Minchev I., Famaey B., 2010, ApJ, 722, 112 8, 9

Minchev I., Famaey B., Quillen A. C., Di Matteo P., Combes F., Vlajić M., Erwin P., Bland-Hawthorn J., 2012a, A&A, 548, A126 12, 33

Minchev I., Famaey B., Quillen A. C., Dehnen W., Martig M., Siebert A., 2012b, A&A, 548, A127 12

Minchev I., Chiappini C., Martig M., 2013, A&A, 558, A9 12

Miyamoto M., Nagai R., 1975, PASJ, 27, 533 18

Navarro J. F., Frenk C. S., White S. D. M., 1996, ApJ, 462, 563 7

Ohnishi T., 1975, Progress of Theoretical Physics, 53, 1042 14

Patsis P. A., Athanassoula E., 2019, MNRAS, 490, 2740 7

Patsis P. A., Grosbøl P., 1996, A&A, 315, 371 20

Patsis P. A., Tsigaridi L., 2017, Ap&SS, 362, 129 7

Pérez-Villegas Á., 2013, PhD thesis, Instituto de Astronomía, UNAM 33

Pérez-Villegas A., Pichardo B., Moreno E., Peimbert A., Velázquez H. M., 2012, ApJ, 745, L14 26, 27

Pérez-Villegas A., Pichardo B., Moreno E., 2013, ApJ, 772, 91 26, 27

Pérez-Villegas A., Pichardo B., Moreno E., 2015, ApJ, 809, 170 27

Pichardo B., Martos M., Moreno E., Espresate J., 2003, ApJ, 582, 230 7, 10, 20

Pichardo B., Martos M., Moreno E., 2004, ApJ, 609, 144 7, 10

Plummer H. C., 1911, MNRAS, 71, 460 18

Prantzos N., de Laverny P., Guiglion G., Recio-Blanco A., Worley C. C., 2017, A&A, 606, A132 12

Press W. H., Teukolsky S. A., Vetterling W. T., Flannery B. P., 1992, Numerical recipes in FORTRAN. The art of scientific computing 21, 25

Quillen A. C., Minchev I., Bland-Hawthorn J., Haywood M., 2009, MNRAS, 397, 1599 11

Roberts W. W. J., Huntley J. M., van Albada G. D., 1979, ApJ, 233, 67 20

Roškar R., Debattista V. P., Loebman S. R., Ivezić Z., Quinn T. R., 2011, in Johns-Krull C., Browning M. K., West A. A., eds, Astronomical Society of the Pacific Conference Series Vol. 448, 16th Cambridge Workshop on Cool Stars, Stellar Systems, and the Sun. p. 371 (arXiv:1101.1202) 12

Roškar R., Debattista V. P., Quinn T. R., Wadsley J., 2012, MNRAS, 426, 2089 12

Ruiz-Lara T., et al., 2017, A&A, 604, A4 13

Sánchez-Menguiano L., et al., 2018, A&A, 609, A119 13

Sánchez S. F., et al., 2015, A&A, 573, A105 13

Schönrich R., Binney J., 2009, MNRAS, 396, 203 8

Sellwood J. A., Binney J. J., 2002, MNRAS, 336, 785 7, 43, 62

Sellwood J. A., Masters K. L., 2021, arXiv e-prints, p. arXiv:2110.05615 6

Sofue Y., 2016, PASJ, 68, 2 26

Toomre A., 1964, ApJ, 139, 1217 6

Veltz L., et al., 2008, A&A, 480, 753 4

Vera-Ciro C., D'Onghia E., Navarro J., Abadi M., 2014, ApJ, 794, 173 9, 11, 12

Vorontsov-Velyaminov B. A., 1959, Atlas and Catalog of Interacting Galaxies (1959, p. 0 2

Weiland J. L., et al., 1994, ApJ, 425, L81 7

Yoachim P., Dalcanton J. J., 2006, AJ, 131, 226 4

Yu S.-Y., Ho L. C., 2020, ApJ, 900, 150 27

Zhuang Y., Leaman R., van de Ven G., Zibetti S., Gallazzi A., Zhu L., Falcón-Barroso J., Lyubenova M., 2019, MNRAS, 483, 1862 13

van der Kruit P. C., 1988a, A&A, 192, 117 5

van der Kruit P. C., 1988b, A&A, 192, 117 5